ISTANBUL TECHNICAL UNIVERSITY ★ GRADUATE SCHOOL OF SCIENCE ENGINEERING AND TECHNOLOGY

DESIGN, FABRICATION AND CHARACTERIZATION OF SUBWAVELENGTH-SCALE DISTANCE SENSORS BASED ON OPTICAL DIRECTIONAL COUPLING

M.Sc. THESIS

Shahab BAKHTIARI GORAJOOBI

Department of Mechatronics Engineering

Mechatronics EngineeringProgram

Anabilim Dalı : Herhangi Mühendislik, Bilim
Programı : Herhangi Program

October 2013

ISTANBUL TECHNICAL UNIVERSITY ★ GRADUATE SCHOOL OF SCIENCE ENGINEERING AND TECHNOLOGY

DESIGN, FABRICATION AND CHARACTERIZATION OF SUBWAVELENGTH-SCALE DISTANCE SENSORS BASED ON OPTICAL DIRECTIONAL COUPLING

M.Sc. THESIS

Shahab BAKHTIARI GORAJOOBI
(518111057)

Department of Mechatronics Engineering

Mechatronics Engineering Program

Thesis Advisor: Asst. Prof. Dr. Erdal BULĞAN

Anabilim Dalı : Herhangi Mühendislik, Bilim
Programı : Herhangi Program

October 2013

İSTANBUL TEKNİK ÜNİVERSİTESİ ★ FEN BİLİMLERİ ENSTİTÜSÜ

OPTİK YÖNLÜ BAĞLAŞIM TEMELLİ DALGABOYU-ALTI MESAFE ÖLÇÜM SENSÖRLERİNİN TASARIMI, İMALATI VE KARAKTERİZASYONU

YÜKSEK LİSANS TEZİ

Shahab BAKHTIARI GORAJOOBI
(518111057)

Mekatronik Mühendisliği Anabilim Dalı

Mekatronik Mühendisliği Programı

Tez Danışmanı: Yrd. Doç. Dr. Erdal BULĞAN
Anabilim Dalı : Herhangi Mühendislik, Bilim
Programı : Herhangi Program

EKİM 2013

Shahab Bakhtiari Gorajoobi, a **M.Sc.** student of ITU **Graduate School of Science Engineering and Technology** student ID **51811057**, successfully defended the **thesis** entitled "**DESIGN, FABRICATION AND CHARACTERIZATION OF SUBWAVELENGTH-SCALE DISTANCE SENSORS BASED ON OPTICAL DIRECTIONAL COUPLING**", which he prepared after fulfilling the requirements specified in the associated legislations, before the jury whose signatures are below.

Thesis Advisor :	**Asst. Prof. Dr. Erdal BULĞAN** İstanbul Technical University	....
Jury Members :	**Prof. Dr. Ata MUĞAN** İstanbul Technical University	....
	Asst. Prof. Dr. Mustafa Fazıl Serincan Istanbul Bilgi University	....

Date of Submission : 03 May 2013
Date of Defense : 21 October 2013

To the loving memory of my Mother,

and to my Father who has supported me in all of my endeavors.

FOREWORD

I wish to thank, first and foremost, my advisor, Dr. Erdal Bulgan for his support, motivation and guidance. This thesis would have not been possible without his encouragement and support.

To all of my friends and colleagues, Mohammadreza, Hatef, Morteza, Amir, Ali, Azadeh, Unal, Jaber and Ekrem. Thank you guys for your ongoing support and friendship.

I owe a special thanks and appreciation to my dear friend, Mustafa, who has been always helpful and consistently supportive. I also acknowledge TUBITAK for funding the project.

Finally, I would like to thank my Mom and Dad for all the unending love they have given me, my brothers, Afshin and Afshar whose care and encouragement have kept me going on.

October 2013 Shahab Bakhtiari Gorajoobi

TABLE OF CONTENTS

Page

ABBREVIATIONS

ODC	: Optical Directional coupler
AFM	: Atomic Force Microscopy
BOX	: Buried Oxide
EBL	: Electron Beam Lithography
FDTD	: Finite-Difference Time-Domain
BPM	: Beam Propagation Method
CMT	: Coupled Mode Theory
ICP-DRIE	: Inductively-Coupled-Plasma Deep-Reactive-Ion-Etching
MEMS	: Microelectromechanical Systems
NEMS	: Nanoelectromechanical Systems
NIR	: Near Infrared
PMMA	: Poly(methyl methacrylate)
RF	: Radio Frequency
SEM	: Scanning Electron Microscope
SOI	: Silicon-on-Insulator
TE	: Transverse-Electric
TM	: Transverse-Magnetic
WDM	: Wavelenght Division Multiplexing
FSR	: Free Spectral Range
MZI	: Mach-Zehnder Interferometer
DC	: Directional Coupler
CMOS	: Complementary Metal–Oxide–Semiconductor
MCDC	: Multichannel Directional Coupler
FFT	: Fast Fourier Transform
TLS	: Tunable Laser Source
PC	: Polarization Controller
DUT	: Device Under Test
PD	: Photo Detector

LIST OF TABLES

Page

LIST OF FIGURES

Page

DESIGN, FABRICATION AND CHARACTERIZATION OF SUBWAVELENGTH-SCALE DISTANCE SENSORS BASED ON OPTICAL DIRECTIONAL COUPLING

SUMMARY

This thesis presents theoretical and experimental study of ultra-compact Si-wire Optical Directional Couplers (ODCs) on Silicon-on-Insulator (SOI) wafer for telecommunication and sensory applications especially in nanoscale sensing. The presence of the controllable evanescent light strongly confined in the region bounded by the Si nano-wires is found to have a large impact on the optical power coupling between waveguides. The characteristics of coupling length and power transmission in ODCs based on separation, wavelength, light field propagation distance and geometry of waveguides are described by the Coupled Mode Theory (CMT), 3D Finite-Difference Time-Domain (FDTD) Analysis and Beam Propagation Method (BPM), and are confirmed by experiments.

Using BPM method the symmetric and antisymmetric electric mode profiles of a 300nm-wide and 340nm-thick SOI ODC and the corresponding electrical powers are found. The coupling length of the aforementioned ODC geometry as a function of separation distance between the two waveguides is also calculated. The exponential dependency of coupling length on the separation of coupled waveguides and wavelength shows interesting high-sensitivity optical sensing and switching properties. The effects of the geometry of the waveguides on the coupling length and possible fabrication imperfections can cause several micrometers change in coupling length. Also the coupling length is found to be changeable as the wavelength of the light field changes. The wavelength dependency of a 5µm-long ODC on separation distance using 3D FDTD simulations is shown, and the wavelength responses of 100nm, 200nm and 300nm-separated ODCs with changeable coupled-waveguide lengths are also calculated. Custom spectral properties can be achieved by the configuration of coupled nano-wire waveguides based on their separation and lengths. All of the components designed for ODC fabrication, such as directional couplers, bending waveguides and optical power splitters are simulated using an FDTD simulations order to reduce the failure possibilities in fabrication process and experimental characterization.

ODCs are fabricated utilizing SOI wafer platform. First, a 50nm-thick layer of electron beam lithography resist (PMMA) is coated on the SOI wafer, and then desired pattern is transferred to the resist by electron beam lithography. The entire structure is then coated by chromium in electron beam evaporation process and the remaining PMMA resist is lifted-off the desired silicon surface. Then, using the ICP-DRIE etching process undesired regions of the silicon layer, which are not coated by chromium are etched, and the whole wafer is diced into two parts after removal of the chromium layer on the device.

Ultimately, guidelines on optimization of ultra compact high-sensitivity optomechanical sensors, switches and WDM devices are provided. several SEM

micrographs of the fabricated devices after each fabrication stage are studied in order to find the best recipe and understand how the fabrication parameters affect the structures. All of the geometries including width, length and separation distance of waveguide pairs in each ODC device are measured under SEM.

Fabricated devices are characterized using a tunable laser source. Output powers from both of the parallel and cross port of the ODCs are detected using an InGaAs NIR camera and then transferred to computer. Results show that the output light power changes sinusoidally with the length of the coupler. The gradient field between two waveguides is highly dependent on their separation such that smaller separation distances yield smaller coupling lengths causing sharper variations at the output power. Hence, ODCs with variable separation can be exploited for high-sensitivity optomechanical switches or sensor devices while changes in length can be utilized in applications requiring higher range of motion or low-sensitivity. ODCs as filters and wavelength-selective devices are also simulated, fabricated and characterized. The separation and length of the ODCs can be optimized for the desired filter spectrum. The transmission spectra of ODCs are found to be tunable by their separation and length such that, for instance, increasing the separation distance from 150nm to 200nm for a 10μm-long ODC at 1578nm wavelength will drop the transmission from almost 100% down to about 0% at through port. Longer ODCs have more channel dropping characteristics making them suitable for the design of tunable wide-FSR channel-dropping filters. In all experiments results show a good agreement between theory and experiment.

The next step is the realization of ODCs to see their performance as a displacement sensor. Structures are proposed to observe and analyze the effects of separation and length parameters of the ODCs in displacement sensing applications. For this purpose, in order to generate subwavelength motions in the system, micro-comb actuators are simulated and characterized based on the desired displacement values. The output displacement of the designed com-actuator is given as a function of input voltage. Since the connection between the movable waveguide in an ODC to the mechanical actuator may cause additional cross-talk in the system the waveguide is splitted into sections constructing two ODCs with almost the same functionality but capable to be handled from the center using low-loss elliptical waveguides.

Using the optical power change along the ODC can be utilized for higher ranges of motions, but according to the limits of fabrication, ODCs with less than 200nm constant separation are hard and expensive to fabricate, on the other hand, for longer separation distances, in order to test the device the actuator should at least generate motions more than 3μm which needs a very large number of actuation fingers. Since the fabrication area for a subfield is limited (induced by the e-beam lithography system), the enlargement of the numbers of the fingers is not possible. Alternatively, a new device based on Mach-Zehnder Interferometry in which one of the arms includes an ODC is simulated. According to the CMT an ODC can change the phase of the output light with respect to the separation and length. Hence, having the phase difference at the output of the MZI can be used for sensing. FDTD simulations show that the device can be used as both high and low-sensitivity sensors at short or long distances.

Devices are patterned on a layer of PMMA coated on a SOI wafer. The correct dose is found by several controlled trials of writings. Then, in order to have a complete device including input coupler waveguide, output waveguide, comb actuator and electrical connections several subfields are patterned individually on the PMMA and aligned carefully together. Then, a layer of 30nm-thick Cr is coated on top of the

PMMA and the rest of the PMMA is lifted off the wafer. Si device is then etched down to the SiO_2 layer using Inductively Coupled Plasma (ICP), and the Cr layer is removed from the top of the devices. In order to release the mechanical parts floating in the air, devices are exposed to the vapor HF. Various devices connected to micro-comb actuators as the source of motion are fabricated.

MZ based devices with length of 10µm, 12.5µm and 17.5 µm, and ODCs with 10µm and 15µm are tested. For MZ devices a distinction ratio of 4dB at 1550nm wavelength at less than 60nm displacement is achieved. For a 15µm-long ODC more than 15dB attenuation in the output signal can be achieved for less than 25nm displacement around 70nm separation. The spectral response of the devices is measured to be very sensitive to the changes of separation. For instance, dips in the spectra of an MZ device with 12.5µm coupler length can be red-shifted for 17nm by changing the separation from 60nm to 110nm. ODCs also show interesting spectral characteristics. If the length of the ODC is kept long while working at the small separations, small changes (few nanometers) in the separation can cause large attenuation or boost in the output signal. It is also shown that for a 15µm-long ODC at 125nm separation more than 25dB attenuation can be achieved by decreasing the separation to 90nm at 1540nm wavelength.

OPTİK YÖNLÜ BAĞLAŞIM TEMELLİ DALGABOYU-ALTI MESAFE ÖLÇÜM SENSÖRLERİNİN TASARIMI, İMALATI VE KARAKTERİZASYONU

ÖZET

Bu tezde özellikle nano-boyutlu sensör ve telekomünikasyon uygulamaları için, yalıtkan üzeri silisyum (Silicon-on-insulator, SOI) pul üzerinde ultra-kompakt silisyum-tel Optik Yönlü Bağlaştırıcılar'ın (Optical Directional Couplers, ODCs) teorik ve deneysel çalışmaları sunulmaktadır. Silisyum nano-teller tarafından sınırlandırılan bölgede, güçlü bir şekilde sınırlandırılmış kontrol edilebilen kaybolan ışığın varlığının, dalgakılavuzları arasındaki optik güç bağlaşımı üzerinde büyük bir etkiye sahip olduğu bulunmuştur. Mesafe, dalgaboyu, dalgakılavuzu geometrisi ve ışık alan ilerleme mesafesine bağlı olarak Optik yönlü Bağlaştırıcılar'da (ODCs) güç iletimi ve bağlaşma uzunluğunun karakterizasyonu, Bağlaşmış Mod Teorisi (Coupled Mode Theory, CMT), Sonlu-Fark Zaman-Alanı (Finite-Difference Time-Domain, FDTD) Analizi ve Işın İlerleme Yöntemi (Beam Propogation Method, BPM) ile açıklanmış ve deneysel olarak doğrulanmıştır.

BPM metodu kullanılarak, 300nm genişlik ve 340nm kalınlığa sahip SOI ODC'lerin simetrik ve antisimetrik elektriksel mod profilleri ve bu profillere karşılık gelen elektriksel güçler bulunmuştur. Ayrıca, iki dalgakılavuzu arasındaki ayrım mesafesinin bir fonksiyonu olarak sözkonusu ODC geometrilerinin bağlaşma uzunluğu hesaplanmıştır. Bağlaşmış dalgakılavuzları arasındaki mesafenin ve dalgaboyunun bağlaşım uzunluğuna olan üstel etkisi dikkate değer yüksek-hassasiyetli optik algılama ve anahtarlama özellikleri göstermektedir. Dalgakılavuzu geometrisinin ve olası imalat hatalarının bağlaşma uzunluğu üzerindeki etkisi, birkaç mikrometrelik değişimlere sebep olabilmektedir. Ayrıca, ışık alanının dalgaboyu değiştirilirken bağlaşma uzunluğunun da değişeceği anlaşılmıştır. Mesafenin 5μm-uzunluklu bir optik yönlü bağlaştırıcının dalgaboyuna bağlılığı, üç boyutlu FDTD simulasyonu kullanılarak gösterilmiştir, ve ayrıca farklı bağlaşma uzunluklarına sahip dalgakılavuzları ile 100nm, 200nm ve 300nm mesafeli ODC'lerin dalgaboyu cevapları hesaplanmıştır. İhtiyaca özel spektral özellikler, bağlaşmış nano-tel dalgakılavuzlarının mesafe ve uzunluklarına bağlı olarak konfigürasyonu ile elde edilebilir olduğu anlaşılmıştır. Yönlü bağlaştırıcılar, dönüş dalgakılavuzları ve optik güç bölücüler gibi Optik Yönlü Bağlaştırıcılar'ın imalatı için tasarlanmış bileşenlerin tümü, deneysel karakterizasyon ve imalat sürecindeki hata olasılığını azaltmak için FDTD simülasyonları kullanılarak nümerik olarak çalışılmışlardır.

Optik Yönlü Bağlaştırıcılar SOI pul platformu kullanılarak üretilmişlerdir. İlk olarak, SOI pulların üzeri 50nm kalınlığa sahip Elektron Hüzme Litografi rezist tabakası (Electron Beam Lithography Resist, PMMA) ile kaplanmış, ve daha sonra istenilen desen Elektron Hüzme Litografi (Electron Beam Lithography) ile rezist tabakasına aktarılmıştır. Daha sonra, yapının tümü Elektron Hüzme Buharlaştırma (Electron Beam Evaporation) işlemi yardımıyla krom ile kaplanmış, ve kalan PMMA rezist katmanı istenilen silisyum yüzeyinden kaldırılmıştır. Ardından kromla kaplanmış silisyum katmanın istenmeyen bölgesi Endüktif-Eşleşmiş-Plazma Derin-Reaktif-İyon-Kazıma (Inductively-Coupled-Plasma Deep-Reactive-Ion-Etching, ICP-DRIE) prosesi kullanılarak kazınmış ve tüm pul cihaz üzerinden krom katmanın kaldırılmasından sonra iki parçaya bölünerek mekanik ve optik karakterizasyona hazır hale getirilmiştir.

Son olarak, ultra-kompakt yüksek-hassasiyetli optomekanik sensörler, anahtarlar ve Dalgaboyu Bölmeli Çoklayıcı (Wavelength Division Multiplexer, WDM) cihazların optimizasyonu ile ilgili erişilen prensipler belirlenerek sunulmuştur. Fabrikasyon parametrelerinin yapıyı nasıl etkilediğini anlamak ve en iyi reçeteleri bulmak için herbir üretim aşamasından sonra üretilen cihazların bir kısmı Taramalı Elektron Mikroskobu (SEM)' nda çalışılmıştır. Herbir ODC cihazında dalgakılavuzu çiftlerinin genişlik, uzunluk ve ayrım mesafesini kapsayan tüm geometrik özellikleri SEM altında ölçülmüştür.

Üretilen cihazlar ayarlanabilir lazer kaynağı kullanarak karakterize edilmiştir. ODC'nin hem paralel hem de çarpraz portlarındaki çıkış gücü bir InGaAs NIR kamera kullanılarak tespit edilmiş ve daha sonra bu görüntüler bilgisayara aktarılarak analizleri gerçekleştirilmiştir. Sonuçlar göstermiştir ki ışık çıkış gücü, bağlaştırıcı uzunluğu ile sinüsoidal olarak değişmektedir. İki dalgakılavuzu arasındaki gradyen alanı yüksek oranda mesafeye bağlıdır, öyle ki daha küçük ayrım mesafeleri çıkış gücünde keskin farklılıklara neden olan daha küçük bağlaşma uzunluklarına yolaçmaktadır. Bu yüzden, daha yüksek hareket aralığı ya da düşük-hassasiyet gerektiren uygulamalarda uzunluktaki değişimlerden faydalanılabiliyorken, optomekanik anahtarlar ya da dedektör cihazlar için ise farklı mesafeye sahip ODC'lerde yüksek-duyarlıklı kullanılabilecektir. ODC'lerin filtre ve dalgaboyu seçici cihazlar olarak kullanımına yönelik şekilde simülasyonları da yapılmış, üretilmiş ve karakterize edilmişlerdir. ODC'lerin ayrım mesafesi ve boyu istenilen filtre tayfı için en uygun hale getirilebilir. ODC'lerin iletim spektrumunun ayrım mesafeleri ve bağlaşma boyları yardımıyla ayarlanabilir olduğu bulunmuştur, öyle ki örneğin; 1578nm dalgaboyundaki 10µm-uzunluğa sahip bir ODC için ayrım mesafesinin 150nm'den 200nm'ye çıkarılması bağlantı noktası üzerinden iletimi neredeyse %100'den %0'a düşürebilmektedir. Daha uzun ODC'ler sayesinde erişilen ayarlanabilir geniş Serbest Spektrum Aralığı (Free spectral Range, FSR), daha yüksek kanal-düşürme özelliklerine sahip filtrelerin tasarımı için uygun kılmaktadırlar. Bu tezde gerçekleştirilen tüm çalışmalarda, teorik ve deneysel sonuçlar arasında iyi bir uyum elde edilmiştir.

Bir sonraki adım, ODC'nin bir mesafe sensörü olarak performansını görmek için gerçeklenmesi olmuştur. Mesafe sensörü uygulamalarında ODC'nin mesafe ve boyut parametrelerinin etkilerini gözlemlemek ve analiz etmek için bir dizi cihaz yapısı önerilmiştir. Bu amaçla, sistemde dalgaboyu-altı hareketleri üretmek için ihtiyaç duyulan yerdeğiştirme değerleri esas alınarak mikro-tarak (micro-comb) eyleyicilerin hesaplamaları ve karakterizasyonları gerçeklenmiştir. Tasarlanan tarak-eyleyicinin yerdeğiştirme çıktısı giriş voltajının bir fonksiyonudur. Bir ODC'de hareketli dalgakılavuzu ile mekanik eyleyici arasındaki bağlantı, sistemde ek çarpraz-konuşmaya (cross-talk) sebep olacağı için, dalgakılavuzu düşük-kayıplı eliptik dalga kılavuzları yardımıyla merkezinden tutularak neredeyse eşdeğer fonksiyon kalitesine sahip çarpraz-konuşmanın önüne geçilebilecek olan iki ODC bölüme ayrıştırılmıştır.

ODC boyunca optik güç değişimi, daha yüksek hareket aralıkları için kullanılabilir, fakat üretim sınırlarına göre 200nm'den daha kısa mesafeli ODC'lerin deneysel olarak gerçeklenmesi zor ve yüksek maliyetlidir. Diğer taraftan, daha uzun ayrım mesafelerinde cihazı test etmek için eyleyici çok fazla sayıda tahrik parmaklarına ihtiyaç duyan en az 3µm hareket üretmelidir. Çünkü fabrikasyon bölgesi bir alt-alan (subfield)'da sınırlı olmaktadır (Elektron Hüzme Litografi Sistemi kullanımı nedeniyle) ve parmak sayılarının arttırılabilmesi de aynı nedenden ötürü mümkün değildir. Alternatif olarak, iki kolundan birinde bir optik yönlü bağlaştırıcıya sahip Mach-Zehnder İnterferometresi'ne dayanan yeni bir cihaz nümerik olarak çalışılmış ve tasarımı tamamlanmıştır. CMT'ye göre bir optik yönlü bağlaştırıcı, mesafe ve uzaklığa bağlı olarak çıkış ışık fazını değiştirebilir. Bu nedenle, MZI'nın çıkışındaki faz farkı algılama amacıyla kullanılabilir. FDTD simülasyonları, cihazların kısa ve uzun mesafelerde yüksek ve düşük hassasiyetli sensör olarak kullanılabileceklerini göstermiştir.

Cihazlar bir SOI pul üzerine kaplanan PMMA katmanı üzerine desenlenmiştir. Doğru litografi dozu birkaç kontrollü yazma denemesi ile bulunmuştur. Daha sonra, giriş bağlaştırıcı dalgakılavuzu, çıkış dalgakılavuzu, tarak tahrik elemanı ve elektriksel bağlantıları içeren komple bir cihaza sahip olmak için birkaç alt-alan ayrı ayrı PMMA üzerine desenlenmiş ve dikkatli bir şekilde bağıl olarak hizalanmıştır. Daha sonra, 30nm-kalınlığa sahip Cr katmanı PMMA üzerine kaplanmış ve kalan PMMA ise puldan ayrıştırılmıştır (lift-off). Cihaz Silisyum katmanı ICP-DRIE yardımıyla SiO_2 katmanına kadar kazınmış, ve Cr katmanı sensör cihazların üzerinden kaldırılmıştır. Havada asılı bulunacak hareketli mekanik kısımları serbestleştirmek için cihazlar buhar HF asitine maruz bırakılmışlardır. Hareket kaynağı olarak kullanılan mikro-tarak tahrik elemanlarına bağlı birkaç farklı yerdeğişimi sensörü cihaz üretilmiştir.

10µm, 12.5µm, ve 17.5µm uzunluğa sahip Mach-Zehnder Interferometresi (MZ Interferometer) esaslı sensör cihazlar ile birlikte 10µm ve 15µm uzunluktaki ODC esaslı cihazların testleri yapılmıştır. MZ esaslı cihazlar için 1550nm dalgaboyunda 60nm'den küçük yerdeğişimlerinde 4dB zıtlık değerine erişilmiştir. 15µm-uzunluktaki bir ODC'de ise 70nm mesafe civarında 25nm'den daha küçük bir yerdeğişimiyle çıkış sinyalinde 15dB'den daha yüksek bir zayıflamaya ulaşılmıştır. Cihazların spektral yanıtlarının mesafelere çok yüksek duyarlılık gösterdikleri ölçümlerden anlaşılmıştır. Örneğin, 12.5µm bağlaşma uzunluğuna sahip bir MZ cihazının spektral yanıtındaki en küçük değer üzerinde, mesafe 60nm'den 110nm'ye getirildiğinde 17nm'lik bir kızıl-kayma (red-shift) gerçeklenebilmiştir. ODC esaslı cihazlar ayrıca ilginç spektral karakteristik özellikler göstermektedirler. Kısa mesafelerde çalışılırken ODC uzunluğu yüksek tutulursa, mesafede yapılacak küçük değişimler (birkaç nanometre kadar) çıkış sinyalinde büyük zayıflamalar veya artımlara yolaçabilmektedir. 125nm mesafedeki 15µm uzunluğa sahip bir ODC'de 1540nm dalgaboyunda mesafe 90nm'ye düşürülerek 25dB'den daha yüksek zayıflama mertebelerine ulaşılabileceği de gösterilmiştir.

1. INTRODUCTION

Optical Directional Couplers (ODCs) are integrated as building blocks in various photonic circuits and optical devices. Several research groups have deployed ODCs as polarization beam splitters [1-5] due to their simplicity in design and fabrication. Directional couplers have been designed as optical power splitters or combiners as well [6-7]. ODCs are utilized in channel dropping lattice filters as WDM photonic devices which are easier to obtain a wide Free Spectral Range (FSR) compared to ring resonator channel add-drop filters [8]. Micro-ring assisted ODCs are shown to have wide range of spectral characteristics [9], but their structures are more sensitive to fabrication imperfections than those without micro-ring. Directional couplers recently have received great attention in optical MEMS and NEMS devices as well, and have been implemented as nanomechanical motion detectors [10], phase shifters [11], frequency and wavelength selective components [12], optomechanical switches [13] and interferometric devices [14]. The exponential dependency of the evanescent field bounded by the parallel waveguides on their separation is used to control the gradient forces between. the nanomechanical beams [15-16]. ODCs are also employed as integrated chemical and biological sensors [17-18].

Theoretical and experimental characteristics of compact ODCs are not investigated very much in detail although they are essential elements in high-density optoelectronic circuits. Integration of passive photonic devices with electronic components requires compromises that reduce the device performance due to the physical limitations in complex optical devices.

In this thesis, behavior of ultra-compact ODCs as simply configurable devices is investigated toward CMOS compatible nanophotonic circuits for optical signal processing and optomechanical systems. Use of high refractive index contrast of Silicon-on-Insulator (SOI) makes the light confinement stronger in Si waveguides enabling the use of smaller core dimensions. Although such smaller dimensions increase the cost and complexity in the fabrication of nano-wire waveguides [19-20], understanding such characteristics as power transmission spectra, and effects of length and separation of the nano-wires on the transmission will allow one to achieve the same performance with simpler fabrication. Such an understanding of the parameters of compact integrated ODCs can lead to reduced circuit footprint without compromising quality in optical systems.

Finally, based on the ODCs investigated previously in this thesis, structures are proposed, simulated and confirmed by experimental results for optical sensing and telecommunication applications.

2. FUNDAMENTALS OF WAVEGUIDE-TO-WAVEGUIDE COUPLING

The field that extends beyond the waveguide is referred to as the evanescent field. We can use the overlap of this field with the waveguides to couple light from one waveguide to the other if the waveguides are sufficiently close to each other. A very useful simplified analysis of such a structure is presented in [21]:

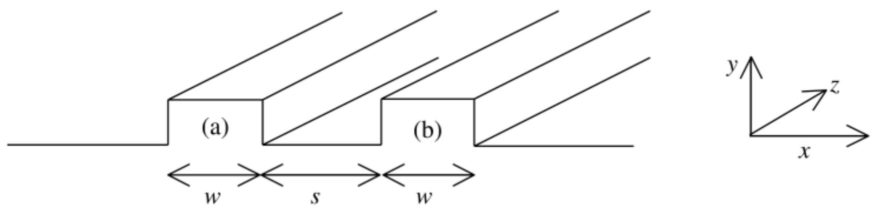

Figure 2.1: Two identical waveguides with width w and separation distance s [21].

Suppose two identical waveguides (a) and (b) in Fig. 2.1, with width w, and are separated with the distance s. Let the field of waveguide (a) be as:

$$E_a = a_0(x,y)e^{j\beta z}e^{j\omega t} \tag{2.1}$$

And the field of waveguide (b) is similarly:

$$E_b = b_0(x,y)e^{j\beta z}e^{j\omega t} \tag{2.2}$$

The interaction of fields can be described using coupled mode theory, and as a simple version of the equations can be written as:

$$\frac{da_0}{dz} = \kappa b_0 \tag{2.3}$$

$$\frac{db_0}{dz} = -\kappa a_0 \tag{2.4}$$

where κ is the coupling coefficient. Here it is assumed that the waveguides are identical, there is no attenuation and no directional coupling, hence there is a phase match between the modes in each waveguide. Assume the waveguide (b) is excited at z = 0 and the waveguide (a) is not:

$$a_0(z = 0) = 0 \quad \textbf{(2.5)}$$

$$b_0(z = 0) = c_0 \quad \textbf{(2.6)}$$

Then the solution of the equations 3 and 4 will be in the form of:

$$a_0(z) = c_0 \sin(\kappa z) \quad \textbf{(2.7)}$$

$$b_0(z) = c_0 \cos(\kappa z) \quad \textbf{(2.8)}$$

This means that the fields in the waveguides are sinusoidal and the increase in one will cause the other one to decrease. Since the fields are periodic, complete transfer of power will occur when the length of coupled waveguides is an integer multiple of $\pi/2\kappa$ which is called coupling length $L_\pi = m\pi/2\kappa$ where m can take 1, 2, 3, ... values. When the structure couples half of the energy to the other waveguide it is called 3-dB coupler which the coupling length will be $L_c = L_\pi/2 = m\pi/2\kappa$.

κ determines the coupling efficiency which is given as [21]:

$$\kappa = \frac{2k_{xc}^2 k_{xs} e^{-k_{xs}\, s}}{\beta w (k_{xs}^2 + k_{xc}^2)} \quad \textbf{(2.9)}$$

where k_{xc} is propagation constant of the core in x direction, k_{xs} is the decay constant between waveguides in x direction, w is the width of the waveguides and s is the separation distance between waveguides.

Eq. 2.9 shows that the coupling coefficient is exponentially related to separation distance between the two waveguides and the coupling efficiency will decrease exponentially when the separation distance increases with the ratio of decay constant.

Optical couplers could be used as building block in the other photonic devices as input or output. Mach-Zehnder interferometer can be one of the devices which use optical coupler as an output.

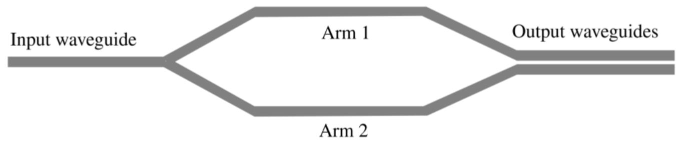

Figure 2.2 : Optical coupler as the output of Mach-Zehnder interferometer [21].

Based on the phase shift caused by Mach-Zehnder interferometer and the coupling length of the output waveguides the optical power in each waveguide can vary according to coupled mode theory. Then the device can act as an optical switch.

Optical ring resonators are one of the key devices which use waveguide to waveguide coupling. The optical coupler can be used as an input to couple the optical power into the ring resonator. The ratio of power coupling into the ring resonator can be controlled by determining the length of the coupling waveguides.

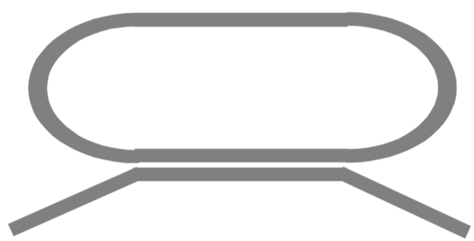

Figure 2.3: Optical coupler as the input of the ring resonator [21].

3. OPTICAL COUPLERS IN LITERATURE:

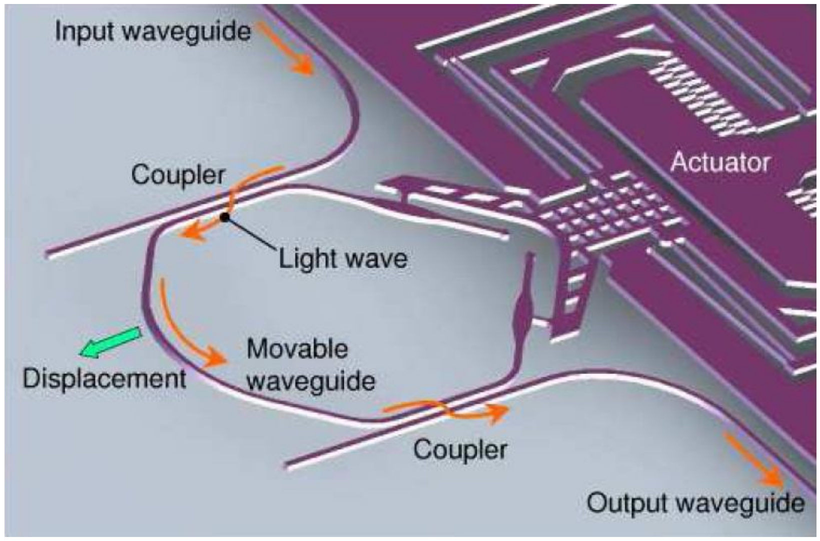

Figure 3.1: Submicron silicon waveguide phase-shifter with an ultra-small actuator. [11]

Since silicon has great optical and mechanical properties SOI devices have been ubiquitously considered in recent years, its high refractive index compared to silicon dioxide has made it suitable to design submicron, low-loss, single mode nanophotonic waveguides [10]. Silicon waveguides are very attractive materials for waveguiding purposes, because of the large refractive index difference between silicon and silicon dioxide substrate, light is strongly confined into the silicon waveguide core [20]. Therefore, the possible bending radius of silicon waveguides can be minimized with respect to the other conventional waveguiding materials.

3.1 Applications in Optical circuits

In [20], a sub-wavelength optical directional coupler is fabricated and characterized. The dimensions of fabricated devices are shown in the Fig. 3.2. The DCs are made of two silicon channel waveguides with the square shaped 0.3µm×0.3µm cross section fabricated on silicon-on-insulator wafer with 1-µm-thick buried silicon dioxide layer on silicon substrate.

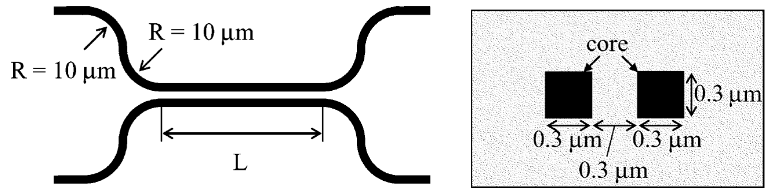

Figure 3.2: Top and cross sectional view of the silicon waveguide directional coupler [20].

The waveguide cores are 0.3μm apart of each other. The S shaped waveguides are connected to both input and output ports of the waveguides in order to prevent confining the ambient and noisy light caused by inappropriate fiber optic coupling to the input waveguides into the coupler's waveguide. The radius of the curvature of the S shaped waveguides is 10μm which makes the overall length of the device (40+L) μm, where L is the coupled-waveguide length. The coupling lengths calculated for separation distance of 300nm and 200nm are 10μm and 4.9 μm, respectively. The coupling length is a little longer when the TE-mode light is launched through the parallel waveguide.

A cutback method was implemented to measure the propagation loss of the silicon waveguide, and tapered optical fibers were used to couple light to the input of the waveguide and measure the light reached the output.

The output light powers for both perpendicular and parallel polarized light field were observed to be sinusoidal and complementary for two output ports. The coupling length was estimated to be 10μm for electric field perpendicular to the substrate and to be 11μm for the electric field parallel to the substrate. DCs with longer coupled waveguides L = 100μm were fabricated and the wavelength dependence of the transmittance obtained from both calculation and measurements for the two cross and parallel output ports is plotted in Fig. 3.3a and b. The ripples in the Fig. 3.3a are caused by fabry-perot reflection, because both facets of the directional couplers were uncoated.

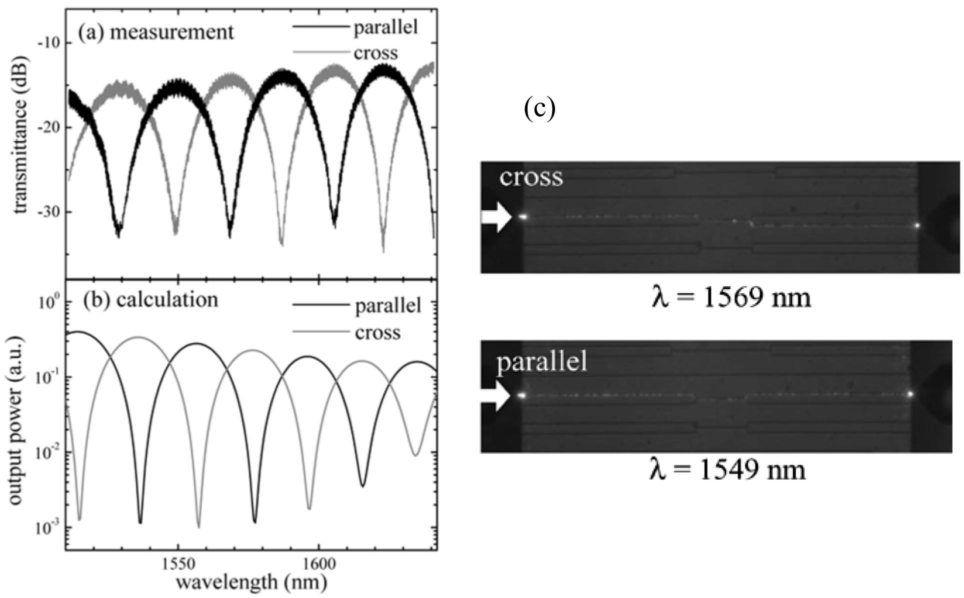

Figure 3.3: Wavelength dependence of light output from a 100-µm-long directional coupler. (a) Measured transmittance. (b) Calculated output power. (c) Light scattered from the top surface of the device. [20]

Herein, an experimental method for characterization of coupled waveguides by normal-mode excitation will be described.

In [22] a novel method is presented to characterize optical directional coupler in Ti:$LiNbO_3$ based on excitation of normal modes and individual-waveguide-modes of symmetric optical directional couplers.

Method 1: Coupling coefficient from normal structure modes:

We can express any wave in a waveguide as the superposition of two symmetric and antisymmetric modes. Consider the electric field in one of the waveguides in figure6. We can express the transverse electric field in terms of symmetric mode and antisymmetric modes as:

$$E_t(x,z) = M_s(z)E_s(x) + M_a(z)E_a(x) \quad \textbf{(3.1)}$$

where $E_s(x)$ and $E_a(x)$ are symmetric and antisymmetric electric field modes, respectively, and $\mathrm{M_s(z)}$ and $\mathrm{M_a(z)}$ are complex functions.

The intensity of the electric field $E_t(x,z)$ at the propagation length z according to the definition is:

$$I(x,z) = E_t(x,z)E_t^*(x,z)$$
$$= |M_s(z)|^2 E_s^2(x) + |M_a(z)|^2 E_a^2(x) \quad \textbf{(3.2)}$$
$$+ 2\, Re\{M_s(z)M_a^*(z)\}E_s(x)E_a(x)$$

The propagation constants by definition can be expressed by an exponential function:

$$M_s(z) = M_s(0)e^{-j\beta_s z} \quad \textbf{(3.3)}$$

$$M_a(z) = M_a(0)e^{-j\beta_a z} \quad \textbf{(3.4)}$$

where β_s and β_a are propagation constants for symmetric and antisymmetric modes, respectively. Hence, by substituting the Eq. 3.3 and Eq. 3.4 in Eq. 3.2, it can be written:

$$I(x,z) = |M_s(z)|^2|E_s(x)|^2 + |M_a(z)|^2|E_a(x)|^2$$
$$+ 2\, cos(2\kappa z + \Phi(0))\, |M_s||M_a|E_s(x)E_a(x) \quad \textbf{(3.5)}$$

where by definition $\kappa = \frac{1}{2}(\beta_s - \beta_a)$ and $\Phi(0)$ is the phase difference caused by initial excitation field. Amplitudes$|\mathrm{M_s}|$ and $|\mathrm{M_a}|$ can be determined by the initial conditions.

Method 2: Coupling coefficient from individual waveguide modes:

According to coupled mode theory for two waveguides which are closed enough to each other the transverse electric field can be described as:

$$E_t(x,z) = A(z)E_1(x) + B(z)E_2(x) + G(x,z) \quad \textbf{(3.6)}$$

Where $E_1(x)$ and $E_2(x)$ the individual waveguide mode fields in waveguide 1 and 2, respectively and $A(z)$ and $B(z)$ are the complex amplitudes of the individual waveguide modes. Since $E_1(x)$ and $E_2(x)$ do not span all the electric field in waveguides then term $G(x,z)$ is introduced as the residual electric field. Relative size of the term $G(x,z)$ compared to the other terms in Eq. 3.6 determines the reliability of the equation as a model of the system.

According to the coupled mode theory $A(z)$ and $B(z)$ can be determined from the equations:

$$\frac{dA(z)}{dz} = j\beta_1 A(z) + j\kappa_{12} B(z) \tag{3.7}$$

$$\frac{dB(z)}{dz} = j\beta_2 B(z) + j\kappa_{21} A(z) \tag{3.8}$$

where β_1 and β_2 are the propagation constants of the fields in waveguide 1 and 2, respectively, and κ_{12} is the coupling coefficient from waveguide 2 to waveguide 1, and κ_{21} is the coupling coefficient from waveguide 1 to waveguide 2. For the identical waveguides the propagation constants and coupling coefficients are identical, as well:

$$\beta = \beta_1 = \beta_2 \tag{3.9}$$

$$\kappa = \kappa_{12} = \kappa_{21} \tag{3.10}$$

The solution of Eq. 3.7 and Eq. 3.8 with the initial condition $A(z=0) = A_0$ and $B(z=0) = 0$ are in the form of:

$$A(z) = A_0 \cos(\kappa z)\, e^{-j\beta z} \tag{3.11}$$

$$B(z) = -jA_0 \sin(\kappa z)\, e^{-j\beta z} \tag{3.12}$$

By neglecting the residual fields Eq. 3.6 can be written approximately as:

$$E_t(x,z) \approx A(z)E_1(x) + B(z)E_2(x) \quad \textbf{(3.13)}$$

The intensity of electric field at z according to Eq. 3.13 can be written as:

$$\begin{aligned} I_t(x,z) &= E_t(x,z)E_t^*(x,z) \\ &\approx |A(z)|^2|E_1(x)|^2 + |B(z)|^2|E_2(x)|^2 \\ &+ 2\,Re\{A(z)B^*(z)E_1(x)E_2(x)\} \end{aligned} \quad \textbf{(3.14)}$$

Light intensity $I_t(x,z)$, $E_1(x)$ and $E_2(x)$ can be measured directly from the experiment for every propagation distance *z*, then by applying a fitting method the coefficients of Eq. 3.14 can be estimated. The behavior of $|A(z)|^2$ and $|B(z)|^2$ is sinusoidal for different propagation distances z, then the coupling coefficient κ of the two waveguides can be easily calculated from the periodicity of the $|A(z)|^2$ and $|B(z)|^2$.

Thereafter, relation between the amplitudes of individual waveguide modes $A(z)$ and $B(z)$ and the normal structure modes are discussed, and it will be shown that how one can be obtained from the other one.

According to two description of electric field along the *x* and propagation distance *z*:

$$\begin{aligned} \mathrm{E_t(x,z)} &= \mathrm{M_s(z)E_s(x) + M_a(z)E_a(x)} \\ &= \mathrm{A(z)E_1(x) + B(z)E_2(x) + G(x,z)} \end{aligned} \quad \textbf{(3.15)}$$

Since symmetric mode and antisymmetric mode are orthogonal to each other the integral of their complex conjugate multiplication is zero, hence:

$$\int E_a(x)E_s^*(x)dx = 0 \quad \textbf{(3.16)}$$

$$\int E_s(x)E_a^*(x)dx = 0 \quad \textbf{(3.17)}$$

In order to keep the fields normalized:

$$\int E_a(x)E_a^*(x)dx = \int E_s(x)E_s^*(x)dx = 1 \qquad \textbf{(3.18)}$$

And the overlap integrals are defined as:

$$\int E_1(x)E_2^*(x)dx = C \qquad \textbf{(3.19)}$$

$$\int E_1(x)E_s^*(x)dx = \int E_2(x)E_s^*(x)dx = I_s \qquad \textbf{(3.20)}$$

$$\int E_1(x)E_a^*(x)dx = -\int E_2(x)E_a^*(x)dx = I_a \qquad \textbf{(3.21)}$$

If we multiply Eq. 3.15 by $E_1(x)$ and then integrate both sides:

$$A(z) + B(z)C = M_s(z)I_s + M_a(z)I_a \qquad \textbf{(3.22)}$$

Similarly If we multiply Eq. 3.15 by $E_2(x)$ and then integrate both sides:

$$A(z)C + B(z) = M_s(z)I_s - M_a(z)I_a \qquad \textbf{(3.23)}$$

Then from the last two equations $\mathrm{M_s(z)}$ and $\mathrm{M_a(z)}$ can be calculated in terms of A(z) and B(z):

$$M_s(z) = \frac{\big(A(z) + B(z)\big)(1 + C)}{2I_s} \qquad \textbf{(3.24)}$$

$$M_a(z) = \frac{\big(A(z) - B(z)\big)(1 - C)}{2I_a} \qquad \textbf{(3.25)}$$

If we multiply the Eq. 3.15 by $E_s(x)$ and then integrate both sides and do the above procedure again we have:

$$A(z) \approx \frac{M_s(z)}{2I_s} + \frac{M_a(z)}{2I_a} \quad \textbf{(3.26)}$$

$$B(z) \approx \frac{M_s(z)}{2I_s} - \frac{M_a(z)}{2I_a} \quad \textbf{(3.27)}$$

$E_1(x)$ and $E_2(x)$ are orthogonal to residual field $G(x,z)$. More details on how the last two equations are calculated are given in [22].

By substituting the last two equations in the Eq. 3.24 and Eq. 3.25 we can easily find that:

$$C \approx |I_s|^2 - |I_a|^2 \quad \textbf{(3.28)}$$

To experimentally excite the normal modes and individual waveguide modes, If the fiber optic illumination of the coupled waveguides occurs exactly at the center of two coupled waveguides, then the waveguides will be excited symmetrically because the light fields propagating through coupled waveguides are in phase. Hence, the light intensity at the output of two waveguides corresponds to the symmetric light mode intensity $|E_s(x)|^2$. Figure 3.4a shows schematically how to excite the symmetric field modes.

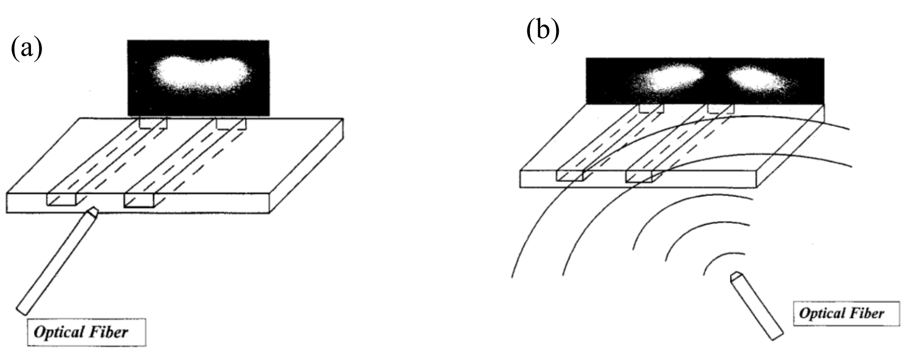

Figure 3.4: (a) Excitation of symmetric mode. (b) Excitation of antisymmetric mode [22].

In order to excite the antisymmetric field modes we tilt the fiber optic illumination in the same plane of the waveguides until we observe an exactly $\lambda/2$ phase shift between the lights reaching the inputs of the two waveguides. This condition is achievable by increasing the angle of the optical fiber with respect to the waveguides core axis until observing the light intensity at the output of the two waveguides which is exactly symmetric but having zero intensity at the center point between the two waveguides. Figure 3.4b shows how to excite the antisymmetric modes and the light intensity for antisymmetric mode $|E_a(x)|^2$ at the output of the waveguides.

In [23] a polarization-insensitive directional couplers based on SOI wire waveguides is proposed. By definition birefringence in a wire waveguide is determined by

$$B = n_{eff}^{TE} - n_{eff}^{TM} \tag{3.29}$$

where n_{eff}^{TE} and n_{eff}^{TM} are the effective refractive indices of waveguide for TE and TM polarized light field, respectively.

Consider the silicon waveguide with width w on a SiO_2 substrate. In this report the fabrication tolerance is shown by non-vertical side-walls. The dependence of birefringence for a silicon wire waveguide with the height of 290nm with respect to the waveguide width is given in Fig. 3.4.

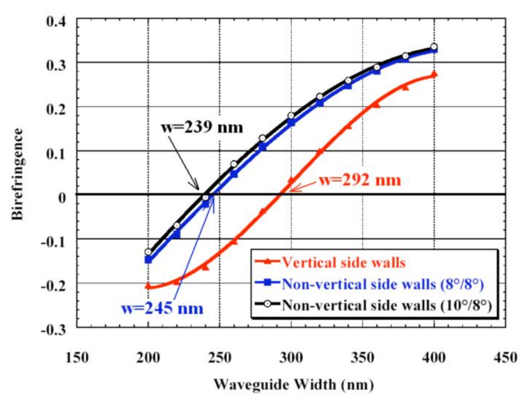

Figure 3.5: Birefringence dependence on width of a SOI waveguide with height of 290nm [23].

Birefringence curve for different values of waveguide width for vertical side walls, symmetrical non-vertical side walls inclined by 8° and non-symmetrical non-vertical side walls inclined by 8° and 10° is plotted in Fig 3.5. The figure shows that the birefringence is highly dependent to waveguide width and as the fabrication tolerance increases the birefringence value changes considerably. Fabrication tolerance also changes the zero birefringence condition.

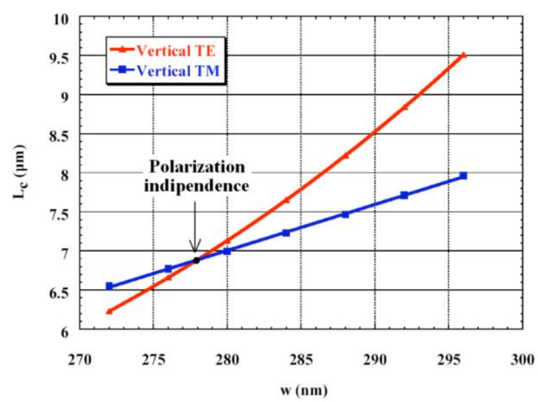

Figure 3.6: Coupling length dependence on vertical side-wall waveguide width for both TE and TM polarized light field when h = 290nm and g = 300nm [23].

Considering both waveguides of the coupler have vertical side-wall with the height of 290nm and the separation distance of 300nm. To obtain a polarization-insensitive structure both curves of coupling distance dependence on waveguide width for both TE and TM polarized light wave are plotted in Fig. 3.6. Then, the polarization-insensitive waveguide width is obtained to be at $w = 278nm$ with corresponding coupling length $L_c = 6.88\ \mu m$.

3.2 Applications in optical sensors

The high stiffness and low mass density of silicon [10] has made it an attractive material for mechanical sensing. Both mechanical and optical properties of silicon are great factors to choose silicon as the sensing material and also it has provided such an area to design sensors that combine mechanical motion, force and mass with photonics in order to design more sensitive, accurate, noise-independent integrated devices. Also photonic silicon structures are compatible with CMOS electronic devices and they are extremely low-cost with comparison to the similar electronic devices. Photonic sensor devices are potential devices for robust and noise-insensitive applications and they can also be used in harsh environments where remote sensing is necessary.

In recent works done on optical directional couplers it has been shown that nanomechanical motion can be sensed with high sensitivity and high bandwidth by means of strong coupling between nanowire channel waveguides [10]. Also multichannel directional couplers (MCDCs) can be considered as sensing devices and they have been investigated as evanescent field optical sensor by means of changing the refractive index of the analyte between and surrounding the waveguides [24]. Other similar techniques such as nanomechanical proximity perturbation in silicon directional couplers have been utilized as a switching device in high density photonic integrated devices [13].

Furthermore, other photonic structures like fabry-perot microcavities have gained significant attraction in integrated photonic devices namely in optical filtering, microphone structures, pressure sensing elements and accelerometer sensors [25]. For instance in [25] a novel in-plane silicon-on-insulator optical accelerometer based on fabry-perot microcavity is presented which provides some advantages in terms of size, weight, reliability and power consumption comparing to other conventional optical accelerometers.

In [10] a method for detection of nanomechnical motion using the evanescent light wave coupling between the coupling waveguides is presented, Fig. 3.7. They showed that their technique works for nanomechanical resonators with more sensitivity than the conventional optical methods presented.

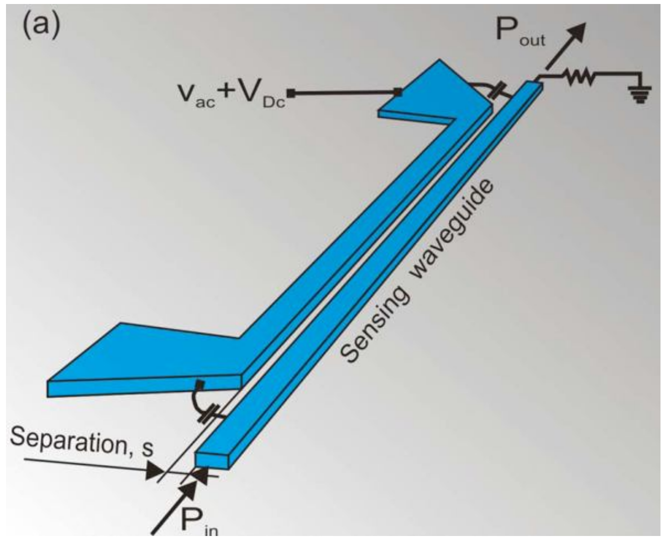

Figure 3.7: Schematic drawing of the device under the test [10].

The nanomechanical motion detection is achieved by coupling the evanescent light field from one waveguide into the mechanical resonator. According to coupled mode theory the amount of light field power abled to couple to the other waveguide varies upon the coupling length, separation distance and amount of optical mode penetration to the other waveguide.

In [24] a new geometry to implement directional couplers as an evanescent field optical sensor is presented. In this method a sensor system is achieved by means of the analyte between an array of waveguides and using the fact that the evanescent light out of the waveguides decays exponentially through the ambient material, hence this system can be considered as an effective index change detector. This system can provide a simpler and more robust sensing device than a Mach-Zehnder, and also since it utilizes the exponential dependence of coupling between two waveguides coupled, higher sensitivity can be achieved [24].

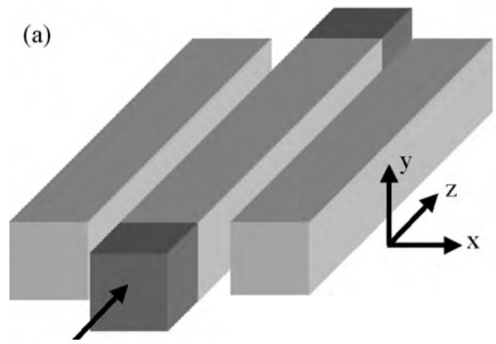

Figure 3.8: Schematic structure of a 3-channel directional coupler fed from the center waveguide [24].

For two symmetric identical waveguides in close proximity with each other the approximated coupling coefficient is given by [24]:

$$\kappa = 2\sqrt{n_c^2 - n_a^2}\,\frac{k}{\beta w_{eff}}\exp\left\{-\sqrt{\beta^2 - (n_a k)^2}\,(s + w/2)\right\} \tag{3.30}$$

Where n_c is the waveguide core refractive index, n_a is the analyte refractive index, β is the unperturbed propagation constant of the two identical waveguides, w_{eff} denotes the effective waveguide width, and k refers to the wave number.

Consider a 3-channel MCDC fed by the center waveguide, the field distribution is symmetric for both side waveguides, if we assume only coupling for the adjacent waveguide then the corresponding self-image length is [24]:

$$L_{center} = \frac{\pi}{\sqrt{2}\kappa} \tag{3.31}$$

According to the power of the light field along the waveguide the operating point can be chosen at the center of the linear region in order to achieve the most sensitivity and the largest possible dynamic range.

If we launch the light through one of the side waveguides then other supermodes will be excited along the waveguides. For a side-fed 3-channel MCDC the corresponding self-image length is [24]:

$$\mathrm{L_{side}} = 2\frac{\pi}{\sqrt{2}\kappa} = 2\mathrm{L_{center}} \quad \textbf{(3.32)}$$

The sensitivity of the sensor is defined as the change of the transmittance (T) for a change in analyte index n_a [24]:

$$S = \left.\frac{\partial T}{\partial n_a / n_{a(ref)}}\right|_{n_a = n_{a(ref)}} = n_{a(ref)} \left.\frac{\partial T}{\partial n_a}\right|_{n_a = n_{a(ref)}} \quad \textbf{(3.33)}$$

To have the largest sensitivity the sensor must be biased at the greatest slope which means the operating point where the sensor is working will be biased at 50% transmittance.

In Fig. 3.9 the calculated transmittance as a function of analyte refractive index is plotted. The behavior of the device is periodic for the less values of the analyte refractive index but according to equation 40 the dependence of coupling efficiency on refractive index is exponential which means that the exponential term for the greater values of refractive index will appear in the transmittance.

For both devices the operating point is determined to be at the middle of the linear region in order to gain the maximum sensitivity. If we consider the calculated sensitivity at the operating point for both devices to be S then according to equation 41 the center-fed 3-channel MCDC is shorter than directional coupler by a factor of $\sqrt{2}$ which means that at the same operating point the center-fed 3-channel MCDC will give more sensitivity as a sensor of analyte change.

Then the performance of a side-fed 3-channel MCDC is compared with a center-fed 3-channel directional coupler. Figure 3.9 shows their transmittance dependence on the analyte refractive index change.

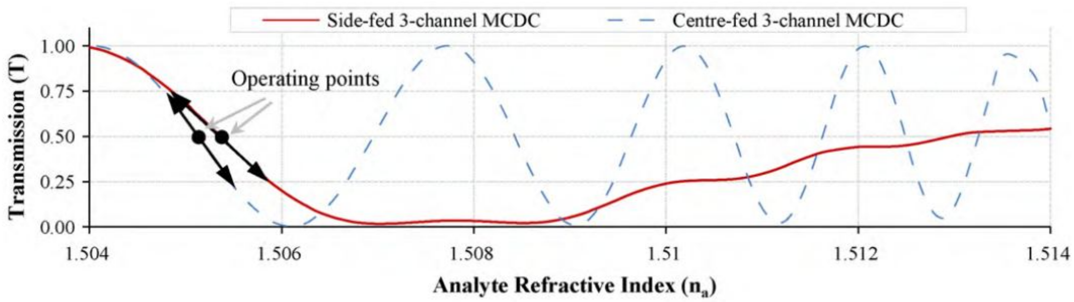

Figure 3.9: Transmittance of a side-fed 3-channel MCDC and a center-fed 3-channel directional coupler as a function of analyte refractive index. The operating points are determined for both devices.

The operating points for both devices are set to be at the place which maximum sensitivity to analyte change is gained. Calculations showed that for the center-fed 3-channel directional coupler the sensitivity of the device was greater than the side-fed 3-channel MCDC with respect to analyte changes. The slope of the curve referring to the center-fed 3-channel directional coupler is greater than the slope of the curve corresponding to side-fed 3-channel MCDC.

In this work they also concluded that for higher sensitivity we need to achieve weaker coupling between the waveguides resulting in longer devices, hence there is always a tradeoff between sensitivity and device length. The highest sensitivity and the best performance were obtained from center-fed 3-channel directional coupler.

In [13] another application of changing the refractive index at the surrounding ambient of the directional couplers is presented. In this method by using the proximity perturbation of the dielectric between the two waveguides a switching device is fabricated.

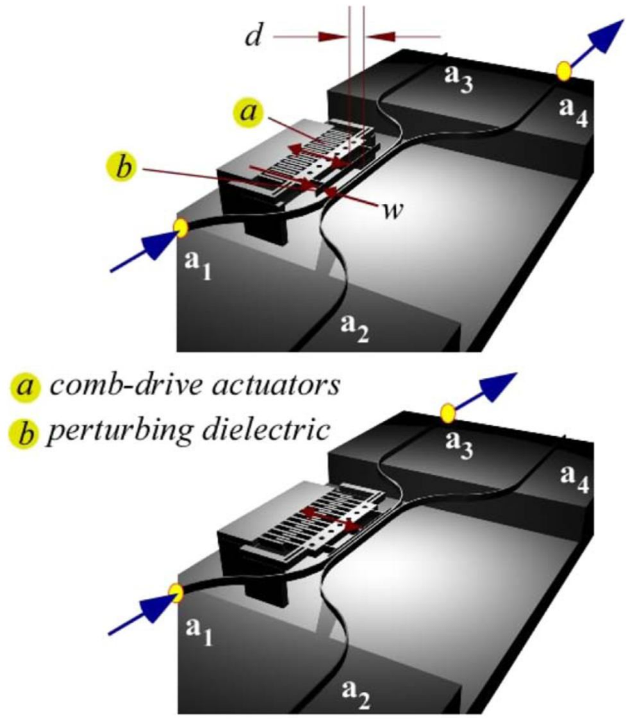

Figure 3.10: Schematic view of the device in unperturbed and perturbed states [13].

The whole structure is shown in Fig. 3.10; the system involves two 500nm × 200nm single mode silicon waveguides which construct the directional coupler with separation distance of 250nm and is perturbed via a 100-nm-wide dielectric which is able to move by means of a comb-drive actuator. The substrate is a silicon-on-insulator wafer with 205-nm single-crystal device layer on top of a 3μm buffer oxide layer [13].

The waveguide effective index of the waveguides is a function of cladding and core indices. Hence, it is possible to change the refractive index of the cladding by closing a dielectric material and then changing the effective refractive index of the waveguide. Changes in effective refractive index of waveguides will result in changes in coupling coefficients between the two waveguides. Therefore it is possible to tune the amount of field power transferred between the waveguides by perturbing the evanescent field around the waveguides.

For the purpose of actuation two electrostatic methods can be used, one is to use electrostatic capacitance plates to move the dielectric, and the second one is to use comb drives. In this work comb-drive actuator was selected, since comb-drive actuators use materials that are more compatible with standard CMOS devices.

4. PHYSICAL CHARACTERISTICS

4.1 Modal analysis

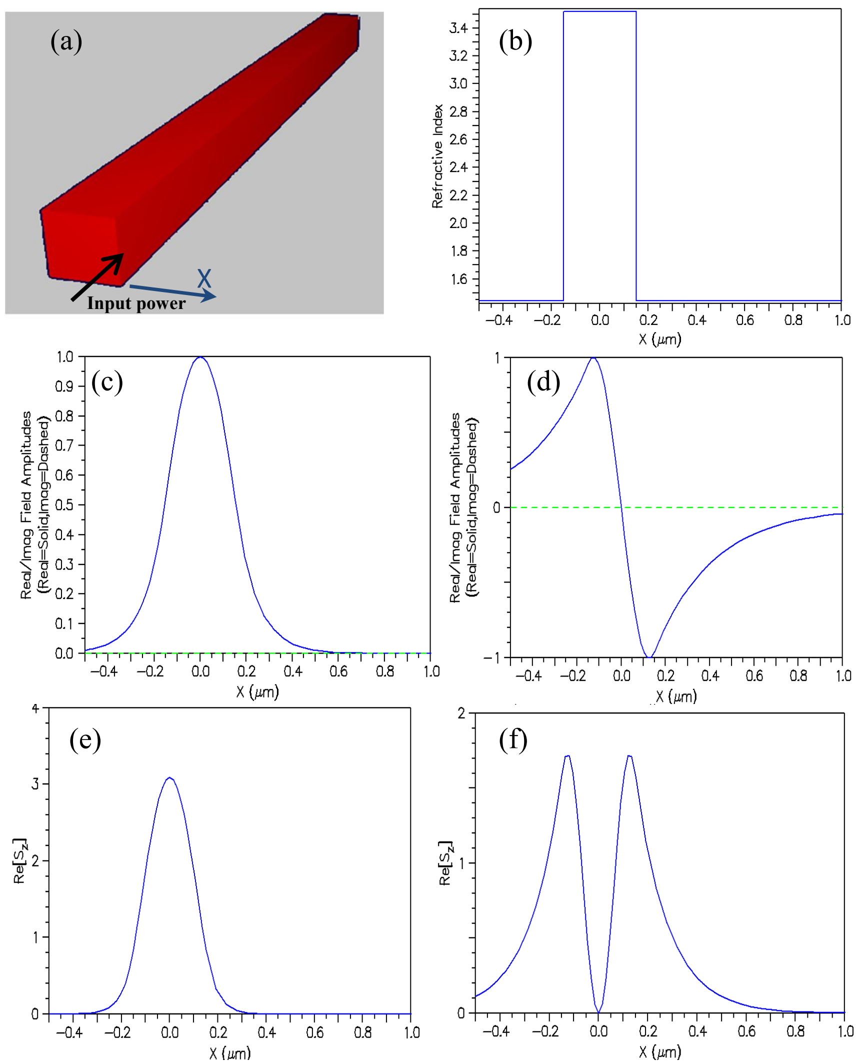

Figure 4.1: First and second electric field mode profiles of a single waveguide (Real and Imaginary values are illustrated by solid and dashed lines, respectively), (a) 3D schematic view of a single rectangular waveguide, (b) Refractive index profile of the waveguide along x direction, (c) First mode profile of electric field, (d) Second mode profile of electric field, (e) Real part of the electrical power for the first mode, (f) Real part of the electrical power for the second mode.

It is possible to express any wave in a single-mode waveguide as the superposition of two symmetric and antisymmetric modes. For a single-mode rectangular waveguide with the 300nm-wide and 300nm-thick in cross-sectional geometry, the first and the second fundamental mode profiles of the electric field with the corresponding powers are calculated, and the calculated modes are plotted in Fig. 4.1.

For the two waveguides close enough to each other, the first two modes named symmetric and antisymmetric modes can be calculated. The cross-sectional geometry of both waveguides is chosen to be 300nm×300nm in order to satisfy the single-mode condition [20] and the separation between the two waveguides is 300nm. The first and the second mode profiles of the electric field with the corresponding powers for the two coupled waveguides are given in Fig. 4.2.

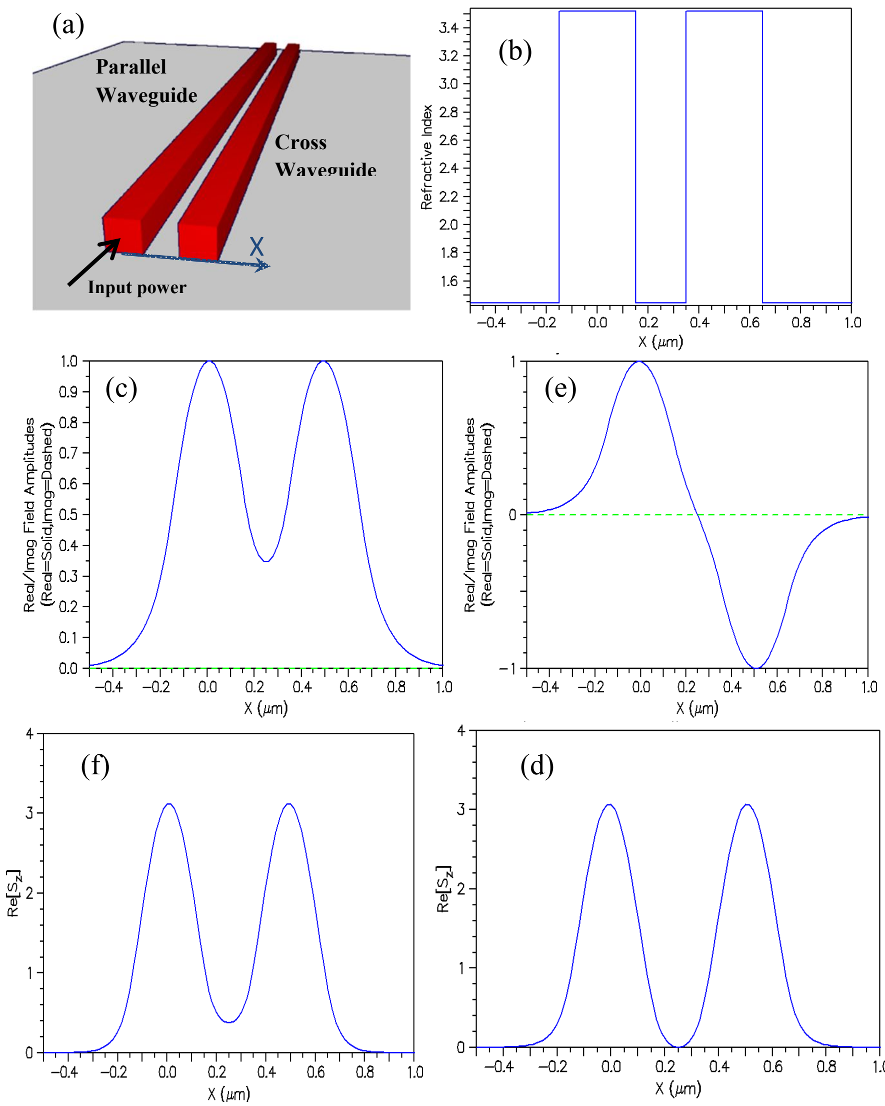

Figure 4.2: First and second electric field mode profiles of two coupled waveguides (Real and Imaginary values are illustrated by solid and dashed lines, respectively), a) 3D schematic view of two coupled waveguides, b) Refractive index profile of the waveguides along the x direction, c) First mode profile of electric field, d) Second mode profile of electric field, e) Real part of the electrical power for the first mode, f) Real part of the electrical power for the second mode.

Using Beam Propagation Method (BPM), coupling lengths between the two waveguides for different separation values have been calculated. E_x field of the fundamental mode along the two waveguides is as presented in Fig. 3. Figure 3b shows the E_x mode profile for the fundamental mode at the output of the two waveguides.

According to Coupled Mode Theory (CMT), the coupling length can be written as a function of separation distance such that:

$$L_c(s) = Ae^{Bs} \quad \textbf{(4.1)}$$

According to the BPM simulations conducted, the exponential fitted curve gives the values of the constants to be $A = 1.113$ m and $= 0.00731\ nm^{-1}$, hence the Eq. 4.1 can be rewritten as:

$$L_c[s(nm)] = 1.113\ e^{0.00731s}\ (\mu m) \quad \textbf{(4.2)}$$

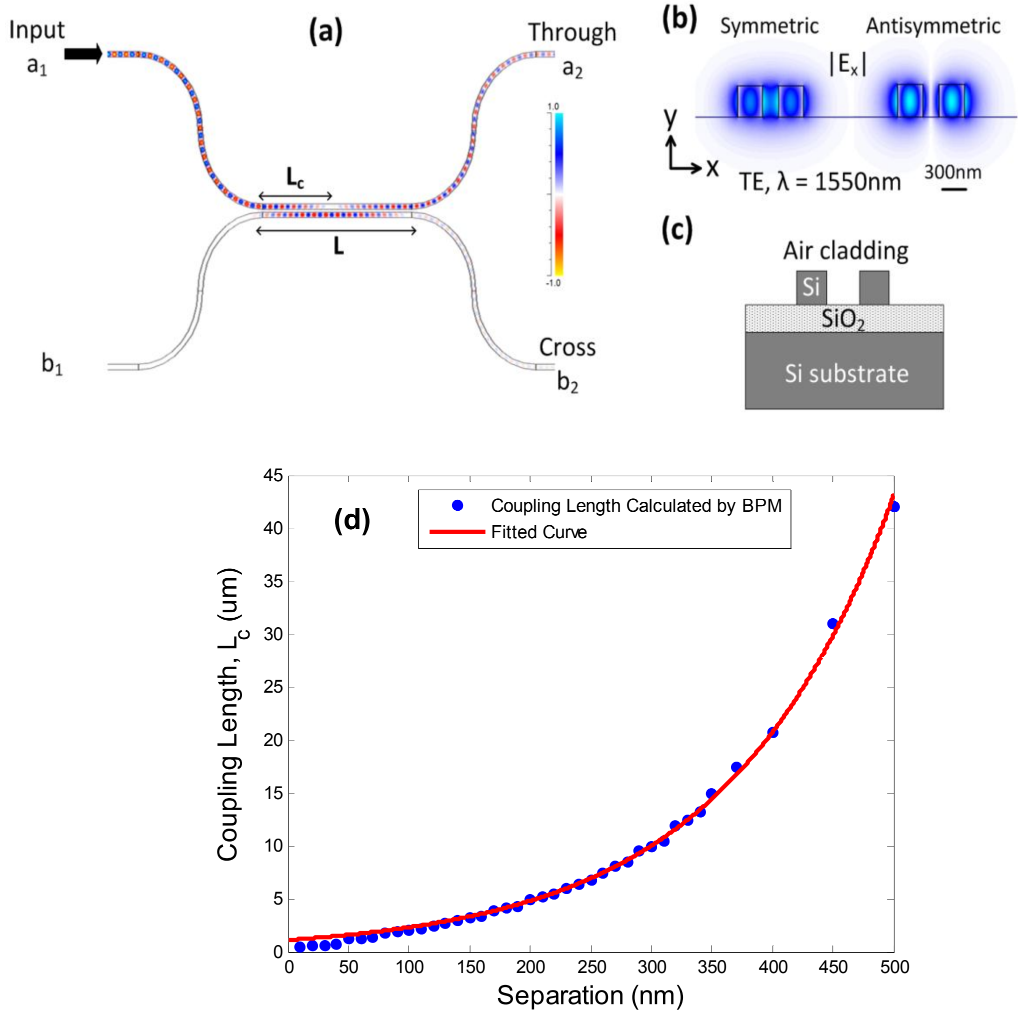

Figure 4.3: (a) Magnetic field distribution along an ODC where complete power transfer occurs between waveguides. (b) Absolute value of symmetric and asymmetric TE-mode profile distributions at 1550nm wavelength. (c) Cross-sectional view of an ODC on SOI wafer. (d) Coupling length of the directional coupler as a function of the separation between the waveguides, and its fitted curve.

Then the output powers at the parallel and cross ports as a function of separation distance can be calculated. Figure 4.4 shows how the output powers change when the separation between the waveguides of a 10- m directional coupler changes. Note that the sum of the output powers is always equal to one due to conservation of energy.

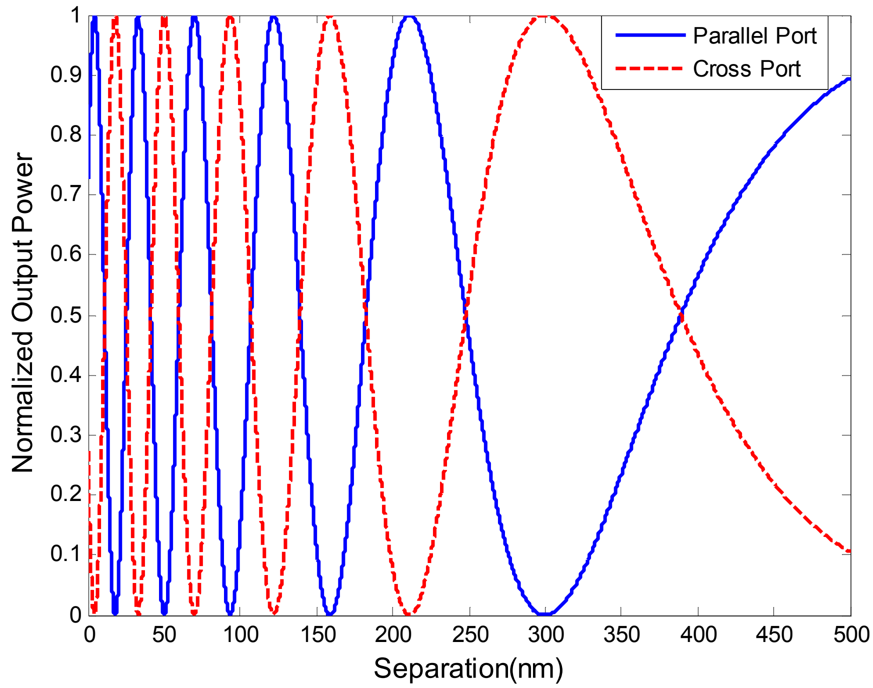

Figure 4.4: Normalized output powers at the parallel and cross ports of a 10- m directional coupler as a function of separation distance.

The above results correspond to an optical directional coupler with identical waveguides of 300nm-wide and 300nm-thick in cross-sectional geometry. The values of A and B are dependent to the waveguides geometry and can be calculated accordingly for different possible dimensions. Figure 4.5 illustrates the output power as both separation and length of the coupler.

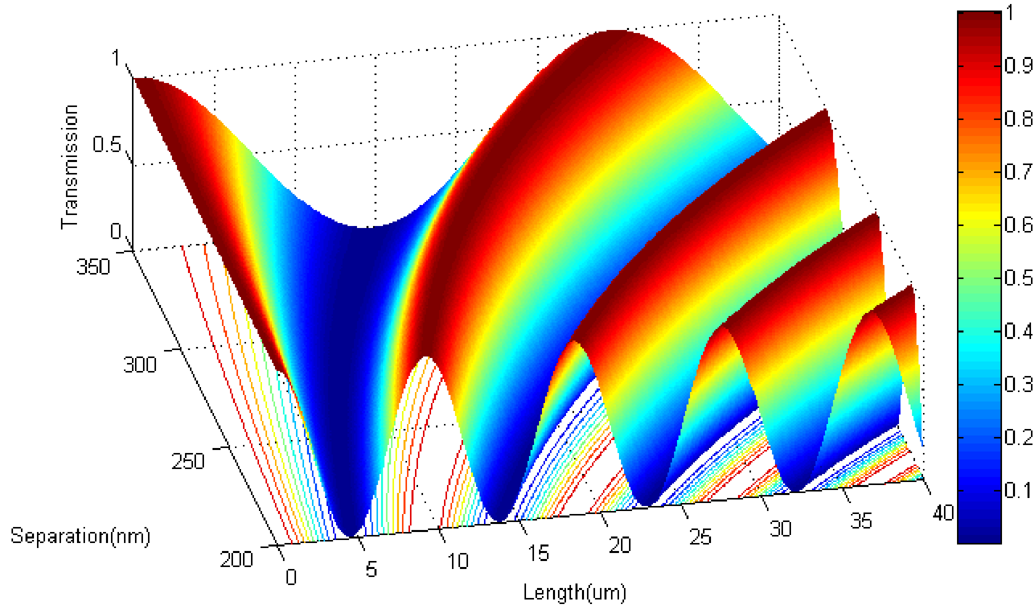

Figure 4.5: Transmission of directional coupler from the parallel port as function of separation and length of the waveguides.

4.2 Geometry analysis

Changing the cross-sectional geometry of the waveguides can cause significant changes on the coupling length. For a 300nm-separated directional coupler the dependence of coupling length on the width and thickness of the directional coupler has been simulated and the results are as presented in Fig. 4.6. Coupling length is found to be more sensitive to changes in the width of the waveguides when compared to changes in the thickness. In the range between 290nm to 310nm for both width and thickness, changes in thickness for a specific width can cause at most 1 μm change in the coupling length while for a constant thickness the coupling length can change more than 3μm.

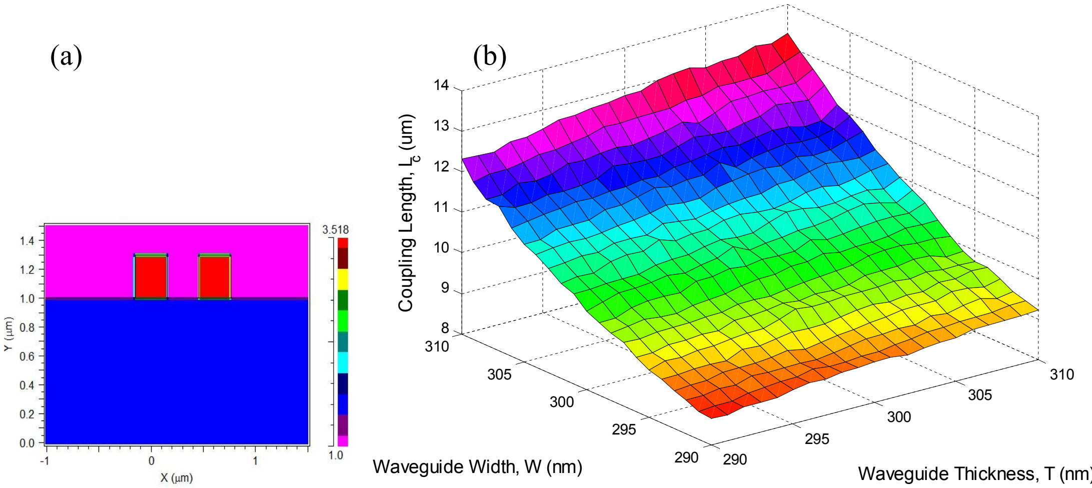

Figure 4.6: (a) Cross-sectional refractive index profile of a 300nm-separated directional coupler, (b) Coupling length of the directional coupler as a function of width and thickness.

For less than 150nm thickness coupling between the waveguides does not occur properly, actually most of the light remains as the evanescent light between two waveguides, even for some values less than a specific thickness, light cannot propagate inside the waveguides. For thicknesses above 470nm, desired directional coupler satisfies the multimode condition.

Undesired changes in the cross-sectional geometry of the waveguides may occur during the microfabrication process; one of the cases which may occur is that the sidewalls of the waveguides may not be fabricated perfectly vertical. Hence, the effects of tilting in the waveguide sidewalls on the coupling length for 300nm and 200nm-separated directional couplers with the thickness of 300nm and top width of 300nm have been studied. Figure 4.7a shows the refractive index profile of the non-vertical sidewalls directional coupler from the cross-sectional view. Different cases for various sidewall angles have been numerically studied and the coupling lengths for both 200nm and 300nm-separated non-vertical sidewalls directional couplers calculated. Results are presented in Figs. 4.7b and 4.8a.

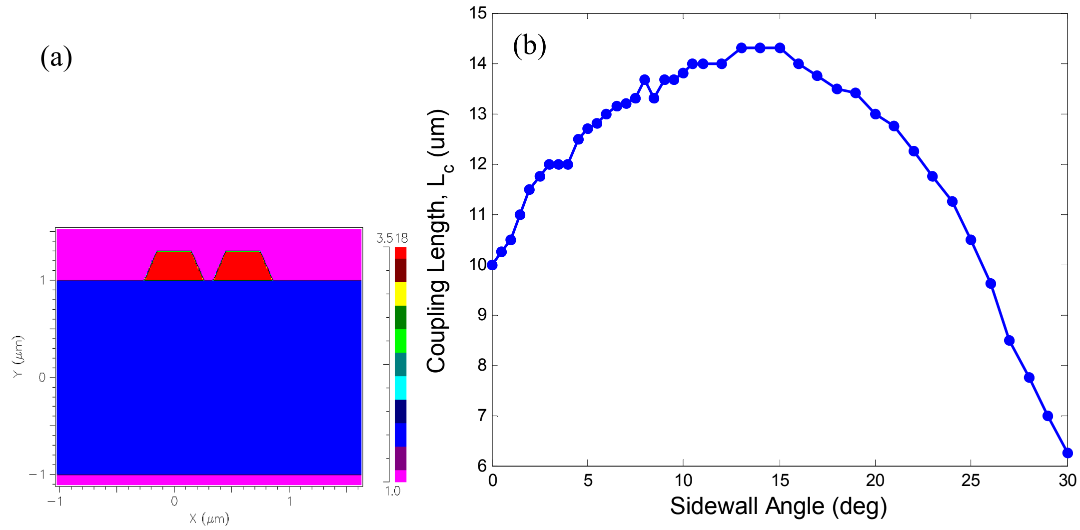

Figure 4.7: (a) Cross-sectional refractive index profile of directional coupler with non-vertical sidewalls, (b) Coupling Length, L_c, as a function of sidewall angle for a 300nm-separated non-vertical sidewalled directional coupler.

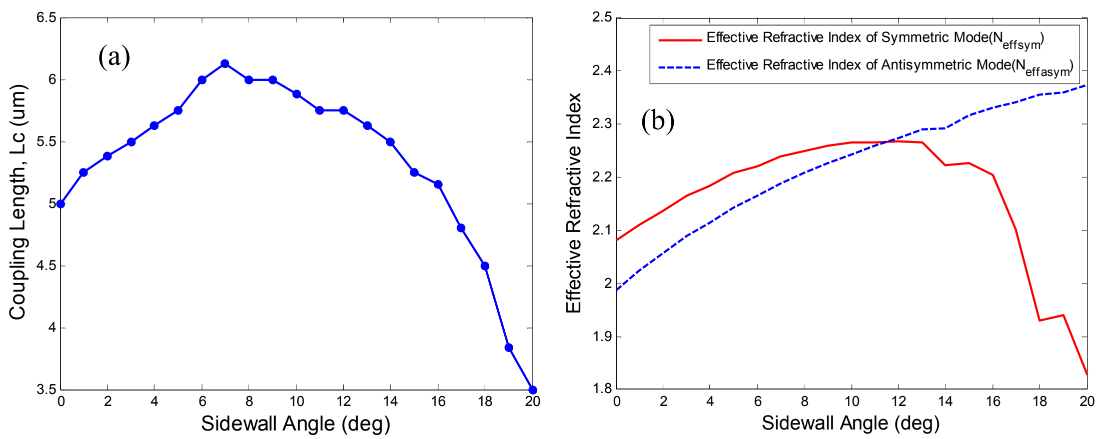

Figure 4.8: (a) Coupling Length as a function of sidewall angle for a 200nm-separated non-vertical sidewalled directional coupler, (b) Effective refractive indices for both symmetric and antisymmetric modes as a function of sidewall angle for a 200nm-separated non-vertical sidewalled directional coupler.

Simulations are conducted as well for 300nm-separated directional couplers with reversed non-vertical sidewalls. Figure 4.9a shows the cross-sectional view of the refractive index profile of the simulated device. Results show that the coupling length decreases as the angle of the walls increases. The coupling length corresponding to each angle is plotted in Fig. 4.9b. These results are in the path of the previous results of the non-vertical sidewalls. Figure 4.9c shows both results in a graph if we consider the reverse sidewalls angles as negative values.

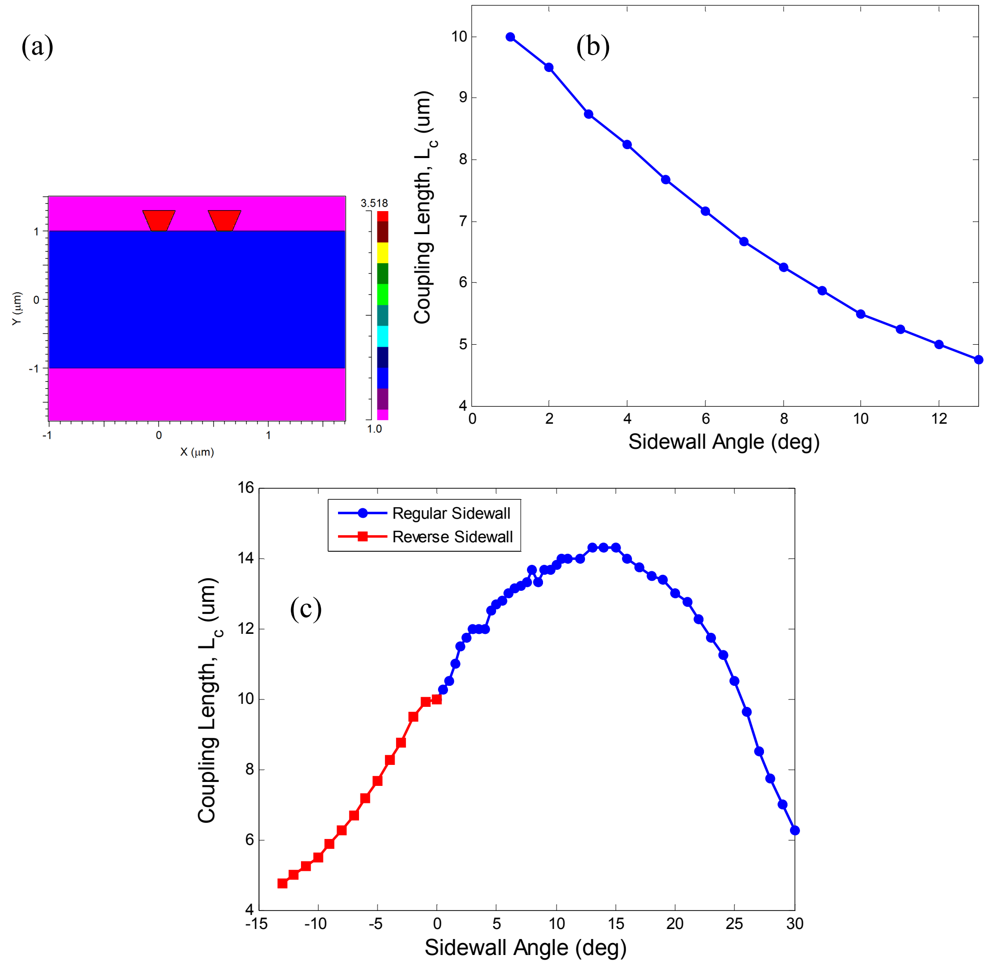

Figure 4.9: (a) Cross-sectional refractive index profile of non-vertical reverse sidewall directional coupler, (b) Coupling Length as a function of sidewall angles for a 300nm-separated reverse non-vertical sidewall directional coupler, (c) Coupling length for both non-vertical regular sidewalled and reverse non-vertical sidewalled of a 300nm-separated directional coupler.

Figure 4.10a shows another possible geometry that may be interesting to investigate in which each waveguide is consisted of two symmetric trapezoidal shaped parts, one on the top of the other. The coupling length dependency of the directional coupler on the sidewall angles is given in Fig. 4.10b. It is shown that for both cases where separations are 200nm and 300nm, the coupling length decreases as the sidewall angle increases, but in the case of 200nm separation, the reduction rate is less than coupling with a separation of 300nm which is less sensitive and more robust against fabrication imperfections.

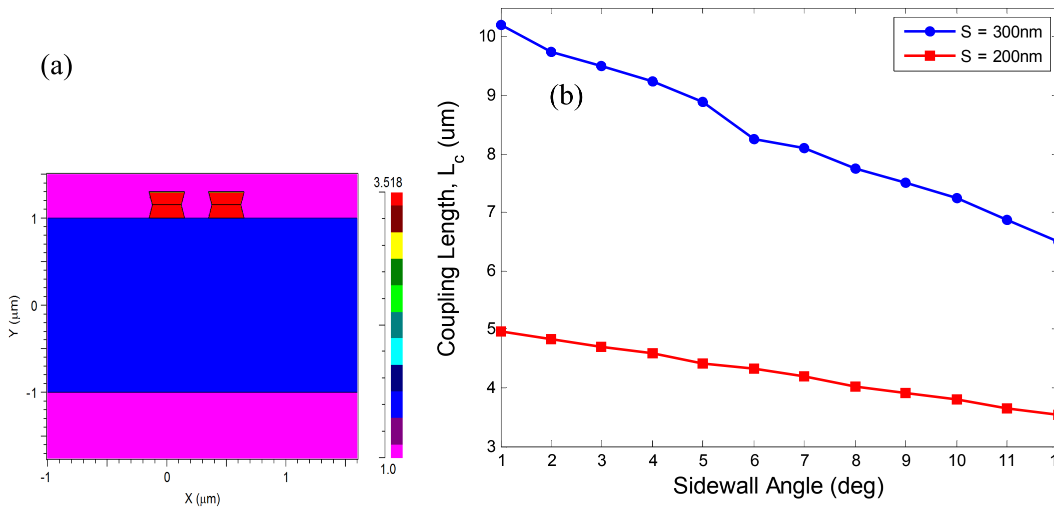

Figure 4.10: (a) Trapezoidal cross-sectional refractive index profile of non-vertical sidewalled directional coupler, (b) Coupling Length as a function of sidewall angles for 200nm and 300nm-separated non-vertical sidewalled directional coupler with trapezoidal cross-section.

4.3 Spectral analysis

Directional couplers can be used as wavelength selective devices in many nanophotonic applications and integrated circuits. In our simulations, we have observed a strong dependence of the device on the wavelength. To validate our results, first we have simulated a device reported in literature [20]. The device is a 100-µm-length Silicon-On-Insulator (SOI) 300nm-separated optical directional coupler with 300nm×300nm cross-sectional waveguides, and S-shaped waveguides as inputs and outputs. Our simulations were done using BPM method where the waveguides were assumed to be lossless. As it is shown in Fig. 4.11, the drops in the transmission for both parallel and cross ports are occurred in the same wavelengths. Also, these results show that the structure of the directional coupler is highly dependent on the operating wavelength such that small changes in the wavelength may cause several dB changes in transmission.

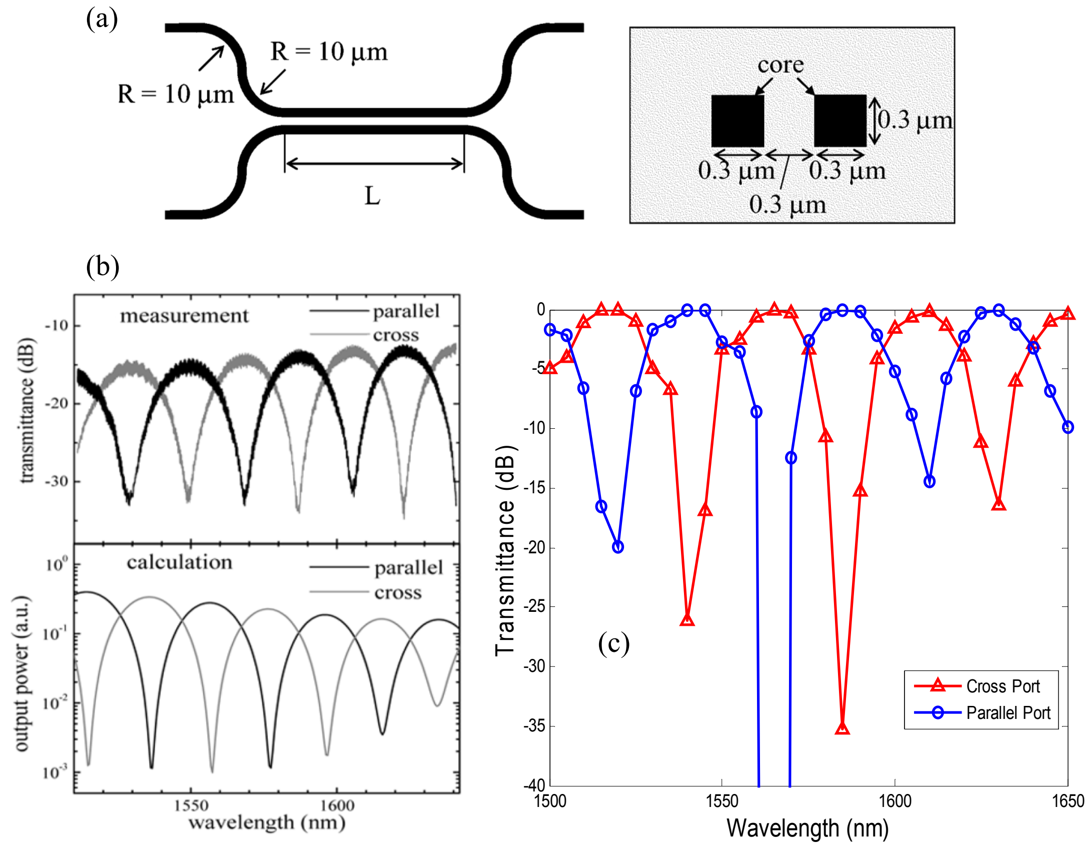

Figure 4.11: (a) Top and cross-sectional views of a Si-wire-waveguide directional coupler [20], (b) Measurement and calculation results of frequency response for a 100-μm-length 300nm-separated optical directional coupler with 300nm×300nm cross-sectional waveguides [20], (c) BPM simulation results of the same device assuming the waveguides are lossless.

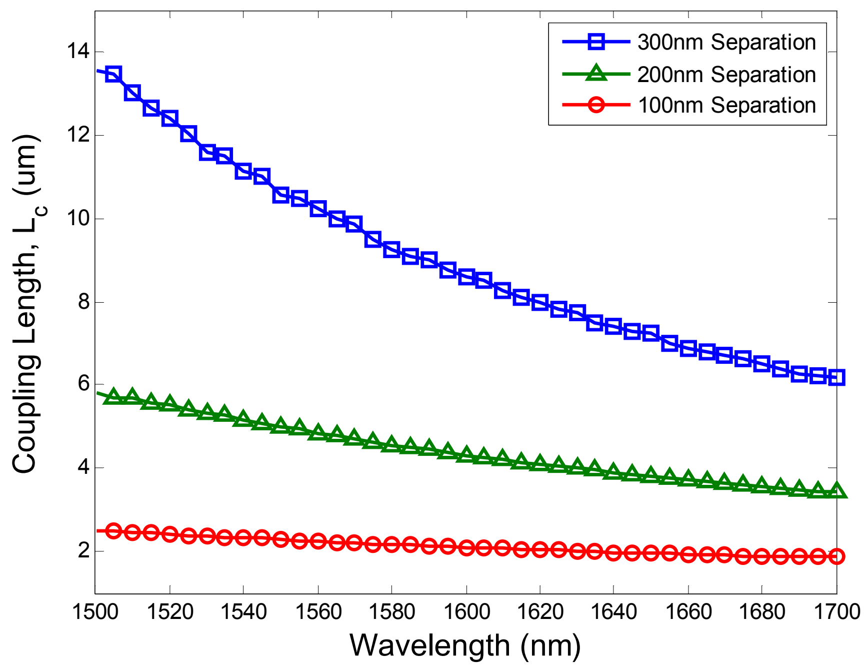

Figure 4.12: Wavelength dependency of coupling length for 100nm, 200nm and 300nm-separated directional couplers.

Using the same method, the coupling length of the directional coupler for different separation values has been calculated. The results in Fig. 4.12 show that the coupling length is dependent to wavelength, and it decreases generally as the wavelength increases. But as the separation decreases, the ratio of change in the coupling length decreases such that for 100nm separation the most robust coupling length dependency on wavelength is observed.

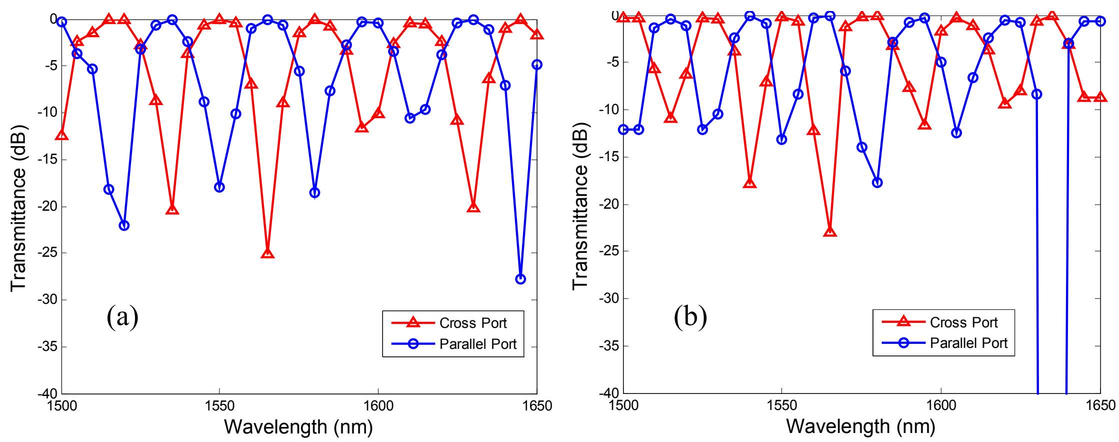

Figure 4.13: (a) Wavelength dependency of transmission for a 100μm-long 200nm-separated directional coupler, (b) Wavelength dependency of transmission for a 100μm-long 100nm-separated directional coupler.

Figure 4.13 shows the transmission of a 100μm-long directional coupler from both parallel and cross ports. The results show that although the coupling length of less separated device is less sensitive, the transmission is more sensitive to wavelength changes such that for less separated directional couplers the number of dropped wavelengths is more in a specific wavelength range comparing to those in larger separation distances.

Further investigations have been completed in order to characterize the frequency response of the directional couplers. Figure 4.14 shows the structure of the device simulated using an intensive FDTD method in order to obtain its wavelength dependency. The green plates show the input and output of the device where the electric field power is measured. The coupling region of two waveguides is called as the coupled-waveguide length which is selected to be 5 μm in order to decrease the simulation time as small as possible.

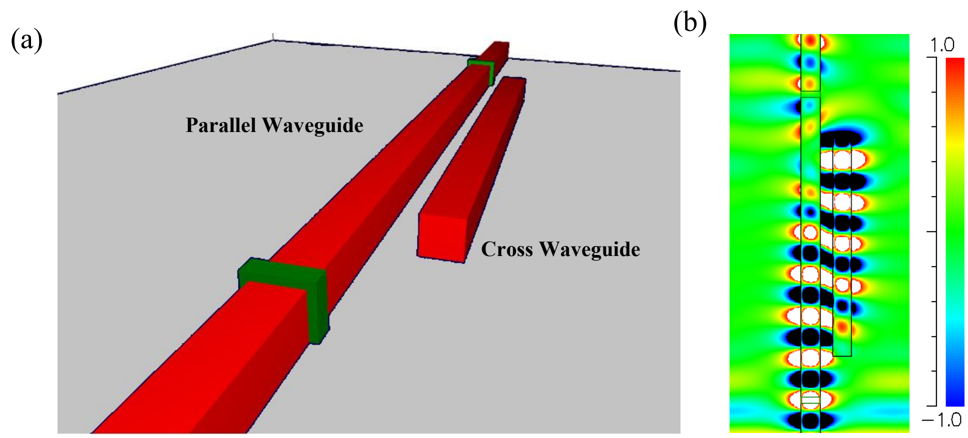

Figure 4.14: (a) 3D view of directional coupler placed on a SiO2 substrate, (b) E_x field distribution of TE-polarized light along a 5-µm-long 200nm-separated directional coupler.

The wavelength response of the device is plotted in Fig. 4.15 for different separation distances using Fast Fourier Transform (FFT) method with a Gaussian Transverse-Electric (TE)-polarized input light having a peak at the wavelength of 1.55 µm. Results show that the device is highly dependent on the wavelength and small changes in wavelength may cause significant change in transmission, suggesting the opportunity to use the structure as a wavelength selective device with a very high extinction ratio more than 30 dB at the dropped wavelengths.

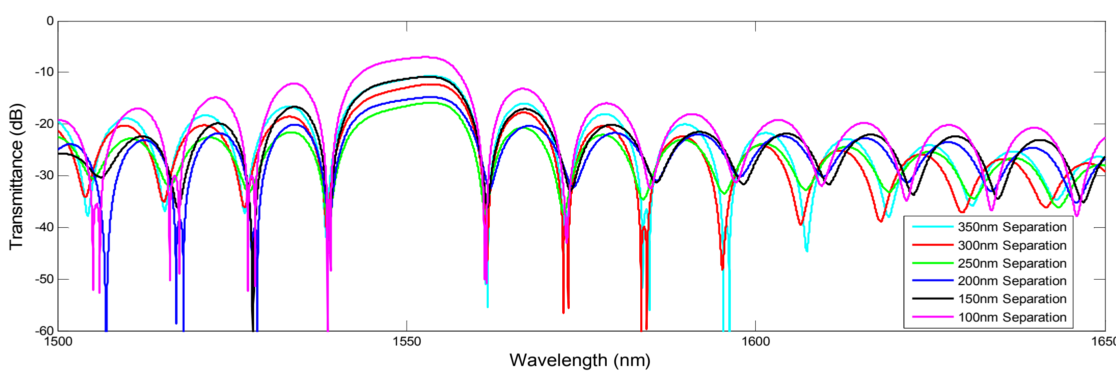

Figure 4.15: Wavelength dependency of a 5-µm-long directional coupler for different separations.

Wavelength response of a 300nm-separated directional coupler with the structure shown in Fig. 4.13a for different lengths has been simulated as well. Results are plotted in Fig. 4.16. Also corresponding results for 100nm-separated and 200nm-separated directional couplers are presented in Fig. 4.16.

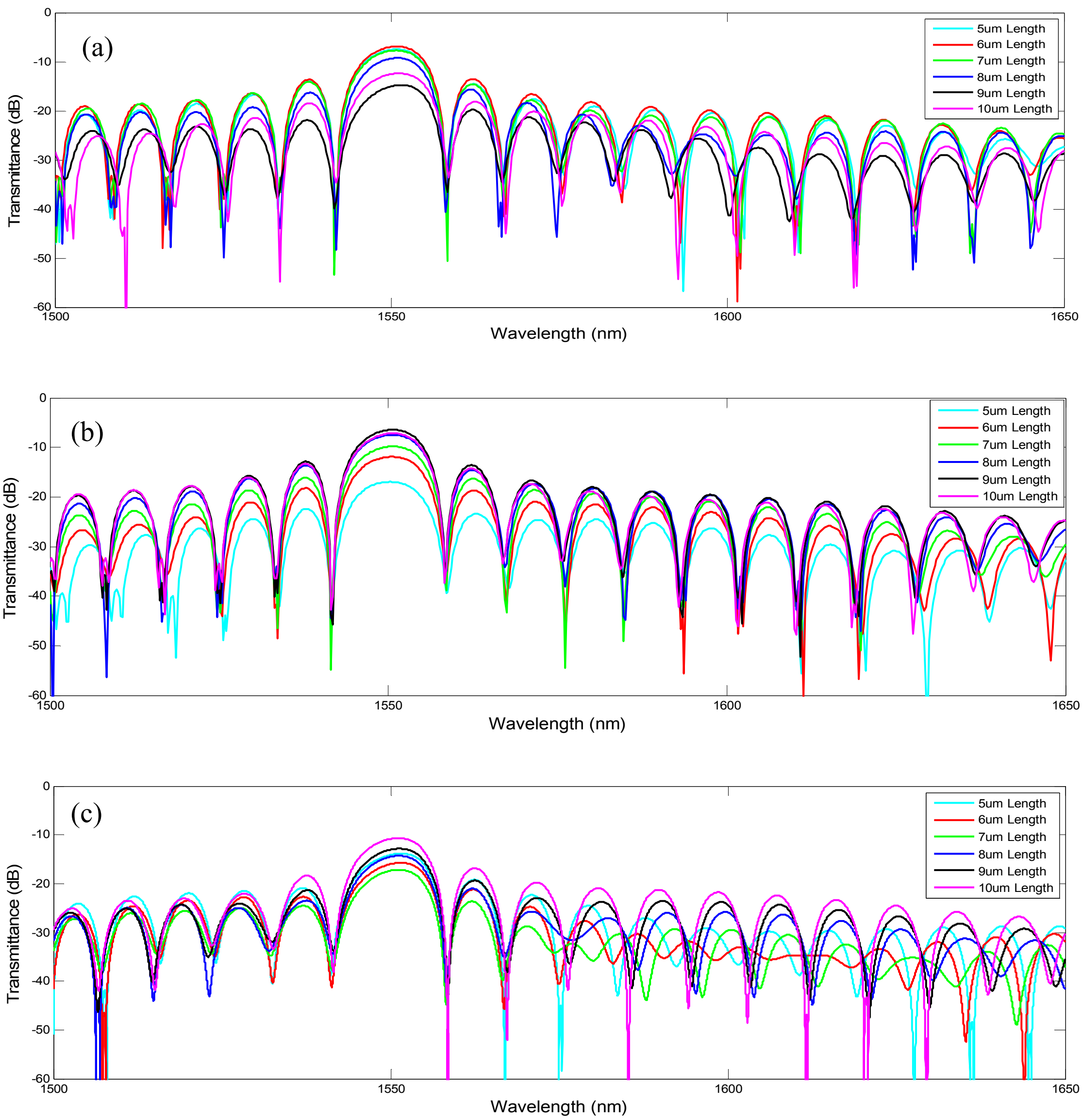

Figure 4.16: Wavelength response of (a) 100nm-separated, (b) 200nm-separated, (c) 300nm-separated directional coupler for different lengths.

4.4 Non-parallel optical directional coupler

Non-parallel optical directional couplers can be useful devices for power dividing or combining in a very small area in high density photonic circuits. These devices combine both power splitting and direction changing in one device while the ratio of splitting can be tuned easily by changing the device parameters.

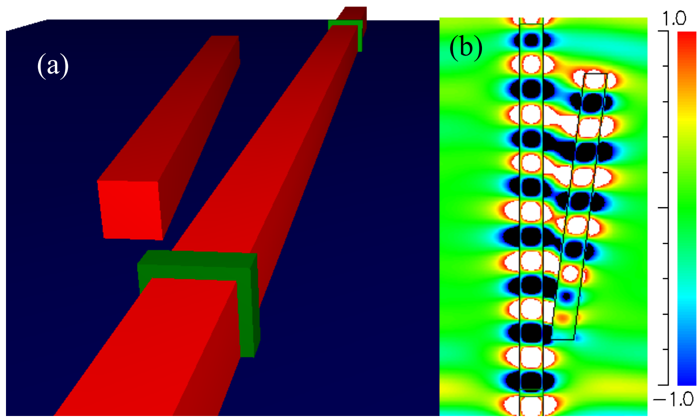

Figure 4.17: (a) 3D view of non-straight directional coupler placed on a SiO_2 substrate. (b) E_x field distribution of TE-polarized light along a 5-μm-long directional coupler with 5∘ tilted waveguide and 100nm initial.

Figure 4.17a shows the structure of a non-parallel directional coupler and the input and output ports of the simulated device. FDTD simulations of the device show that the output power depends on the initial separation of two waveguides and the ratio of their separation along the light field propagation which we refer as tilting angle. According to CMT we can write the powers along parallel and cross waveguides such that [26]:

$$P_{parallel} = P_{in}\cos^2[\theta(z)] \quad \textbf{(4.3)}$$

$$P_{cross} = P_{in}\sin^2[\theta(z)] \quad \textbf{(4.4)}$$

where $\theta(z) = \int_0^z \kappa(z')dz'$ and κ is the coupling coefficient and according to Eq. 2.9 can be expressed as $\kappa(z, s_0, \alpha) = Ke^{-\gamma(s_0+z\,tan(\alpha))}$, where γ is called decay constant.

The final coupling condition is determined by $\theta(\infty)$, for instance if $\theta(\infty) = \pi/2$ complete power transfer from waveguide I to waveguide II will occur, and for $\theta(\infty) = \pi/4$ it becomes a 3-dB directional coupler which half of the initial power is finally able to be transferred to the second waveguide.

Taking the integral gives us $\theta(z)$ as a function of all design parameters and the field power along the parallel port will be calculated:

$$\theta(z) = K \frac{e^{-\gamma s_0}}{\gamma \tan(\alpha)} \left[1 - e^{-\gamma z \tan(\alpha)}\right] \tag{4.5}$$

$$P_{parallel} = P_{in} \cos^2 \left[K \frac{e^{-\gamma s_0}}{\gamma \tan(\alpha)} \left(1 - e^{-\gamma z \tan(\alpha)}\right)\right] \tag{4.6}$$

Eq. 4.6 proves that the transmission of the non-straight directional coupler is just a function of initial separation and the angle between two waveguides.

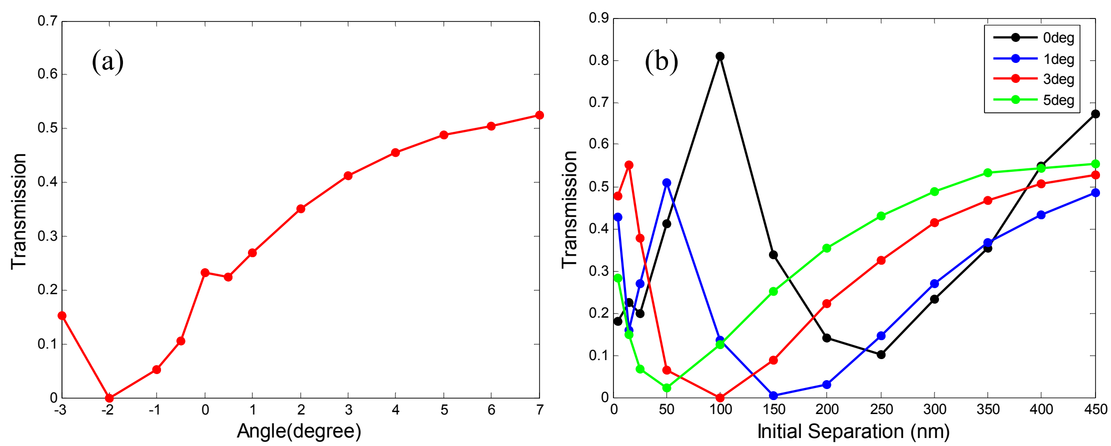

Figure 4.18: (a) Transmission dependence of a 5-µm-long directional coupler with tilted waveguide and 300nm initial separation on tilting angle. (b) Transmission dependence of a 5-µm-long directional coupler with different tilting angles and initial separations.

Figure 4.18a shows the transmission of a 5-µm-long non-straight directional coupler with 300nm initial separation for different tilting angles. The results show that as the angle increases the coupled light power to the tilted waveguide decreases which results in the raise in the transmission. The negative angles refer to the case where the waveguide is tilted in the opposite direction such that the waveguides gradually getting close to each other. The output power changes with respect to the initial separation distance between the waveguides. Figure 4.18b shows the transmission of the device at different initial separation distances for some tilting angle. At the small separation distances the coupling efficiency of the waveguides is greater, that causes the electric field power alternate more between the waveguides. While at the greater separation distances the coupled electric field at the tilted waveguide is not able to couple back because as the distance between the two waveguides increases along the coupler the coupling efficiency of the coupler decreases gradually.

5. DESIGN AND FABRICATION OF TESTING DEVICES

In order to characterize the proposed directional coupler, fabrication of several on a single wafer was decided. Figure 5.1a shows the structure of the entire list of devices on a single wafer. Several units of directional couplers are going to be fabricated each 400µm apart. Figure 5.1b shows one single block consisting of three different directional couplers. The fourth waveguide will be used as reference signal in order to compare its output light power with the corresponding outputs of the directional couplers. Six bending waveguides with the outer radius of 7µm to split the field power equally between the waveguides and decrease the bending loss as much as possible were deployed. Owing to fabrication limits enforced by electron beam lithography in terms of dimensions one can etch at one process, each straight waveguide is chosen to be 10µm long. Radius of splitters were also decided by the fabrication limits. At the output of each port, a 4-µm-outer radius bending waveguide is utilized to separate the output powers as far as possible. Hence the output powers reaching to the end of each waveguide will be observed with the help of a high sensitive camera from the top. Using straight output waveguides at the output may cause the powers to overlap. As seen in Fig. 16a each testing block is fed using a 2mm straight waveguide with 12 µm width and 340 nm height in order to couple the light to the waveguide from the lensed optical fiber with the highest coupling efficiency possible. Bending waveguides just before the testing blocks are also used to decrease the ambient noise caused by the optical fiber on the test devices. The outer radius of the bending waveguide is chosen to be 42 µm. The whole device is going to be fabricated twice on a single wafer, and at the end the wafer is going to be cleaved at the middle, leading to two identical for testing in order to ensure reliable results.

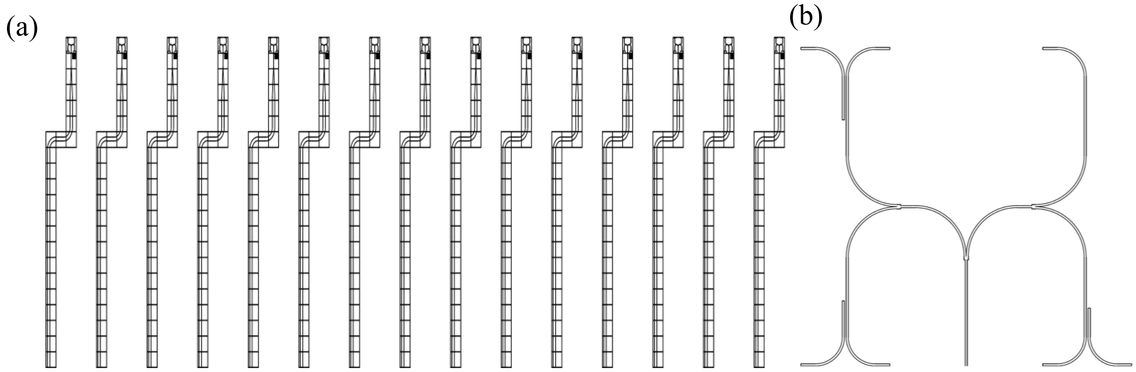

Figure 5.1: (a) Several units of directional couplers each 400 μm apart on a single wafer, (b) One single block of directional coupler consisting of three different directional couplers and a reference parallel-alone port.

5.1 Fabrication process

Optical Directional Couplers (ODCs) are fabricated utilizing Silicon-On-Insulator (SOI) technology. The largest dimension of device pattern takes place at the input light-coupling waveguides, 12 μm width, whereas, the critical dimension (minimum line spacing) occurs for the ODCs with 50 nm separation. In order to minimize writing time in electron beam lithography without compromising pattern quality at both extremes, consecutive two patterns are written using so-called mix-match process. The recipes of large and small pattern features utilized in the electron beam lithography processes are as given in Table 5.1.

Table 5.1: Electron beam lithography parameters.

Electron Beam Resist Patterning Recipe			
Positive resist (PMMA)	Prebake	180 ºC	2 min
	Spin coat	500 rpm	10 sec
		8000 rpm	1 min
	Postbake	180 ºC	2 min
	Resist Thickness	50 nm	
Patterning Small Features	Acceleration Voltage	30 kV	
	Beam Current	48 pA	
	Step Size along X, Y	5 nm	
	Exposure Density	180 μC/cm2	
	Write Field Size	50μm × 50μm	
Patterning Large Features	Acceleration Voltage	10 kV	
	Beam Current	1.6 nA	
	Step Size along X, Y	500 nm	
	Exposure Density	150 μC/cm2	
	Write Field Size	1000μm × 1000μm	
Development	Developing by 1:3 MIBK:IPA	25 ºC	50 sec
	Rinsing by IPA	25 ºC	20 sec
	Postbake	100 ºC	1 min

The ODCs are fabricated on an SOI wafer with 340nm-thick device silicon and 1 m-thick buried-oxide layer. Process plan is as illustrated in Fig. 5.2.

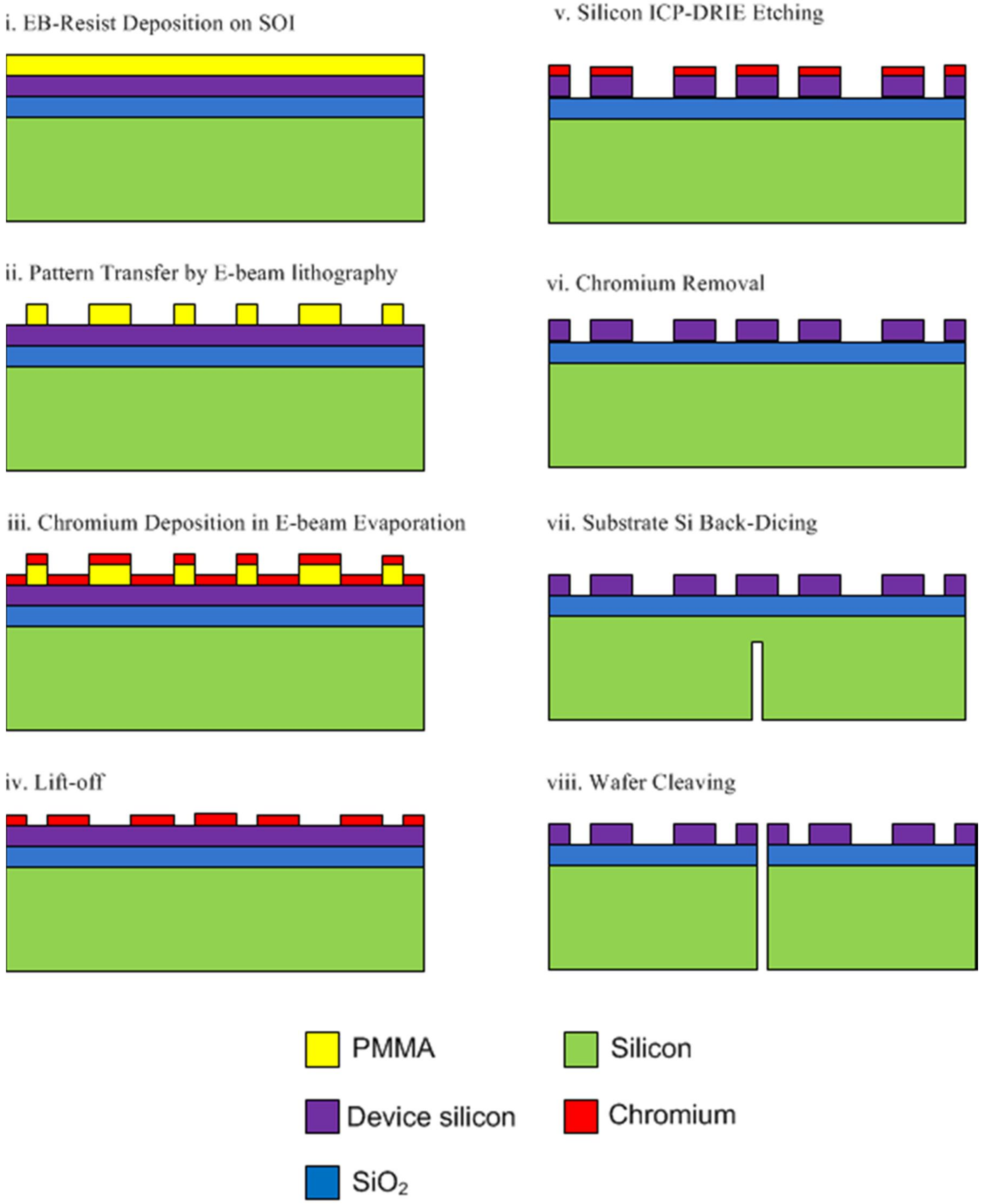

Figure 5.2: Fabrication process.

First, desired geometries are patterned using electron beam lithography (FEI Nova NanoSEM 600 with integrated Raith ElphyPlus, FEI&Raith Co., USA). A positive electron beam resist (PMMA 950K, Microchem Co., USA) is spin coated. Using electron beam lithography small and large features of the device pattern is written on the PMMA layer. Then, device is coated with chromium by electron beam evaporation process (PVD Vapor 4S E-Beam, Vaksis Co., Turkey) and remaining PMMA resist is lifted off via organic cleaning. Parameters utilized in the evaporation steps are as presented in Table 5.2.

Table 5.2: Electron beam evaporation parameters.

Chromium Deposition for Lift-off		
Preparation	Chamber Vacuum	4×10-6 Torr
	Chromium Density	7.19 g.cm-3
	K Factor	100
	Ionization Energy	2987 kJ.mol-1
	Temperature	20 ºC
Deposition	Voltage	25 kV
	Current Beam	25 mA
	Rate	0.03 nm/s
	Thickness	30 nm
Drying	Dry N2 Gas	1 min

Afterward, the remaining PMMA is removed. Then, device silicon layer is dry etched by inductively coupled plasma (LPX SR-Cl, STS Co.) using SF_6 and O_2 as etch and passivation gasses, respectively. Chromium is utilized as hard mask due to its high selectivity with respect to silicon. Table 5.3 lists the parameters utilized in the Inductively-Coupled-Plasma Deep-Reactive-Ion-Etching (ICP-DRIE) process. 300nm-thick device silicon is etched at approximately 65.45 nm/min rate.

Table 5.3: Inductively-Coupled-Plasma Deep-Reactive-Ion-Etching (ICP-DRIE) parameters.

Silicon DRIE Recipes		
Recipe	I	II
Number of Cycles	25	
Passivation Time	6 sec	
Etch Time	5 sec	
Chamber Vacuum	8×10-3 Torr	10×10-3 Torr
SF6/O2 Flow Rates	20/50 sccm	
RF Platen Power @ Etch/Passivation	600/20 W	300/10 W
RF Generator Power @ Etch/Passivation		

In order to find the best fabrication parameters in the electron beam lithography process, several recipes are tried. Figure 5.3 shows different patterns written on the PMMA layer with different electron beam current densities. As results show, as the density of electron beam current increases, waveguides' quality in terms of PMMA concentration and sharper edges also increases. We have experimentally observed that incrementation of electron beam current density to more than the value of 180μC/cm^2 will not change the quality of fabrication, but will increase the exposure time, unnecessarily. Hence, we stuck to this value for the future fabrications.

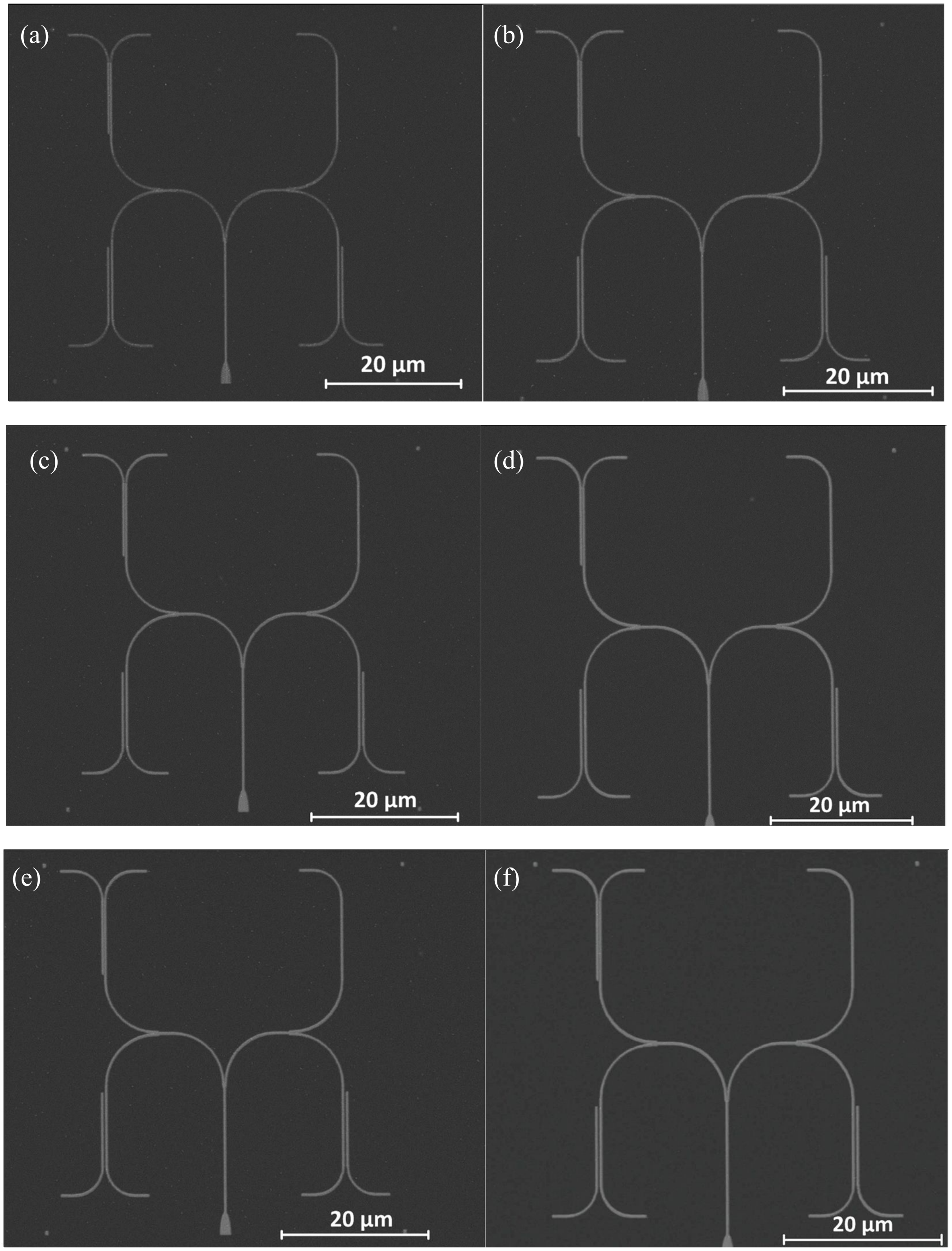

Figure 5.3: Fabricated structures for (a)144 μC/cm^2, (b)156 μC/cm^2, (c)168 μC/cm^2, (d) 175 μC/cm^2, (e)180 μC/cm^2 and (f)185 μC/cm^2 electron beam current density.

Several ODCs with different coupled waveguide lengths and separations are patterned on the same SOI wafer using the learned recipe. Figure 5.4 shows the SEM micrographs of different structures.

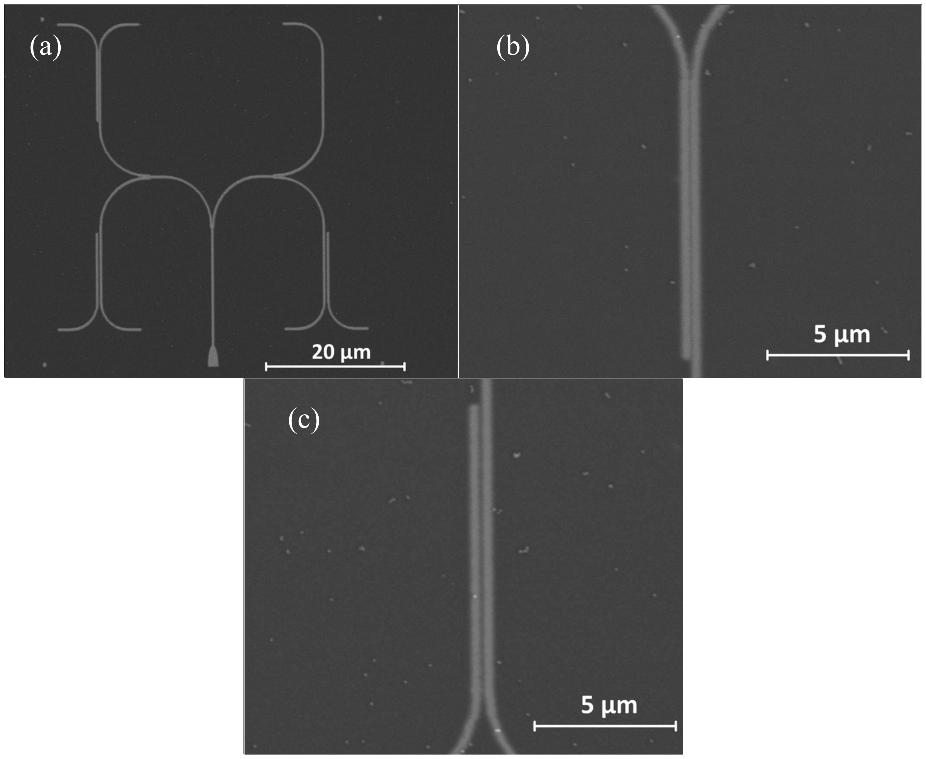

Figure 5.4: SEM micrograph of structures after electron beam lithography process. (a) Set of ODCs of 10 m-long coupled waveguides, (b) 50nm-separated ODC and (c) 150nm-separated ODC.

Figure 5.4a shows a set of ODCs of 10 m-long coupled waveguides with 50nm, 270nm and 280nm separation distances as shown on upper-left, lower-left and lower-right of the SEM micrograph, respectively. The upper-right waveguide is the reference waveguide to be used as normalization reference output. Figure 5.4b shows a closer picture of the 50nm-separated ODC already shown in Fig. 4a. Our observations under the SEM machine show that the separation is about 53nm which is in good agreement with 50 nm desired separation. Figure 5.4c also illustrates ODC with 150nm separation, which after fabrication is observed to be about 148nm. The waveguide width in all micrographs is designed to be 300nm. We observed at most 5% mismatch with the desired width for different fabricated ODCs.

After transferring the desired patterns on PMMA resist layer in electron beam lithography, the entire structure is coated with chromium in electron beam evaporation process and the remaining PMMA resist is removed. Figure 5.5 shows the structures when metalized with chromium.

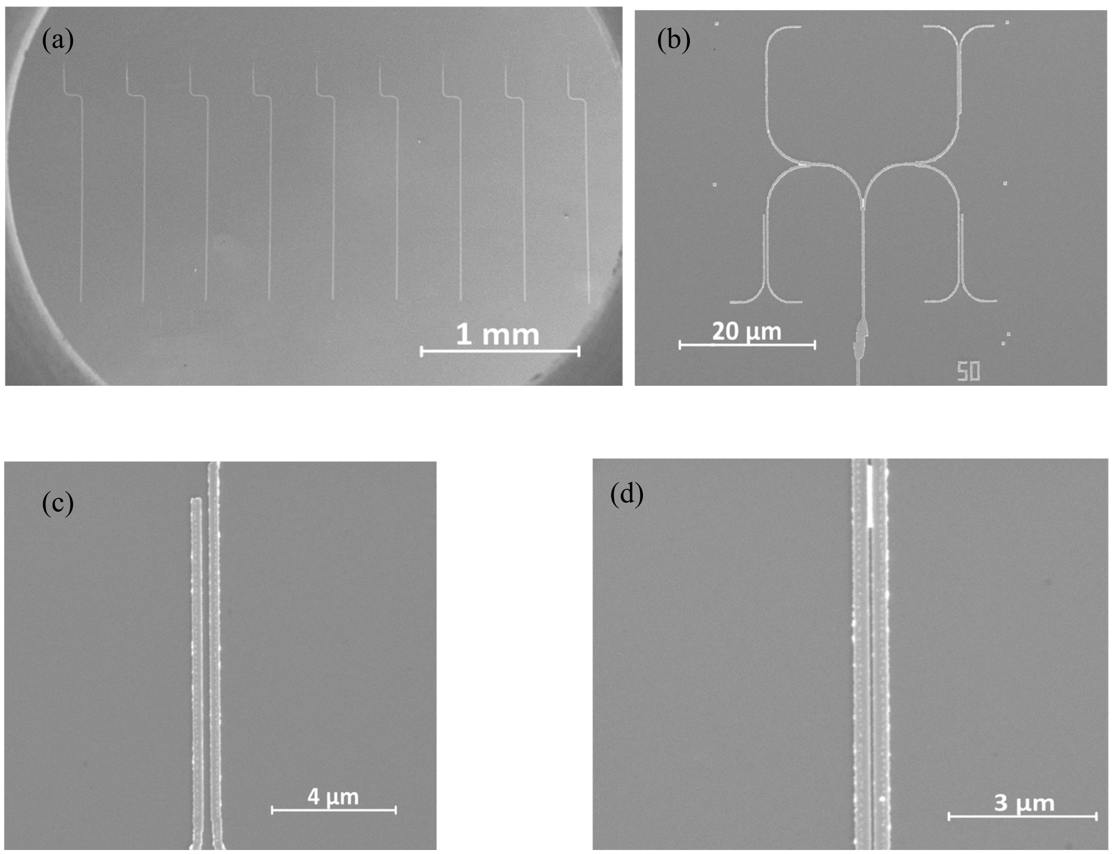

Figure 5.5: SEM micrograph of structures after chromium deposition. (a) fabricated structures on one SOI wafer, (b) set of ODCs with 10 m-long coupled waveguides, (c) 280nm-separated ODC and (d) 100nm-separated ODC.

5.2 Geometry measurements

In order to measure the dimensions of the devices we can use methods like SEM, Atomic Force Microscopy (AFM) or optical microscopy. AFM usually gives higher resolution and more accurate values, but SEM and optical microscopy are limited by the image resolution and many other parameters. Our devices are such that SEM micrographs give accurate enough results. One of the problems with AFM is due to its mechanical contact measurement system which may move the movable parts of the MEMS devices. Hence, using AFM may not help in all of the cases. Optical microscopy is the other possible method for us to measure the dimensions. In this particular method we can use optical and digital zoom in the images and compare the specific dimensions with the longer reference structures which we fabricate on the wafer.

After fabrication, the geometry including width, length and separation distance of waveguide pairs in each ODC is measured under SEM. This measurement is accomplished after each step of fabrication process. Figure 5.6 depicts typical devices with the measured parameters.

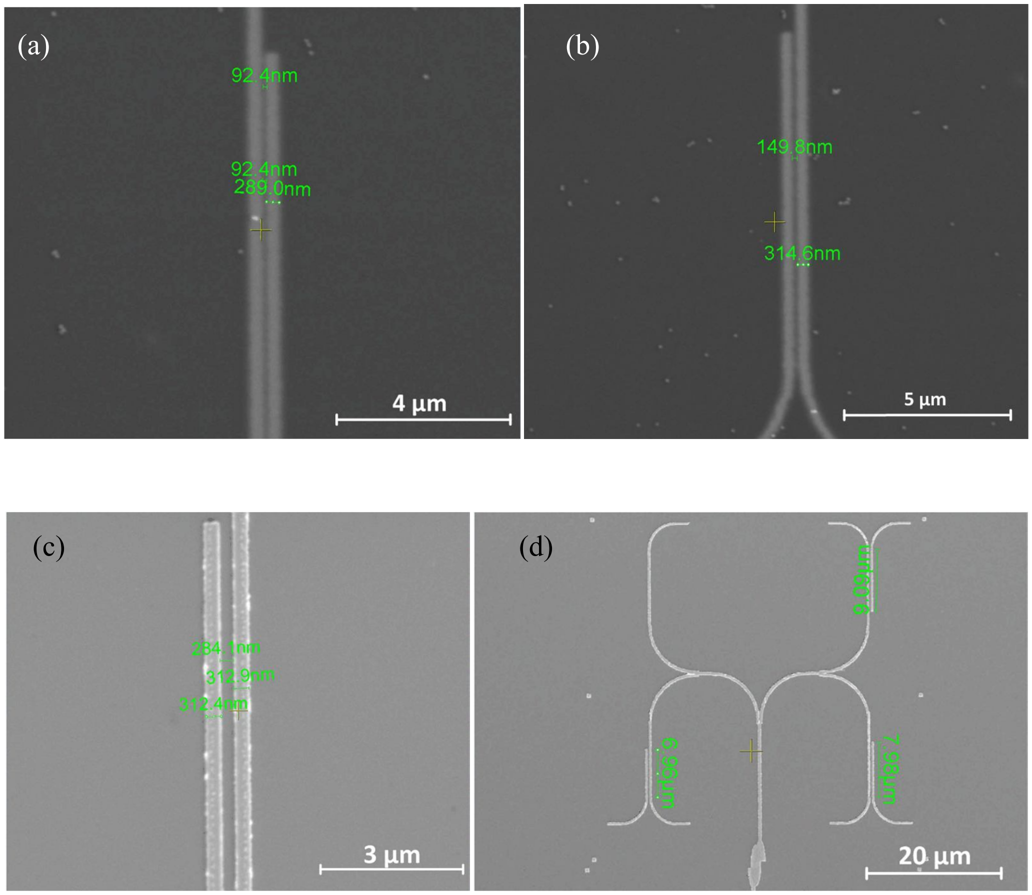

Figure 5.6: SEM images of (a) 150nm-separated ODC after electron beam lithography, (b) 100nm-separated ODC after electron beam lithography, (c) 300nm-separated ODC after chromium coating and (d) set of ODCs with different length of coupled waveguides.

Figure 5.6 illustrates the SEM images with the results obtained from the image processing tool for 100nm, 150nm, 300nm-separated ODCs with various lengths. Results show some slight differences with respect to the desired values, which we think are caused by image resolution, inaccuracy in electron beam lithography, scattering of electron beam in PMMA layer (proximity effect) and other parameter variation encountered during fabrication process as usual.

5.3 Fabricated devices

Both previous simulation and fabrication studies were accomplished for a device silicon layer thickness of 300nm of the SOI wafer. However, since the SOI wafers we have at hand are those with 340nm, in this section we repeated the simulation studies quickly based on our established experience except the Inductively Coupled Plasma Deep Reactive Ion Etching (ICP-DRIE) etch depth has changed from 300nm to 340nm.

Figure 5.7a shows the fabricated devices for a set of 200nm_separated ODCs. A closer SEM picture is demonstrated in Fig. 5.7b and 5.7c for devices with 100nm separations.

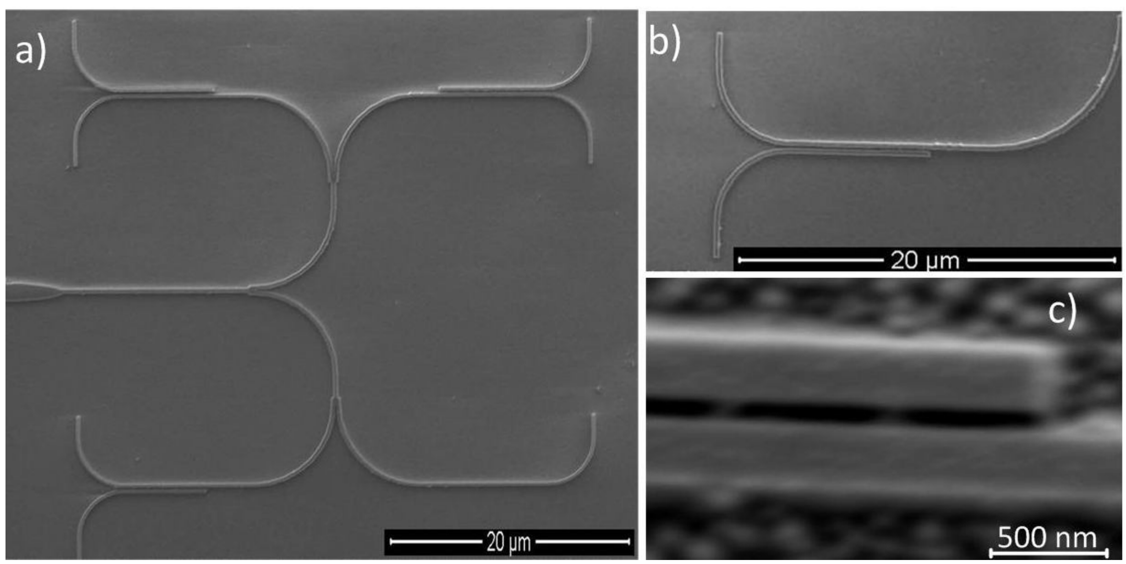

Figure 5.7: (a) A set of fabricated ODC devices fed by a single input waveguide, (b) 7.6 m-length 100nm-separated ODC, (c) Close SEM Image of a 100nm-separated ODC.

6. EXPERIMENTAL CHARACTERIZATION

Similar to that in section 4, the coupling length of the ODCs with 300nm×340nm (width×thickness) cross-section is recalculated for various separation distances in 1550nm optical wavelength. Figure 6.1 shows the calculation points by Beam Propagation Method (BPM) and their fitted curve to coupling length values for a range of separations. The results show an exponential behavior of the coupling length with respect to separation of two waveguides as always. Hence, the parameters of the exponential curve which already reported in the First Progress Report are updated. Updated results yielded the relation as

$$L_c[s(nm)] = 1.328\, e^{0.00733s}\ (\mu m) \qquad \textbf{(6.1)}$$

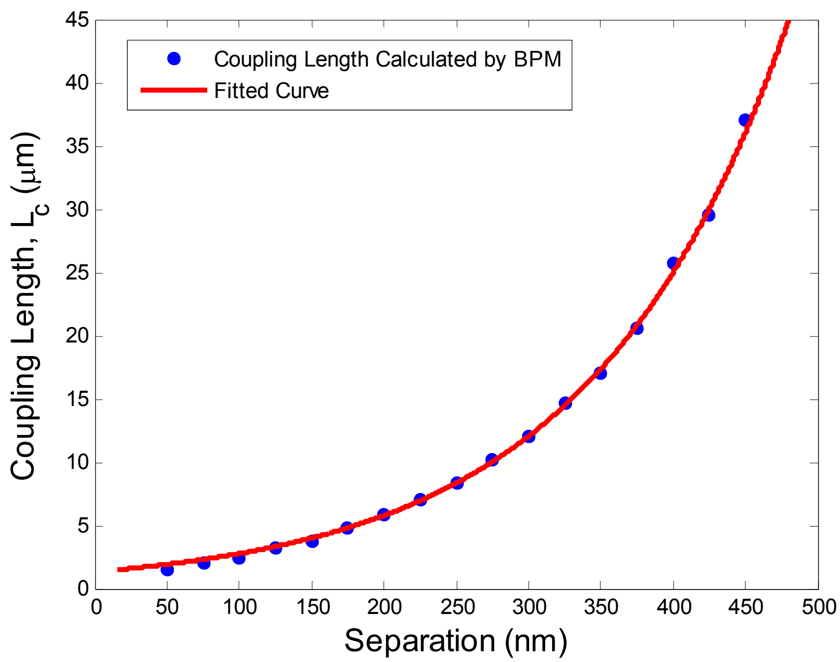

Figure 6.1: Coupling length of the directional coupler as a function of the separation between the waveguides, and its fitted curve.

In order to test the fabricated devices experimentally, the characterization setup shown in Fig. 6.2 is used. A Tunable Laser Source (TLS) output is internally controlled by a Polarization Controller (PC) and then fed into the Device Under Test (DUT). The output is then collected using NIR lens objectives into an InGaAs NIR camera as the Photo Detector (PD) device which is connected to a PC for light intensity calculations using an image processing software developed in-house.

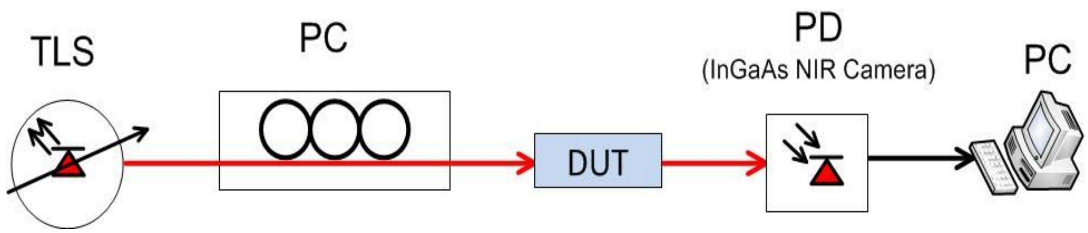

Figure 6.2: Optical setup used to characterize the fabricated devices.

First Devices are tested at the optical wavelength of 1550nm. For instance, Fig. 6.3 illustrates the optical output power detected with the NIR camera for six different ODCs. Figure 6.3a shows how the optical output power of the parallel ports for ODC devices with 100nm separation distances ranging from 9.2 m to 10 m lengths change from 57% to about 90%. Figure 6.3b is related to the ODCs with 300nm separation and lengths of 1, 2 and 3 m. The output power changes from 70% to about 100% at the parallel port. Figure 6.3c illustrates the optical output intensity of parallel port of 250nm-separated ODCs with lengths of 4, 5 and 6 m which show a decrease in transmission from 54% down to 15%.The output power for each port of a single ODC is normalized to the sum of both the parallel and cross ports. Figure 4d shows a set of 10 m-long ODCs with 100,150 and 200nm separations which show 89%, 34% and 89% transmission at parallel port, respectively.

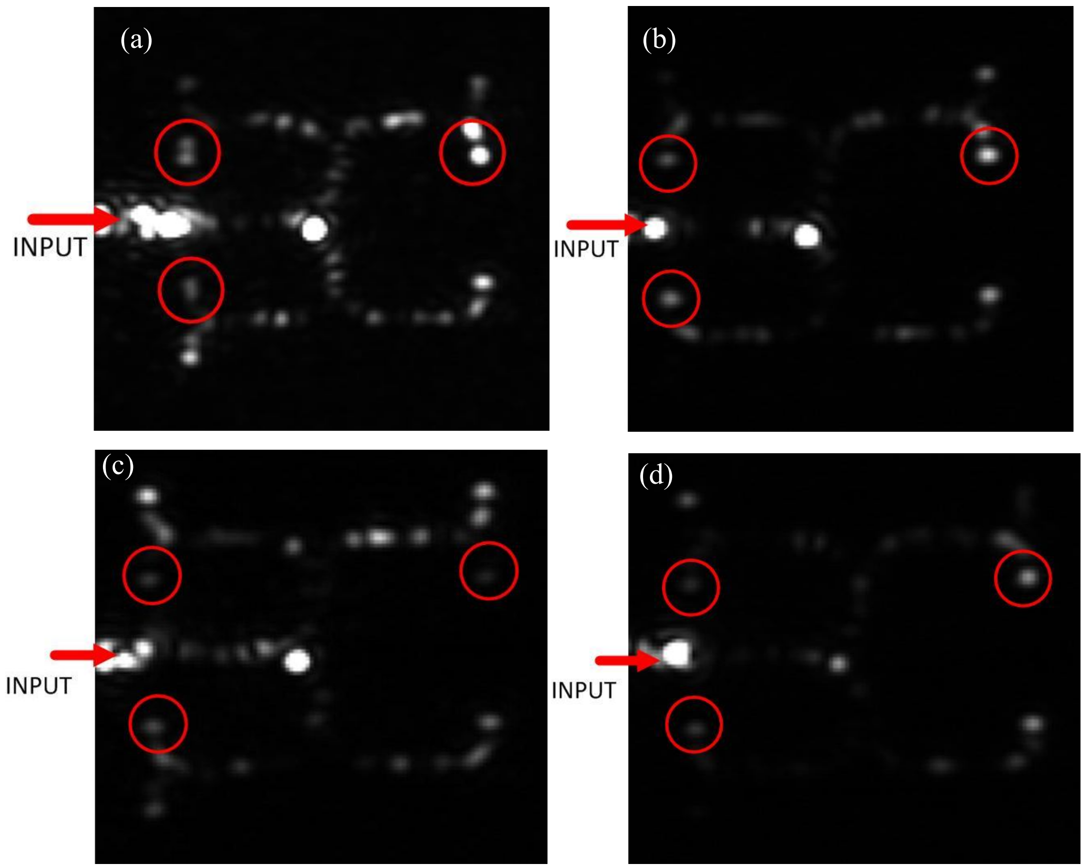

Figure 6.3: Images taken from the NIR camera show the output light intensities from the ODC ports at the wavelength of 1550nm (red circles show the output light of parallel port). (a) 100nm-separated ODCs with 9.2, 9.6 and 10 m lengths, (b) 300nm-separated ODCs with 1, 2 and 3 m lengths, (c) 250nm-separated ODCs with 4, 5 and 6 m lengths, and (d) 10 m-long ODCs with 100, 150 and 200nm separations. (Lengths or separations of ODCs increases from bottom left to top left and then top right of each NIR image)

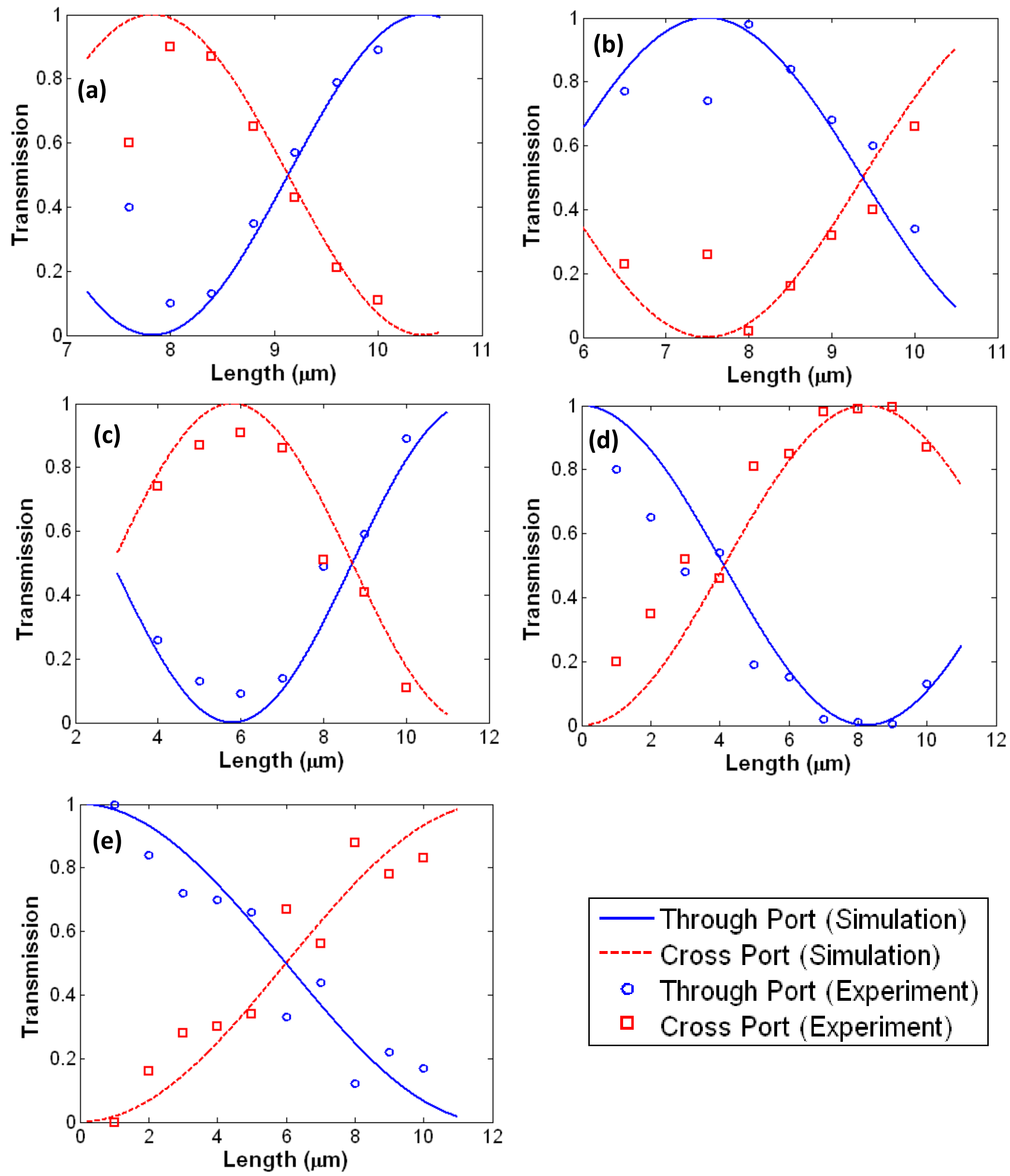

Figure 6.4: Transmission of ODCs as a function of coupled-waveguides length at 1550nm wavelength with (a) 100nm, (b) 150nm, (c) 200nm, (d) 250nm, and (e) 300nm separations.

All of the fabricated devices are optically tested. Figure 6.4 depicts the measured and calculated transmissions at 1550nm wavelength for both through and cross ports of devices with various length and separation values. Experimental results show good agreement with the theoretical ones. Slight deviations between theoretical and experimental results are caused due to the imperfections in fabrication mainly owing to the surface roughness of the waveguide sidewalls, and also the errors in the measurement system due to optical noise. The measured powers at the outputs change sinusoidally with respect to the length of the coupler. The fact that smaller separations have relatively smaller coupling lengths learned from simulations is also confirmed by the experiment.

The experimental and calculated power transmissions of 8 m and 10 m-long ODCs as a function of separation distance at 1550nm wavelength from both through and cross ports are illustrated in Fig. 6.5. A strong dependence of transmission on separation distance is obtained such that ODCs with smaller separations and longer lengths are more dependent on separation changes. Hence, ODCs with small separations can be utilized in applications requiring higher sensitivities and fast responses to the motion at short range displacements such as fast optical switches and high-sensitivity embedded motion detectors.

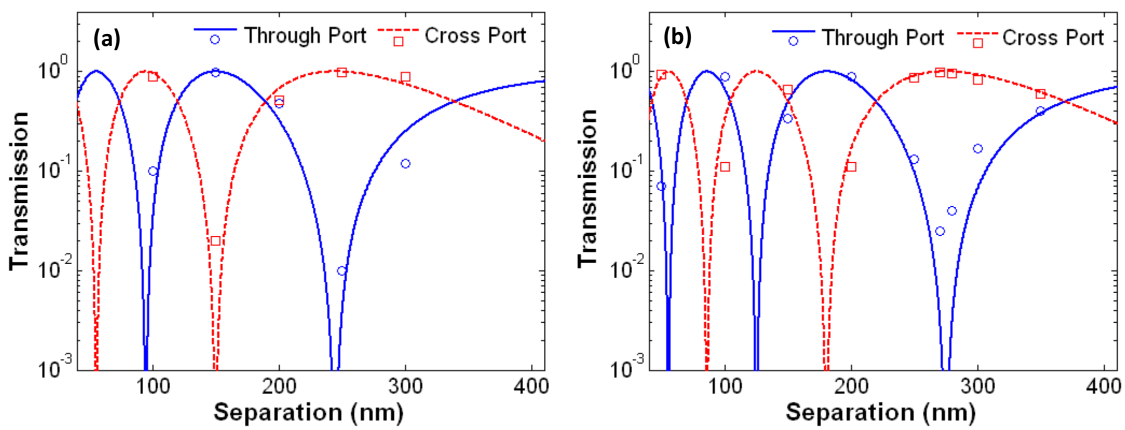

Figure 6.5: Transmission as a function of separation distance at 1550nm wavelength for ODCs with a length of (a) 8 m, and (b) 10 m in logarithmic scale. (Circle and square markers depict the experimental results, solid and dashed lines illustrate the calculated theoretical results for both through and cross ports, respectively.)

6.2 Spectral Analysis

The simulation results for a waveguide cross-sectional geometry of 300nm×340nm (width×thickness) are realized. The results are presented in Fig. 6.6 which shows the changes of coupling length within the wavelength range from 1470nm to 1700nm for ODC devices with varying separations. The results show that the coupling length is dependent to wavelength, and it decreases generally as the wavelength increases. But as the separation decreases, the ratio of change in the coupling length decreases such that for 100nm separation the most robust coupling length dependency on wavelength is observed.

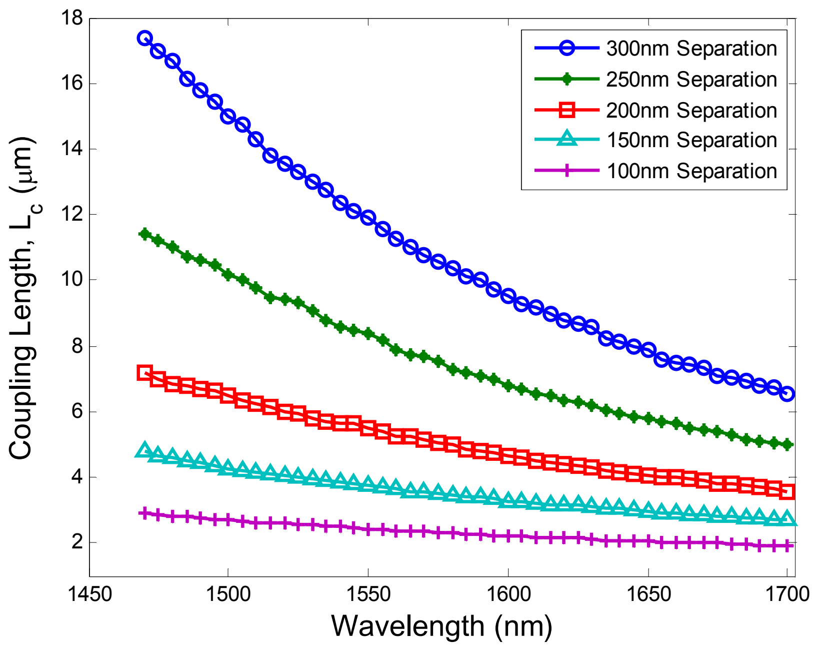

Figure 6.6: Simulated wavelength dependency of the Coupling Length, Lc, for ODCs in the range from 100nm to 300 nm separation.

Figure 6.7 depicts the transmission spectrum of the cross port of the ODCs based on theoretical and experimental results for various waveguide separations and lengths. Figure 10 relates to the transmission spectrum of a 10 m-length ODC when the separation of waveguides changes from 150nm to 300nm. Since deviations in separation distances or length of the ODCs can change the characteristics of the transmission spectrum, one can use this fact in order to measure any displacement. Experimental results prove the validity of theoretical calculations with an acceptable deviation.

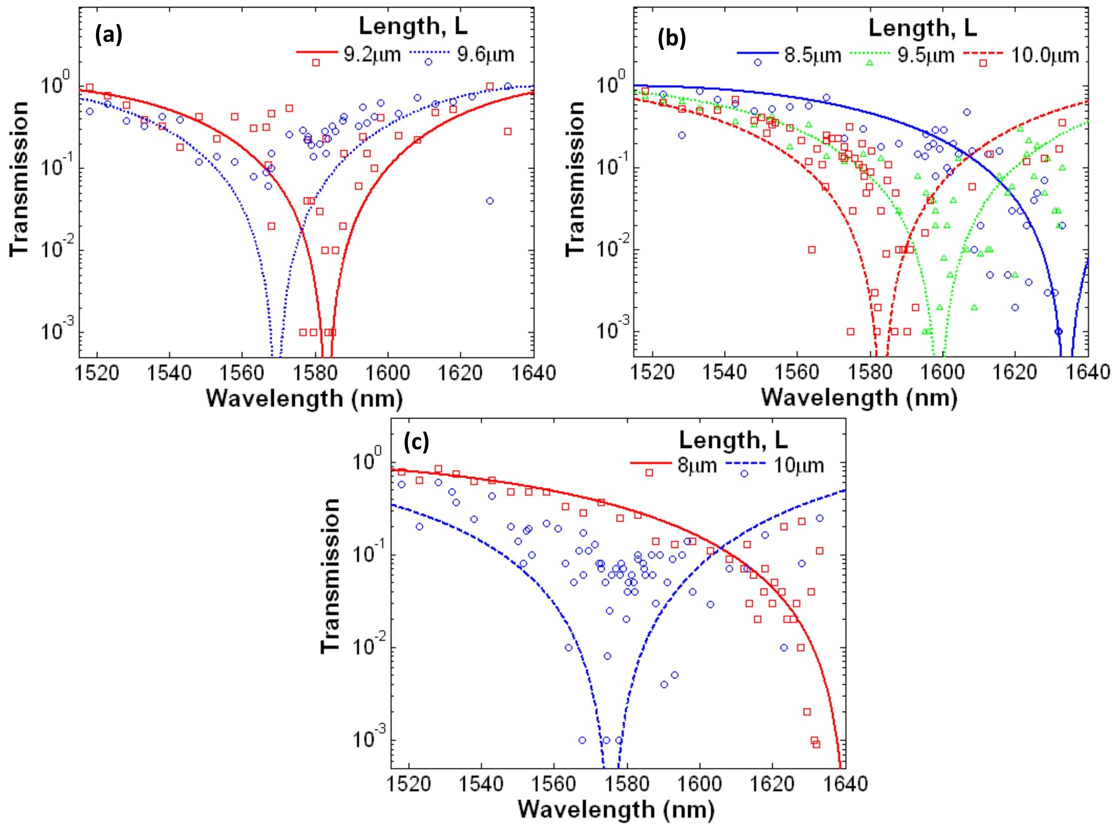

Figure 6.7: Transmission spectra in logarithmic scale at (a) Cross port of 100nm separated, (b) Through port of 150nm-separated, and (c) Cross port of 200nm-separated ODCs. (Discrete markers show the experimental results, and lines show the calculated theoretical ones.)

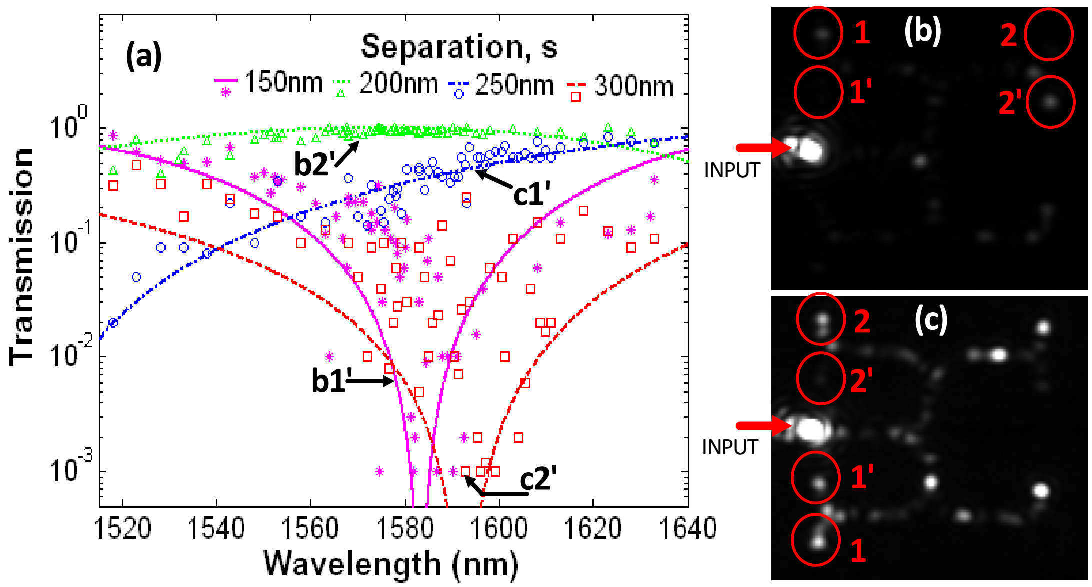

Figure 6.8: Transmission spectra in logarithmic scale from through port of 10 m-long ODC. (Discrete markers show the experimental results, and lines show the calculated theoretical ones), and NIR micrographs illustrating optical powers out of 10 m-long ODCs' ports (b) at 1578nm wavelength for 1) 150nm, and 2) 200nm separations, and (c) at 1587nm wavelength for 1) 250nm, and 2) 300nm separations. (Numbers with and without primes correspond to through and cross ports, respectively.)

The transmission spectra from the through port of 10 m-long ODCs at particular separations are depicted in Fig. 6.8a. The experimental results show good agreement with the theoretical ones. Results show a high dependency on wavelength for all separation distances. Figure 6.8b, for instance, indicates the NIR micrograph of 10 m-long ODCs at the wavelength of 1578nm for through and cross ports at 150nm and 200nm separations marked as 1' and 2, respectively. As presented in Fig. 6.8b, the output light at through port of a 10 m-long 150nm-separated ODC at 1578nm wavelength is almost zero, and a similar situation occurs at the cross port of the 10 m-long 200nm-separated ODC. Figure 6.8c, on the other hand, shows the output light at the wavelength of 1587nm. The output is completely transferred to the cross port of a 10 m-long 300nm-separated ODC marked as 2, while for the same length of ODC with 250nm separation around 60% of light is splitted into the cross port. Although, short ODCs show less channel dropping characteristics when compared to the longer ones, they still can be used and optimized as power splitters or tunable wide-FSR channel dropping filters as more robust devices to fabrication imperfections. On the other hand, long ODCs are simple and easy to fabricate for implementing wavelength transmission filters, switches and high-sensitivity sensors.

7. SENSOR DESIGN

Based on the simulations and experimental results obtained so far, different strategies are considered in order to measure the mechanical displacement produced by actuation in real time to measure the motions in high or low range distances with high and low sensitivities. Here, in order to generate motion in the system, electrostatic forces generated by a micro-comb actuator are utilized. Figure 7.1 shows three possible different structures where ODCs could be used as motion sensors. Figure 7.1a shows a simple ODC in which one of the waveguides is brought to the proximity of the other waveguide by means of a micro-actuator. Previous results well showed that changes in the separation of the waveguides in nanometer scale can cause a significant change in the output optical power. Hence, this phenomenon can be used to detect motions in systems which require higher sensitivities but smaller displacements. An example is as given Fig. 7.1b showing how two ODCs are cascaded in a single device.

In order to have higher range displacement sensors, one can take advantage of power change along the ODCs. Figure 7.1c shows how two ODCs are cascaded and integrated with the micro-comb actuator in order to characterize the performance of the sensor. To obtain high sensitivity devices to motion, one can use smaller separations as the results shown verify that for smaller separations period of sinusoidal curve relating the transmission to coupling length gets smaller.

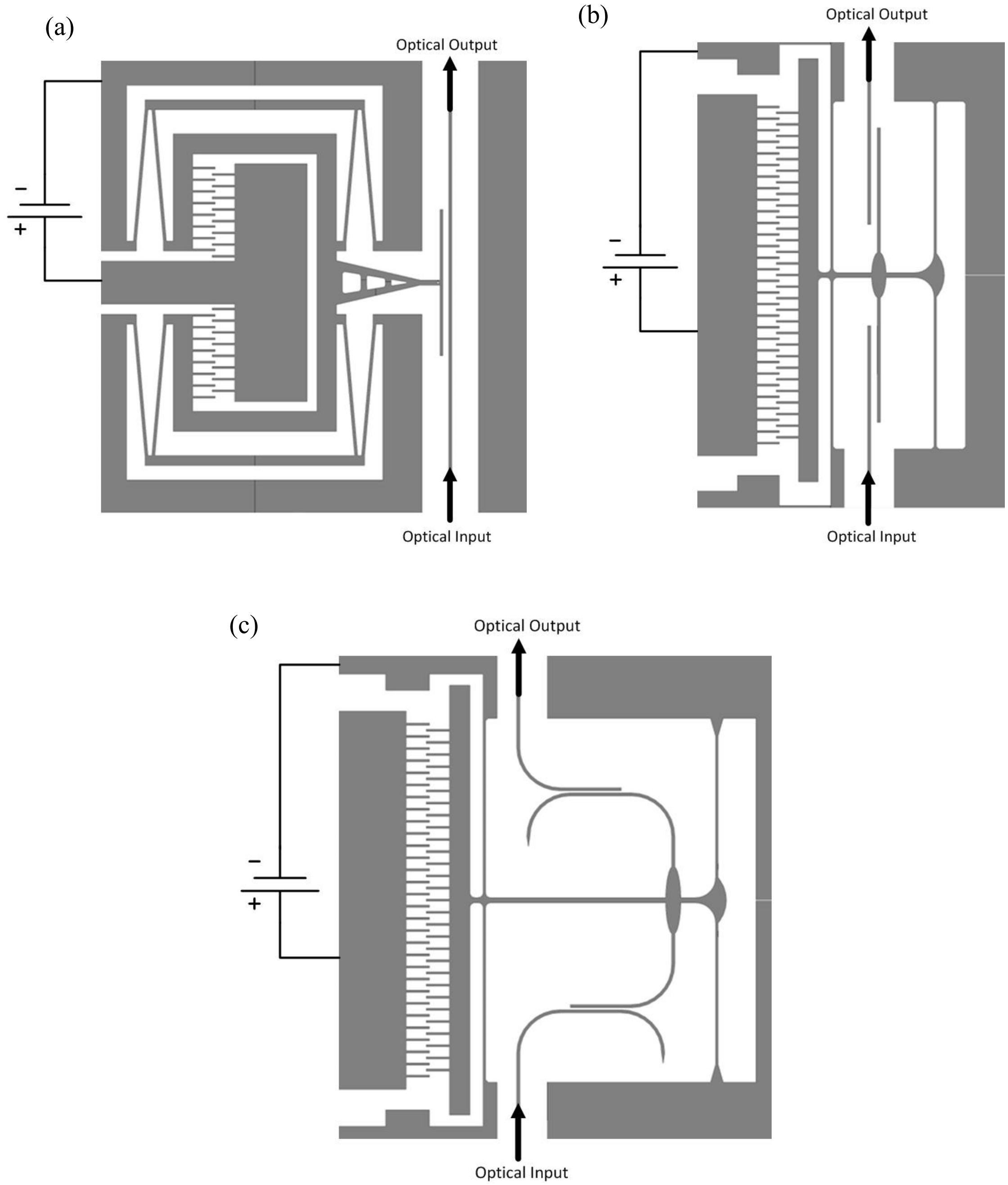

Figure 7.1: Designed micro-structures to test the performance of ODCs in motion as displacement sensor.

7.1 Simulations

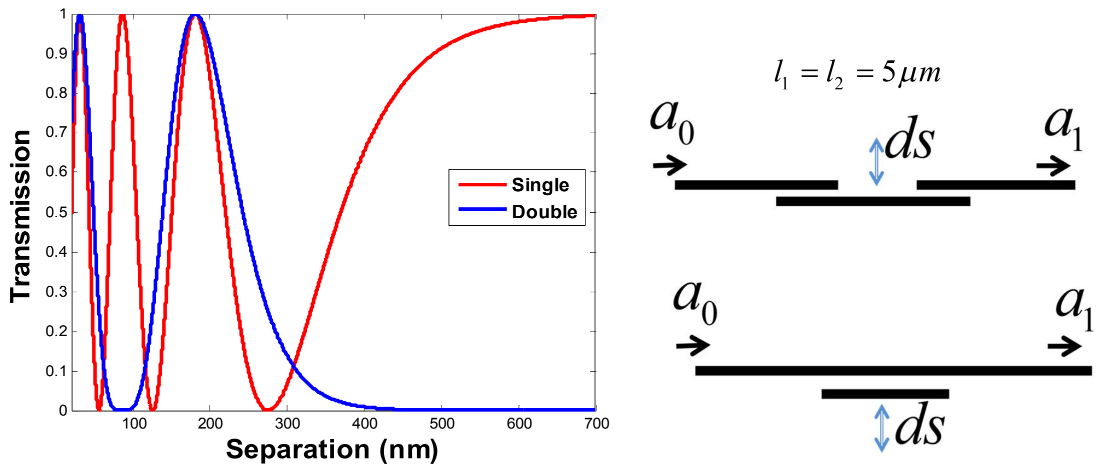

Figure 7.2: Transmission comparison of total 10 m-long single and double ODCs.

In order to get easier devices to fabricate and prevent the effects of mechanical connections to the optical waveguides on the optical performance of the devices an ODC is splitted up in to two ODCs with the same total length. The transmission of the devices for a total length of 10µm for both single and double ODC devices as a function of separation is given in Fig. 7.2. The output field profiles for single and double devices are formulized respectively, based on the Coupled Mode Theory (CMT) as follows:

$$\frac{a_1}{a_0} = e^{-j\beta(l_1+l_2)}t \tag{7.1}$$

$$\frac{a_1}{a_0} = e^{-j\beta(l_1+l_2)}(-\kappa_1\kappa_2) \tag{7.2}$$

where $l_1 = l_2 = 5\mu m$ is length of each ODC in the double ODC device and $l_1 + l_2 = 10\mu m$ is the total length of the single ODC device. t is the transmission coefficient, κ_i is the coupling coefficient of the ODC i and β is the propagation constant. As it is shown in Fig. 7.2, for instance, around the operating point of 200 nm the sensitivity of the device is generally decreased, but still functioning as a high-sensitivity displacement sensor at short ranges of displacements and more functional in practice.

In order to have higher range displacement sensors, one can take advantage of power change along the ODCs. Figure 7.3 shows how two ODCs are cascaded in order to obtain higher sensitivities rather than a single ODC. To obtain high sensitivity devices to motion, one can use smaller separations, but using smaller separations needs accurate and expensive lithography tools. For a total length of 12μm the transmission of the devices are plotted in terms of the displacement dl. The sensitivity of the double ODC device is less than the single device with the same total length for 200nm separations.

$$\frac{a_1}{a_0} = e^{-j\beta(l_1+l_2-2dl)}(-\kappa_1\kappa_2) \quad \textbf{(7.3)}$$

$$\frac{a_1}{a_0} = e^{-j\beta(l_1+l_2-2dl)}t \quad \textbf{(7.4)}$$

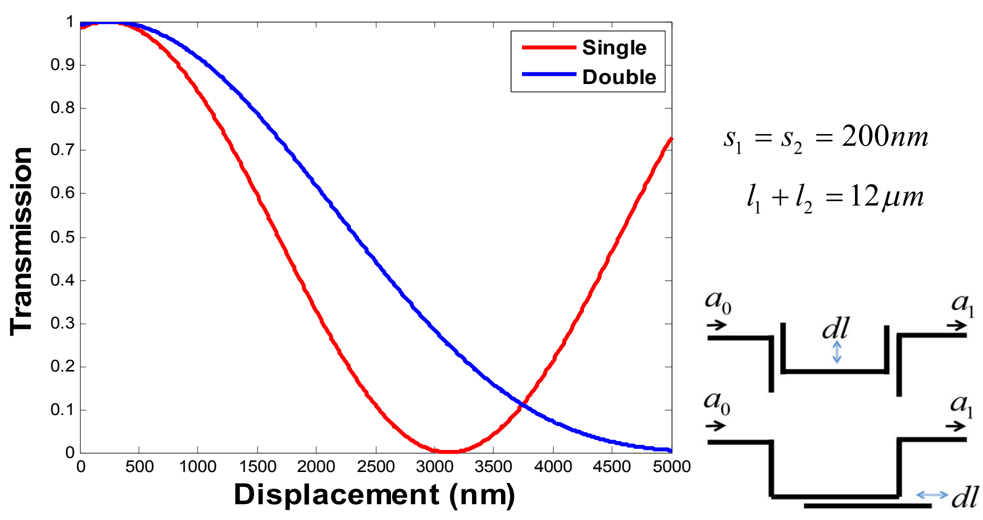

Figure 7.3: Transmission comparison of total 12 m-long single and double ODCs.

As schematically illustrated in Fig. 7.4, another device is proposed based on the phase difference generated between the arms of a balanced Mach-Zehnder interferometer

(MZI). Assuming an ideal 3dB-splitter and combiner at the input and output of the device, β_w and β_c as the propagation constants in a single waveguide and coupler, L_{MZI} as the MZI's arm length, L_c as the coupler's length and t_c as the coupler's transmission coefficient, the output field profile is driven based on CMT:

$$\frac{a_1}{a_0} = \frac{1}{2} e^{-j\beta_w L_{MZI}} (1 + t_c e^{-j(\beta_c - \beta_w)L_c}) \ (\mu m) \quad \textbf{(7.5)}$$

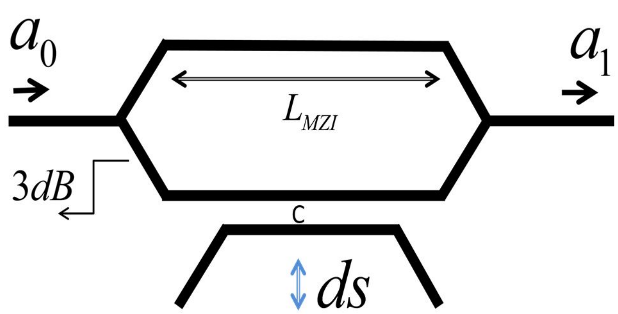

Figure 7.4: MZI with a coupled waveguide to one of the arms.

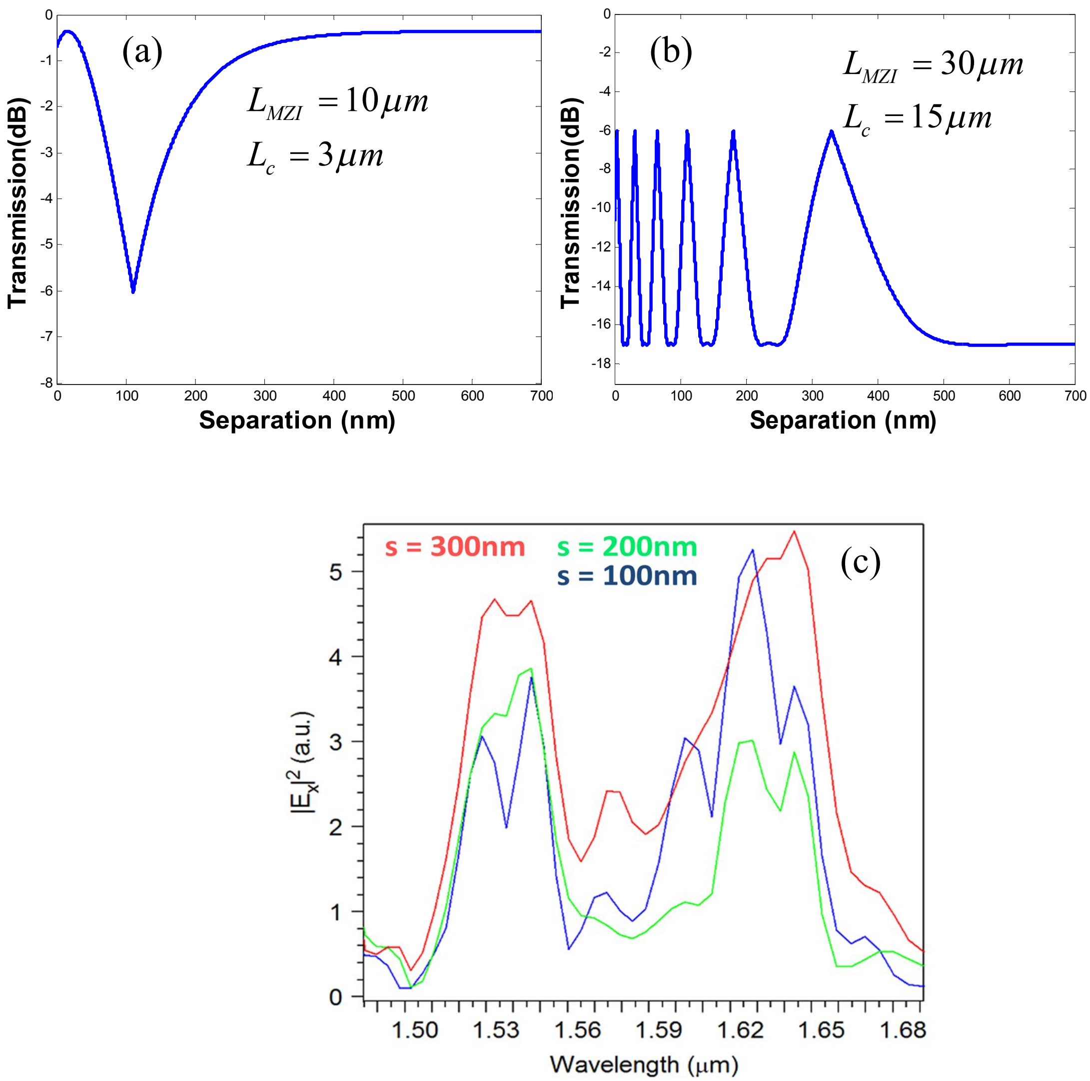

Figure 7.5: Transmission of device with (a) $L_{MZI} = 10\mu m$ and $L_c = 3\mu m$ and (b) $L_{MZI} = 30\mu m$ and $L_c = 15\mu m$, and (c) transmission spectra of device with $L_{MZI} = L_c = 6\mu m$ for separations of 100nm, 200nm and 300nm.

Figure 7.5a shows the transmission of a device with a MZI length of 10μm and a coupler of 3μm as a function of coupler's separation it is clear that increasing the length of the coupler will result in higher sensitivities as it is compared with a device with 30μm-long MZI and 15μm-long coupler.

The transmission spectra for a device with 6μm-long MZI and coupler lengths are plotted in Fig. 7.5c for various separations of the coupler. The results show that the output density is highly dependent on the wavelength. Figure 7.6a shows the FDTD simulation for an MZI with a coupler at one of its arms separated with 300nm distance. For instance, at the wavelength of 1537.5nm it is shown how the coupler induces a phase difference at 100 nm separation compared with the one at 300nm in Fig. 7.6b.

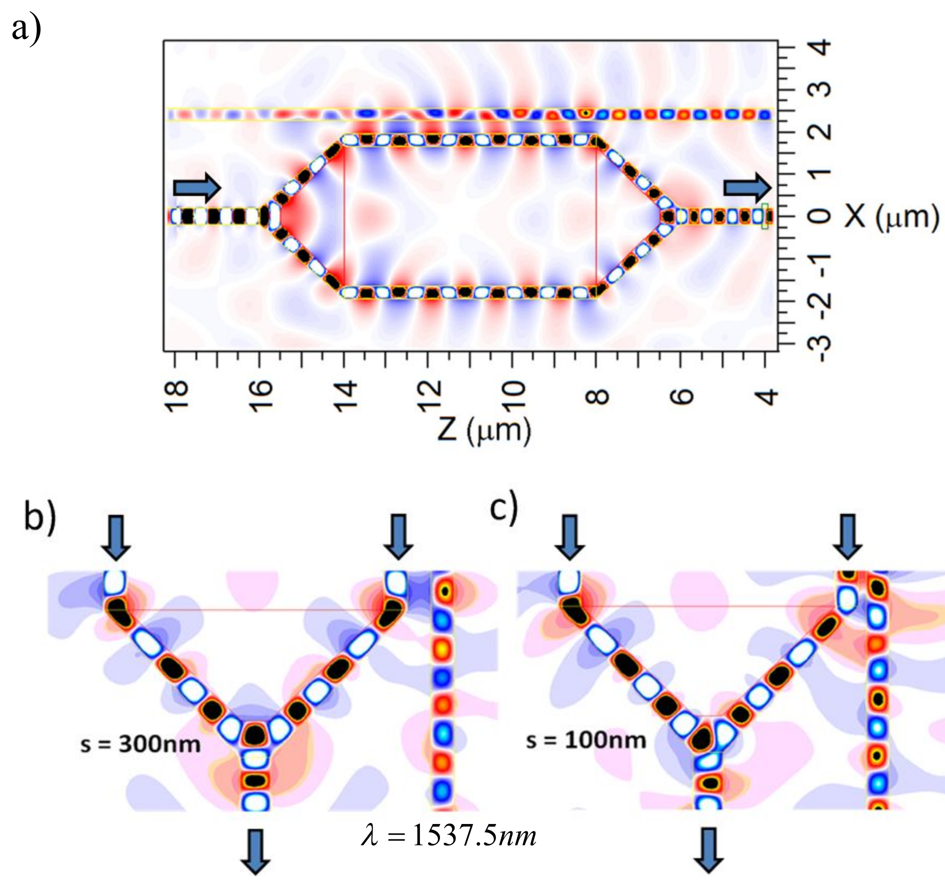

Figure 7.6: Transmission of device with (a) L_{MZI} = *10μm* and L_c = *3μm* and (b) L_{MZI} = *30μm* and L_c = *15μm*, and (c) transmission spectra of device with $L_{MZI} = L_c$ = *6μm* for separations of 100nm, 200nm and 300nm.

7.2 Design of micro-comb actuator

The relationship between displacement and applied voltage can be approximately calculated by [1]:

$$x = \frac{F_e}{k} = \frac{\dfrac{n\varepsilon t V_a^{\,2}}{s}}{\dfrac{4Etw^3}{L^3}} = \frac{n\varepsilon L^3}{4Esw^3} V_a^{\,2} \ (\mu m) \qquad \textbf{(7.6)}$$

where F_e is the electrostatic force produced by the comb drive actuator, k is the spring constant of the folded beams, n is the number of comb drive fingers, ε is the permittivity in air, t is the device thickness, V_a is the applied voltage, s is the air gap between two adjacent fingers, E is the Young's modulus, w is the width of the folded beams, and L is the length of the folded beams.

For $n = 30$, $t = 340nm$, $s = 200nm$, $w = 270nm$ and $L = 17\mu m$ the displacement of the comb actuator as a function of applied voltage is plotted in Fig. 7.7. For experimental calculation of the displacement, applied voltage is calculated by

$$v = \frac{i_n}{fT} V_p \qquad \textbf{(7.7)}$$

where i_n is the number of the captured frames, f is the frame rate of the video, T is the duration of the video and V_p is the maximum applied voltage. Then, displacement can be measured using given Eq. 7.8.

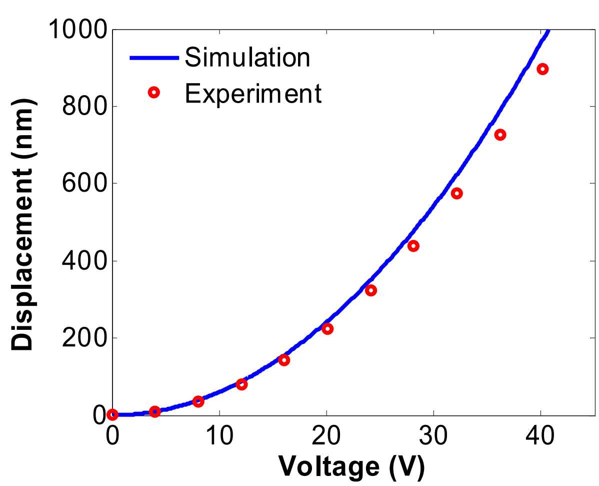

Figure 7.7: Displacement of the micro-comb actuator as a function of applied voltage

7.3 Fabrication of Structures

Based on the simulations and experimental results obtained so far, different strategies according to the fabrication limits are considered in order to measure the mechanical displacement produced by actuation in real time to measure the motions in high or low range distances with high and low sensitivities. Here, in order to generate motion in the system, electrostatic forces generated by the designed micro-comb actuator are utilized. For this purpose MZI devices with a 30 µm-long arms and 10µm, 12.5µm, 17.5µm and 20µm-long couplers, and double ODC devices with a total coupled length of 10µm, 15µm are designed to be fabricated. Hence a large range of devices with different ranges and sensitivities can be covered.

The SOI wafer is with 340nm-thick device silicon and 3 m-thick buried-oxide layer. Electron beam resist (PMMA C2) is spin coated on the wafer with a pre-bake in 180˚C for 2 minutes. Then, the wafer is accelerated by 1000 rpm and 4000 rpm for 2 and 45 minutes, respectively. Finally, the wafer is post-baked for 60 minutes in 180 ˚C.
Then using electron beam lithography small and large features of the device pattern is written on the PMMA layer. The E-beam current is chosen 80pA with a dose of 800µC/cm^2 for small and 1200 µC/cm^2 for large features at 100kV. Afterwards, patterns are developed with a mixture of MIBK and IPA with a portion of 1 and 3 for 40 seconds, respectively. Then, wafer is rinsed in IPA bath for 20 seconds followed by a 5 minutes baking in 120 ˚C.
By using Thermal Evaporator, a 30nm-thick Chromium layer was coated on the devices which were previously patterned on the photo resist. For this purpose, with a deposition rate of approximately 0.02 A/sec at around 4V a layer of 30nm-thick Chromium is coated on the PMMA layer. Then, Cr is sonicaly lifted off in Aceton bath. Consequently, using dry etching in SF_6/O_2 plasma, the device silicon was etched down to the SiO_2 layer. The Botch process was performed in -20 ˚C temperature at 10mTorr pressure. Flow rate of SF_6 and O_2 gasses are 48sccm and 24sccm, respectively with an RF power of 20W. Figure7.8 shows the SEM images taken after ICP process. After ICP step, to remove the Chromium layer, a mixture of 2KMnO4: 3NaOH: 12H2O is

used for chromium removal which successfully removed the Chromium layer. Figure7.8 shows the SEM images taken after ICP process.

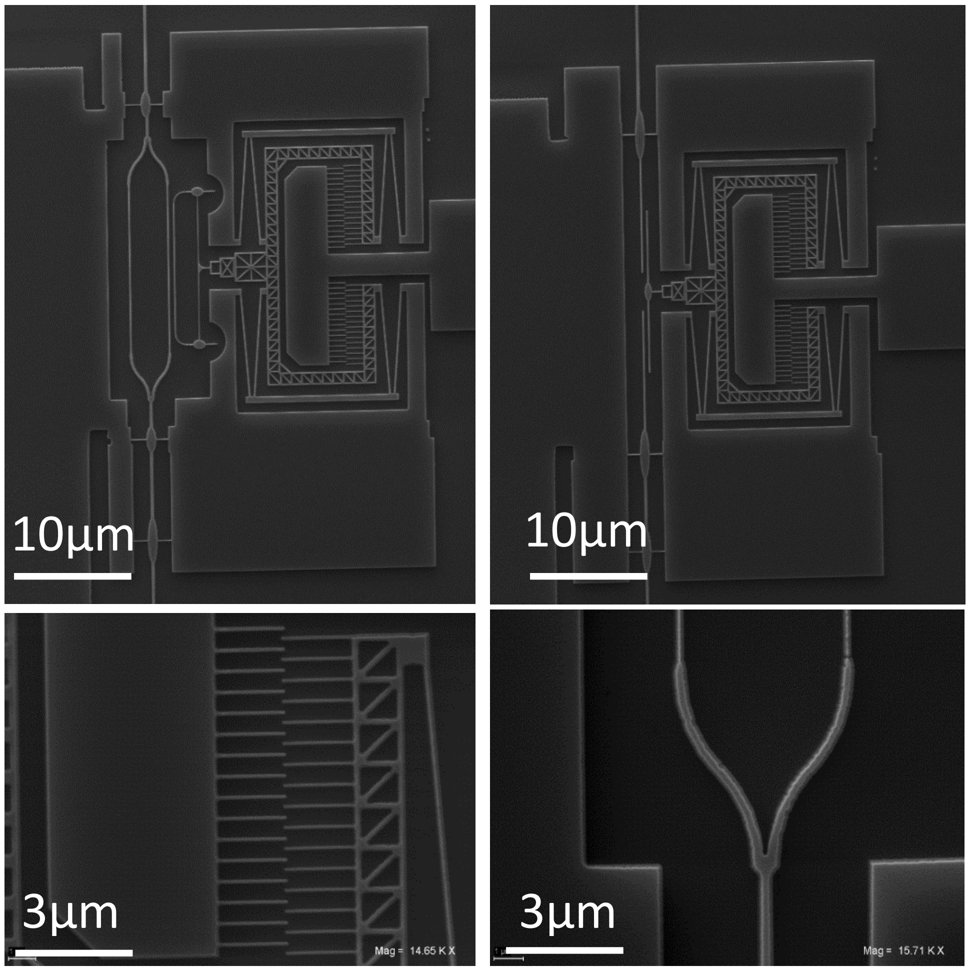

Figure 7.8: The fabricated devices after ICP process.

For the purpose of device release in order to suspend the mechanical components of the system a custom vapor HF etcher shown in Fig 7.9 is used. The temperature of the liquid HF is set to 30 ˚C and wafer is kept at 35 ˚C. For approximately 10 minutes of vapor HF exposure the 3µm-thick SiO_2 layer is etched around 2µm from the Si layer edges. The fabricated devices for both MZ based structure and ODC based structure are demonstrated in Fig. 7.10.

Figure 7.9: Vapor HF setup.

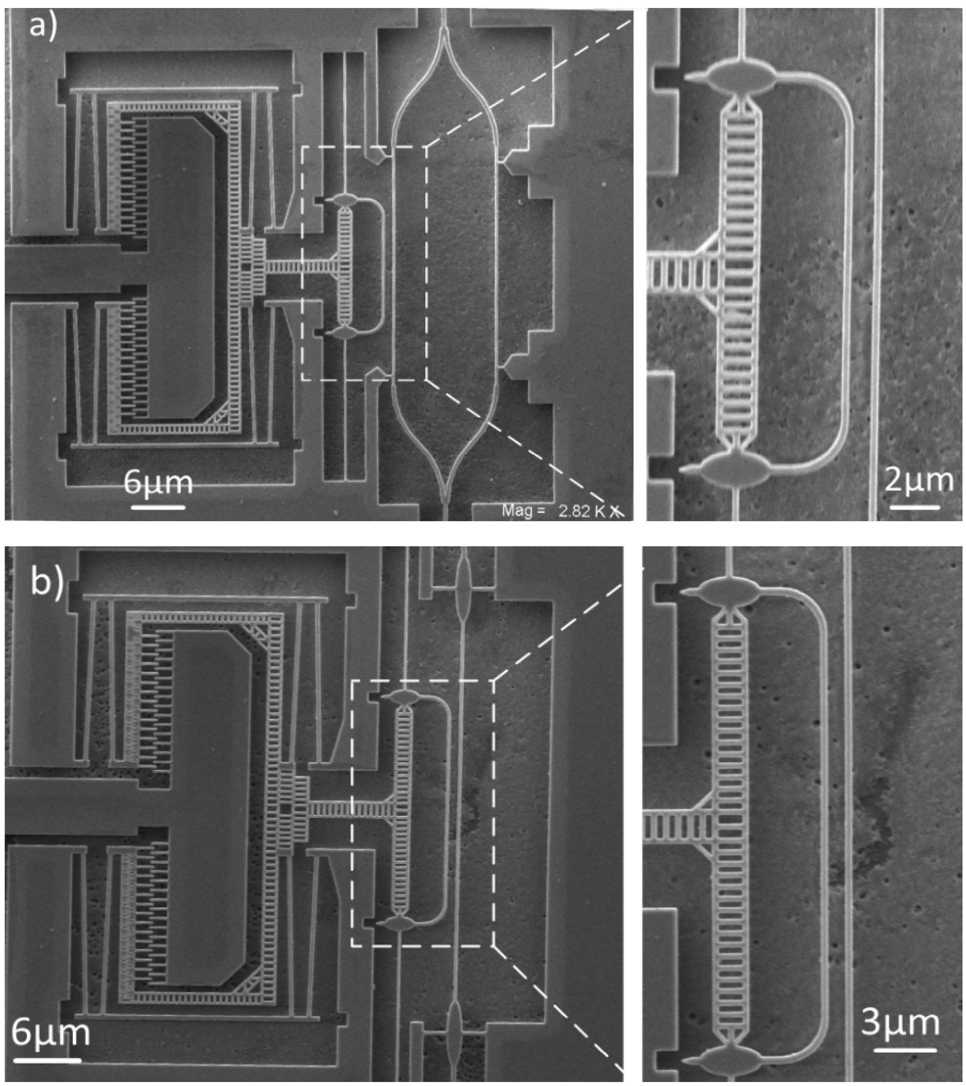

Figure 7.10: SEM images of (a) MZI based structure, and (b) ODC based structure.

From the SEM measurements, micro-comb actuators are fabricated such that the fingers have 270nm width with 200nm air gap and 1.8μm length. Springs have a length of 17μm and width of 450nm.

The optical waveguides are 310nm in width and have an initial separation of 950nm. Waveguides are held using 140nm-wide holders directly connected to the optical waveguides in order to prevent the waveguides from bending downward. The splitter and combiner are similarly designed as S-bends with 10μm radius curves and around 500nm-wide in order to decrease the optical loss as small as possible.

7.4 Characterization

In order to experimentally test the fabricated devices, the characterization setup same as shown in Fig. 6.2 is used. Here, to test the devices at each separation, a voltage is swept over the entire range of possible separations for the coupled waveguides. The optical output power coupled into the lens objective is detected by the InGaAs NIR camera and recorded as sequence of frames. The camera records videos at 49 fps, and the recorded output power as function of separation given by the following formula can be plotted.

$$x = x_0(\mathrm{n}_f / \mathrm{N})^2 \qquad \textbf{(7.8)}$$

where x_0 is the initial separation, n_f is the number of the frame and N is the total number of the frames. Obviously, above equation is valid when voltage linearly varies by time. For this purpose a ramp-like signal with period of T is applied. Then, the output power can be measured by integrating over pixels including the output light power. MATLAB code for calculation of light intensity is brought in APPENDIX I.

Optical images showing the maximum mechanical displacement of the devices at 39V for MZ and 38.5V for ODC devices are depicted in Figs 7.11 and 7.12, repectively.

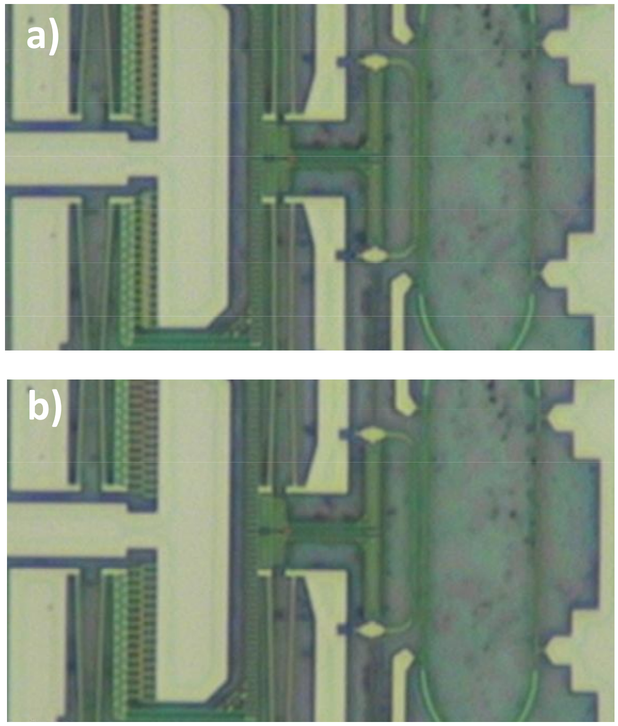

Figure 7.11: Optical images of MZI based structure at (a) maximum displacement, 950nm (39V), and (b) zero displacement (0V).

Initially, an MZ device with 400nm waveguide and coupling length of 20μm width during the fabrication was fabricated. Figure 7.13 shows the experimental results compared with the simulation ones at 1550nm wavelength for TE light. The normalized transmission shows more than 4 dB attenuation over a range of 300nm displacement at the wavelength of 1550nm. Both theoretical and experimental results approximately show sensitivity of 0.03 dB/nm around 190nm separation.

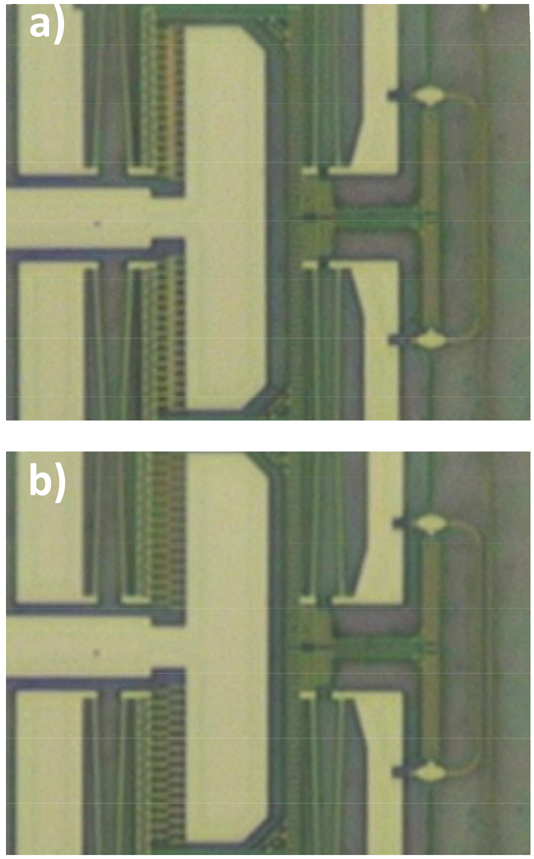

Figure 7.12: Optical images of ODC based structure at (a) maximum displacement, 900nm (38.5V), and (b) zero displacement (0V).

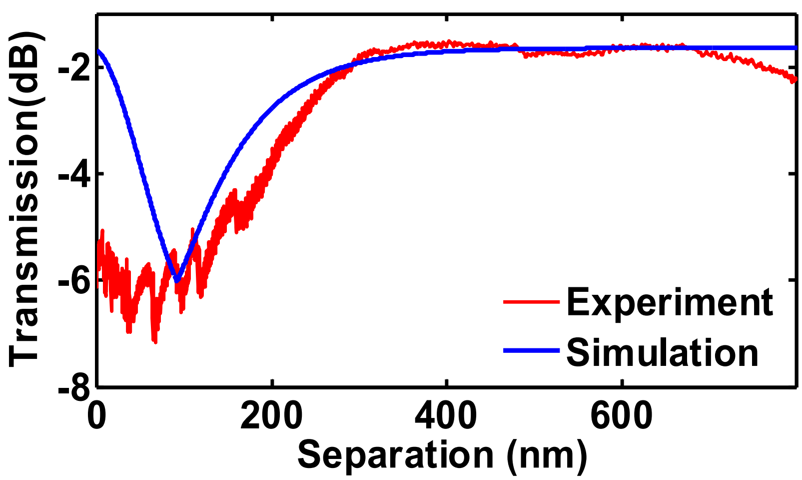

Figure 7.13: Transmission of MZ with 20µm ODC as a function of separation at 1550nm wavelength.

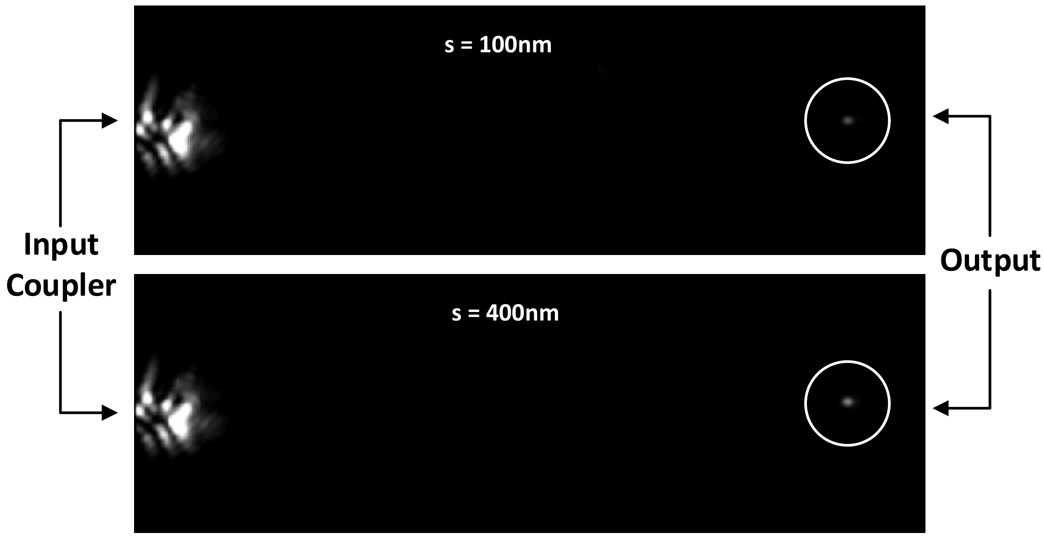

Figure 7.14: Optical micrograph of MZ with 20µm ODC under test at 100nm and 400nm separations at 1550nm wavelength.

Figure 7.14 shows the optical micrograph of the MZ structure with 20µm ODC such that the minimum and maximum of the light intensity is demonstrated at 100nm and 400nm separations, respectively.

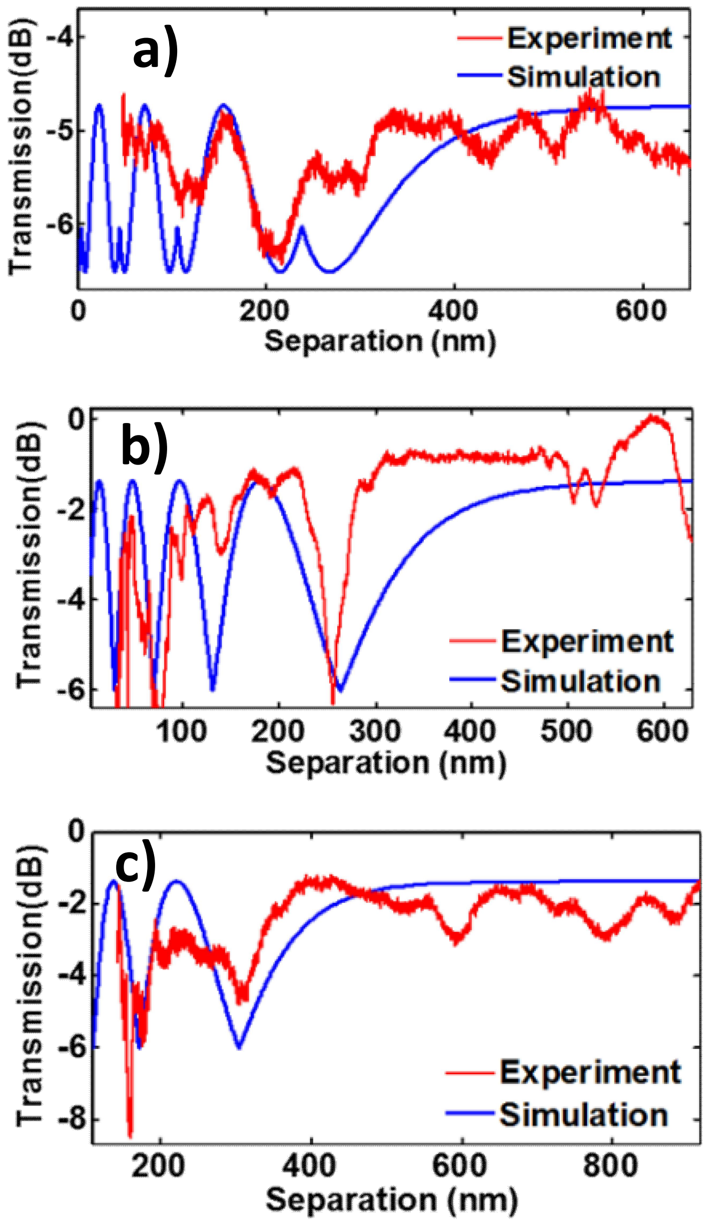

Figure 7.15 Transmission of MZ devices with (a) 10µm, (b) 12.5µm and (c) 17.5µm coupler length as a function of separation.

Furthermore, in order to increase the sensitivity of the optical transmission of the devices the waveguides are fabricated to have 310nm width. Figure 7.15 shows the transmission of the MZ devices with 10µm, 12.5µm and 17.5µm coupler length at 1550nm wavelength for TE light.

For 12.5µm and 17.5µm coupler length the attenuation in the output is increased to about 5dB at smaller separations. While, as the coupler length increases the sensitivity of the device at larger separations also increases. Assuming working at separations around 200nm, MZ devices with 10µm, 12.5µm and 17.5µm coupler length have sensitivity of 0.06 dB/nm, 0.11dB/nm and 0.03 dB/nm, respectively. The deviation from the experimental results which are calculated to be 0.06 dB/nm, 0.2 dB/nm and 0.08 dB/nm, respectively, can be due to the nonlinear response of the power combiner or the reflections from the waveguide holders.

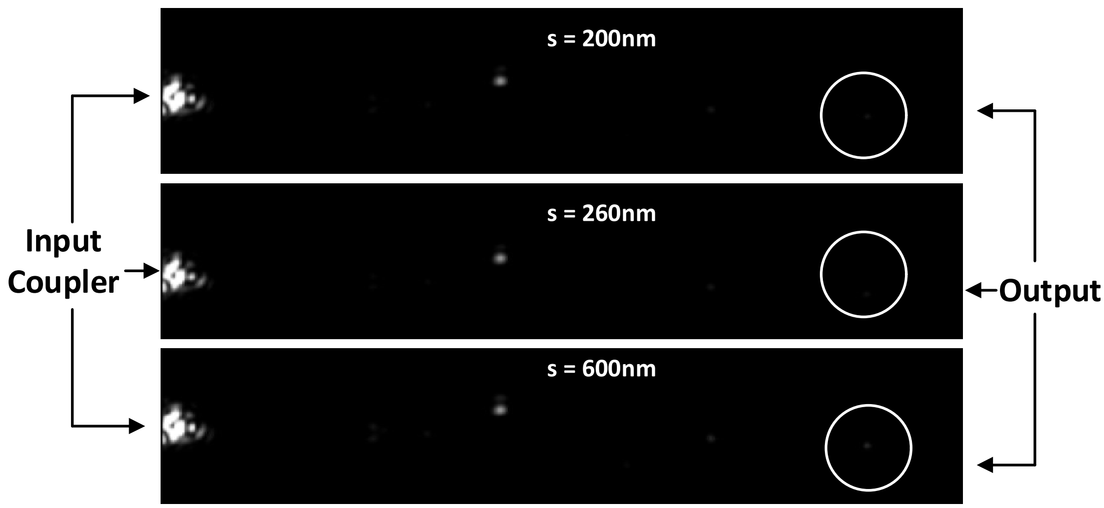

Figure 7.16: Optical micrograph of MZ with 12.5µm ODC under test at 200nm, 260nm and 600nm separations at 1550nm wavelength.

Figure 7.16 shows the optical micrograph of the output light of the MZ structure with 12.5µm coupler length illustrating how the signal can change from about -2dB at 200nm down to -6dB in around 60nm displacement at 260nm separation, while signal can reach to its maximum value at 600nm separation.

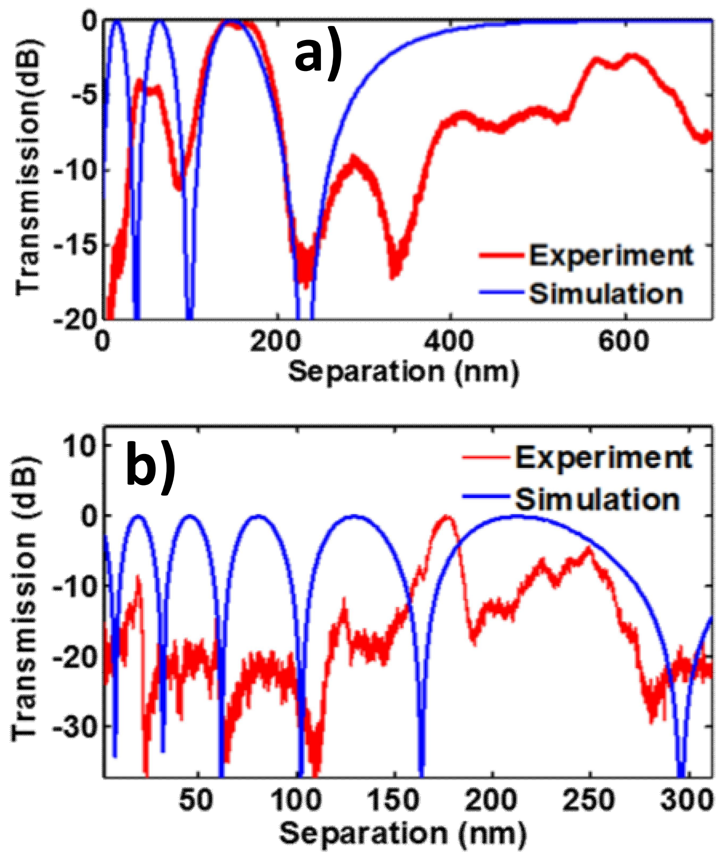

Figure 7.17 Transmission of ODC with (a) 10µm and (b) 15µm length as a function of separation.

Also ODC devices connected to fabricated comb-actuators are characterized. Smaller length of the coupler shows lower sensitivities to separation changes as for 10µm-long ODC shown in Fig 7.17a, fluctuations at the small separations are less when compared to 15µm-long one shown in Fig 7.17b. Figure 7.18, for instance, illustrates the change of the output light of a 10µm-long ODC from 180nm to 230nm. The extinction is measured to be more than 15dB. The sensitivity of ODC with 10µm length is calculated to be 0.32 dB/nm for both experiment and simulation at around 100nm separation. While, for 15µm-long ODC it is calculated to be 0.43 dB/nm experimentally and 0.86 dB/nm in simulation. Decrease in the simulated sensitivity is due to the loss of the signal observed at the output and also the saturation which does not allow the signal to be smaller than a certain value.

The deviation between experimental and calculated results are due to the nonlinearities in the Y-combiner and also reflections and losses caused by the waveguide holders and the facet of the output. Also Fabry-perot reflections in the MZ structure generated during characterization can be a source of deviation as well.

Figure 7.18 Optical micrograph of ODC with length of 10µm under test at 180nm and 230nm separations at 1550nm wavelength.

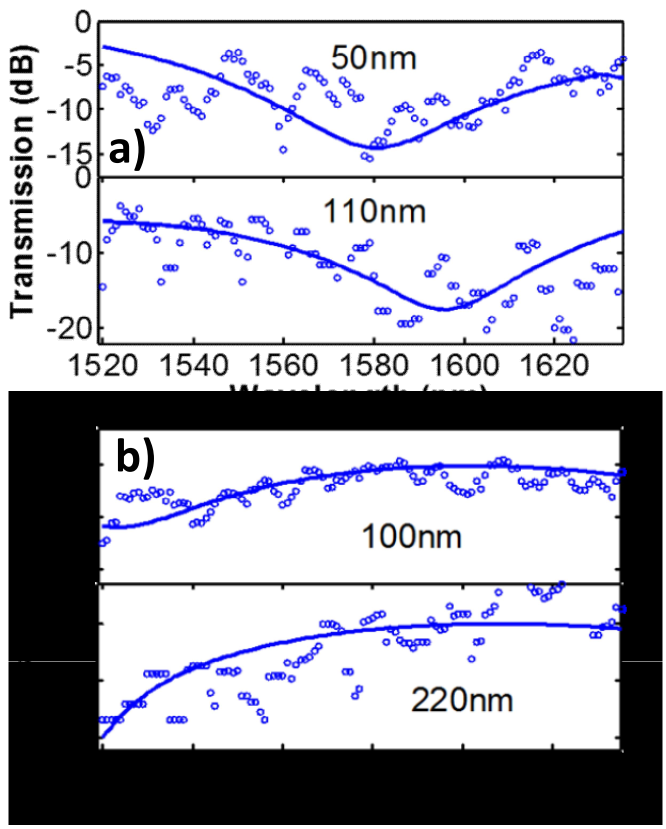

Figure 7.19 Spectral response of MZ device with (a) 12.5µm coupler length at 50nm and 110nm separations, and (b) 17.5µm coupler length at 100nm and 220nm separations. (Circles show the experimental results, and solid lines show the calculated theoretical ones.)

Moreover, the spectral response of the devices are experimentally measured and compared with the simulation ones. Figure 7.19a corresponds to the MZ device with 12.5µm coupler length at 50nm and 110nm separations. The results show that by increasing the separation dip in the spectra red-shifts. Spectral response of MZ device with 17.5µm coupler length at 100nm and 220nm is illustrated in Fig. 19b. Results show that the dip in the spectra blue-shifts while experiences approximately 10db more attenuation.

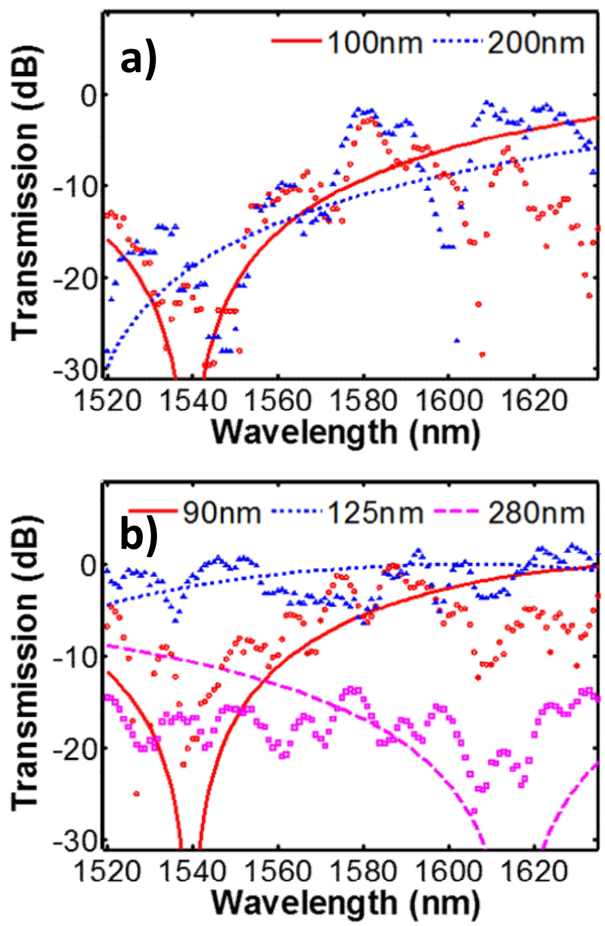

Figure 7.20 Spectral response of ODC with length of (a) 10µm, and (b) 15µm. (Discrete markers show the experimental results, and lines show the calculated theoretical ones.)

The spectra of the ODC structures are also measured. Figure 7.20a shows the spectral response of ODC with length of 10µm for 100nm and 200nm separations. Comparing the spectra of 10µm-long ODC with 15µm-long one whose spectra are depicted in Fig. 7.20b, as the length of the coupler increases sensitivity of the spectral characteristics of the ODC to the separation changes increases.

8. CONCLUSION

In this study, ultra-compact optical directional couplers based on Si-wire waveguides on SOI wafer are simulated, fabricated and characterized. The coupling length and optical output powers are presented in terms of wavelength, coupled-waveguides length, separation and cross-sectional geometry parameters. The coupling length of an ODC is found to be exponentially dependent on the wavelength and waveguides separation. Typical ODCs with 300nm×340nm (width_thickness) cross-sectional geometry embedded on an SOI wafer using 30kV-electron beam lithography are fabricated and characterized. The power transmission of ODCs with various lengths at different separations in the range of 50nm to 350nm is measured. Experiments agree well with simulations. The results show that the output light power changes sinusoidally with the length of the coupler. The gradient field between two waveguides is highly dependent on their separation such that smaller separation distances yield smaller coupling lengths causing sharper variations at the output power. Hence, ODCs with variable separation can be exploited for high-sensitivity optomechanical switches or sensor devices while changes in length can be utilized in applications requiring higher range of motion or low-sensitivity. ODCs as filters and wavelength-selective devices are also simulated, fabricated and characterized. The separation and length of the ODCs can be optimized for the desired filter spectrum. The transmission spectra of ODCs are found to be tunable by their separation and length such that, for instance, increasing the separation distance from 150nm to 200nm for a 10_m-long ODC at 1578nm wavelength will drop the transmission from almost 100% down to about 0% at through port. Longer ODCs have more channel dropping characteristics making them suitable for the design of tunable wide-FSR channel-dropping filters.

Based on the experimental results, structures are proposed in order to characterize the performance of couplers with respect to the dynamic changes of variables. The transmission of optical cascaded couplers are expressed based on the Coupled Mode Theory in order to find the best operating point for the applications as high or low range and high or low sensitivity sensors. It is found that by coupling light to the other waveguide, the phase of the propagating field changes based on the separation and length of the coupler. By coupling a waveguide to one of the arms of a balanced Mach-Zehnder, and exploiting the phase shift induced by the changes in the coupling length originated from the variation in the separation of waveguides, a phase difference can be generated between the light fields reaching to the output of the Mach-Zehnder. Hence, constructive and destructive combination of the light fields can be measured as the effect of a displacement. Several devices integrated with micro comb-actuators as nanomechanical motion source are proposed and simulated both numerically and based on the CMT. MZ based structures with 10µm, 12.5µm and 17.5 µm, and ODCs with 10µm and 15µm are fabricated and tested experimentally. It is shown that with MZ devices an extinction ratio of more than 4dB can be achieved in less than 60nm displacements. Also, thanks to the changeable coupling length of ODC, especially at small separations for long devices, for less than 25nm displacement more than 10dB attenuation at the output signal of ODC with length of 15µm can be observed. The spectral response of the fabricated devices are also measured. Results reveal that the spectra of the MZ based devices us very sensitive that by tuning the separation of the device, same spectra can be achieved at the desired wavelength. Furthermore, ODC devices show high sensitivities at small separation, while, for instance, for a 15µm-long ODC at 125nm separation more than 25dB attenuation can be achieved by decreasing the separation to 90nm at 1540nm wavelength.

REFERENCES

[1] **T. Yamazaki, H. Aono, J. Yamauchi, and H. Nakano,** (2008). "Coupled waveguide polarization splitter with slightly different core widths," *Journal of Lightwave Technology*, vol. 26, no. 21, pp. 3528–3533.

[2] **I. Kiyat, A. Aydinli, and N. Dagli,** (2005). "A compact silicon-on-insulator polarization splitter," *Photonics Technology Letters*, IEEE, vol. 17, no. 1, pp. 100–102.

[3] **Y. Yue, L. Zhang, J. Yang, R. Beausoleil, and A. Willner,** (2010). "Silicon-oninsulator polarization splitter using two horizontally slotted waveguides," *Optics Letters*, vol. 35, no. 9, pp. 1364–1366.

[4] **L. Augustin, J. van der Tol, R. Hanfoug, W. de Laat, M. van de Moosdijk, P. van Dijk, Y. Oei, and M. Smit,** (2007). "A single etch-step fabricationtolerant polarization splitter," *Journal of lightwave technology*, vol. 25, no. 3, pp. 740–746.

[5] **D. Dai, J. Bauters, and J. Bowers,** (2012). "Passive technologies for future large-scale photonic integrated circuits on silicon: polarization handling, light non-reciprocity and loss reduction," *Light: Science & Applications*, vol. 1, no. 3, p. e1.

[6] **I. Park, H. Lee, H. Kim, K. Moon, S. Lee, S. Park, E. Lee,** (2004). "Photonic crystal power-splitter based on directional coupling," *Optics Express*, vol. 12, no. 15, pp. 3599–3604.

[7] **P. Luan, K. Chang,** (2007). "Periodic dielectric waveguide beam splitter based on co-directional coupling," *Opt. Express,* vol. 15, no. 8, pp. 4536– 4545.

[8] **T. Tsuchizawa, K. Yamada, H. Fukuda, T. Watanabe, J. Takahashi, M. Takahashi, T. Shoji, E. Tamechika, S. Itabashi, and H. Morita,** (2005). "Microphotonics devices based on silicon microfabrication technology," *Selected Topics in Quantum Electronics*, IEEE Journal of, vol. 11, no. 1, pp. 232–240.

[9] **A. Prabhu, V. Van, W. Herman, and P. Ho,** (2009). "Compact silicon microring assisted directional couplers for optical signal processing applications," *Optics letters*, vol. 34, no. 8, pp. 1249–1251.

[10] **I. De Vlaminck, J. Roels, D. Taillaert, D. Van Thourhout, R. Baets, L. Lagae, and G. Borghs,** (2007). "Detection of nanomechanical motion by evanescent light wave coupling," *Applied physics letters*, vol. 90, no. 23, pp. 233116–233116.

[11] **T. Ikeda, K. Takahashi, Y. Kanamori, and K. Hane,** (2010). "Phase-shifter using submicron silicon waveguide couplers with ultra-small electromechanical actuator," *Optics express*, vol. 18, no. 7, pp. 7031–7037.

[12] **W. Bogaerts, P. Dumon, D. Thourhout, D. Taillaert, P. Jaenen, J. Wouters, S. Beckx, V. Wiaux, and R. Baets,** (2012). “Compact wavelength selective functions in silicon-on-insulator photonic wires,” *Selected Topics in Quantum Electronics*, IEEE Journal of, vol. 12, no. 6, pp. 1394– 1401.

[13] **R. Chatterjee and C. Wong,** (2010). “Nanomechanical proximity perturbation for switching in silicon-based directional couplers for high-density photonic integrated circuits,” *Microelectromechanical Systems, Journal of*, vol. 19, no. 3, pp. 657–662.

[14] **T. Chu, H. Yamada, S. Ishida, and Y. Arakawa,** (2005). “Compact 1× n thermo optic switches based on silicon photonic wire waveguides,” *Optics Express*, vol. 13, no. 25, pp. 10109–10114.

[15] **D. Van Thourhout and J. Roels,** (2010). “Optomechanical device actuation through the optical gradient force,” *Nature Photonics*, vol. 4, no. 4, pp. 211–217.

[16] **M. Povinelli, M. Loncar, M. Ibanescu, E. Smythe, S. Johnson, F. Capasso,and J. Joannopoulos,** (2005). “Evanescent-wave bonding between optical waveguides,” *Optics Letters*, vol. 30, no. 22, pp. 3042–3044.

[17] **B. Luff, R. Harris, J.Wilkinson, R.Wilson, and D. Schiffrin,** (1996). “Integrated optical directional coupler biosensor,” *Optics letters*, vol. 21, no. 8, pp. 618–620.

[18] **V. Passaro, F. DellOlio, C. Ciminelli, and M. Armenise,** (2009). “Efficient chemical sensing by coupled slot SOI waveguides,” *Sensors*, vol. 9, no. 2, pp. 1012–1032.

[19] **W. Bogaerts, R. Baets, P. Dumon, V. Wiaux, S. Beckx, D. Taillaert, B. Luyssaert, J. Van Campenhout, P. Bienstman, and D. Van Thourhout,** (2005). “Nanophotonic waveguides in silicon-on-insulator fabricated with CMOS technology,” *Lightwave Technology, Journal of*, vol. 23, no. 1, pp. 401– 412.

[20] **H. Yamada, T. Chu, S. Ishida, and Y. Arakawa,** (2005). “Optical directional coupler based on Si-wire waveguides,” *Photonics Technology Letters*, IEEE, vol. 17, no. 3, pp. 585–587.

[21] **G. Reed and A. Knights,** (2004). Silicon Photonics: an introduction, Wiley.

[22] **D. Scarlat, S. Ruschin, and D. Brooks,** (1996). “Experimental characterization of coupled waveguides by normal-mode excitation,” *IEEE J. Quantum Electron.*, vol. 33, pp. 1132–1140.

[23] **V.M.N. Passaro,** (2008). "Polarization-insensitive directional couplers based on SOI wire waveguides", *The Open Optics Journal*, vol. 2, pp. 6-9.

[24] **McCosker, Ravi J, Town, Graham E,** (2010). "Multi-Channel Directional-Coupler as an Evanescent Field Optical Sensor" *Sens.* Actuators B: Chem..

[25] **Zandi, K., Wong, B., Jing Zou, Kruzelecky, R.V., Jamroz, W., Peter, Y.-A. ,** (2010). "In-plane silicon-on-insulator optical MEMS accelerometer using waveguide fabry-perot microcavity with silicon/air bragg mirrors," *Micro Electro Mechanical Systems (MEMS), 2010 IEEE 23rd International Conference on* , vol., no., pp.839-842, 24-28.

[26] **T. Findakly and C. L. Chen,** (1978). "Optical directional coupler with variable spacing," *Appl. Opt.*, vol. 17, pp. 769–773.

[27] **R. Legtenberg, A. W. Groeneveld, and M. Elwenspoek,** (1996). "Comb-drive actuators for large displacement," *J. Micromech. Microeng*. 6(3), 320–329.

APPENDIX I

MATLAB code for calculating light intensity:

```
clear all
close all
clc

video1 = mmreader('W3D2T120_2ramp_2nd.avi');% reading video
video_frm = read(video1); %getting video frames
video_frm_lum =  video_frm(:,:,1,:);%getting monochromatic part of the frames
imshow(video_frm(:,:,2,10))%showing frame no.10

frameY = 587:1:618; % pixel area of the output
frameX = 308:1:333;

Output = (video_frm_lum(frameX,frameY,:,:));% getting the output frames

intensity_time = []; % summing over the output area at each frame using following
for loop
for i=1:size(Output,4)
    temp1 = sum(sum(Output(:,:,1,i)));
    intensity_time = [intensity_time temp1];
end

data_range = (i/2)-400:-1:1;
intensity_time = intensity_time(data_range)/max(intensity_time(data_range));
%normalizing to the maximum value
frame_time = 1:size(intensity_time,2);

range = 900; %giving the range of the motion

figure %plotting the output
plot(range*((frame_time/size(frame_time,2)).^2),smooth(10*log10((intensity_time))),
'r-o');
```

CURRICULUM VITAE

Name Surname: Shahab Bakhtiari Gorajoobi

Place and Date of Birth: Iran, 1986

E-Mail: s.b.gorajoobi@gmail.com

B.Sc.: Electrical Engineering, University of Tehran

Professional Experience and Rewards:

Shahab received his B.Sc. from University of Tehran in Electrical Engineering in 2010. He is currently a graduate student at Istanbul Technical University (ITU), Istanbul. During his studies at ITU he was the top student among his colleagues (GPA: 4.00) while he was supported by scholarship from TUBITAK. His current research interests include opto-electronics, nonlinear optics and optical microresonators.

PUBLICATIONS/PRESENTATIONS ON THE THESIS

[1] **Shahab Bakhtiari Gorajoobi**, Mustafa Kaykisiz, Erdal Bulgan, "Characterization of Strongly Coupled Si-Wire Waveguides for High-Density Optical WDM and Sensing Applications", *IEEE/OSA Journal of Lightwave Technology, 2013.*

[2] **S.B. Gorajoobi**, M.M. Kaykisiz, E. Bulgan, "Principal and Experimental Demonstration of Nano-scale Sensing with Highly-confined Guided Evanescent Lightwave", presented at the *Optical Sensors, Rio Grande, PR, USA, 2013*.

[3] **Shahab Bakhtiari Gorajoobi**, M.Mustafa Kaykisiz, Erdal Bulgan,"Nano-scale Tunability of Sub-wavelength Optical Couplers", presented at the 9th *Nanoscience and Nanotechnology (NanoTR-9) Conference*, Erzurum, Turkey, 2013.